

Cloud Ice Particle Nucleation and Atmospheric Ice Supersaturation in Numerical Weather Prediction Models

DISSERTATION
AN DER FAKULTÄT FÜR PHYSIK DER
LUDWIG-MAXIMILIANS-UNIVERSITÄT
MÜNCHEN



vorgelegt von
Dipl.-Math. Carmen Köhler
geboren in Berlin

München, Dezember 2013

1. Gutachter: apl. Prof. Dr. U. Schumann
 2. Gutachter: Prof. Dr. G. C. Craig
- Tag der mündlichen Prüfung: 25. November 2013

Contents

Zusammenfassung	v
Abstract	vii
1 Introduction	1
1.1 Research Progress	1
1.2 Issues to be Resolved	3
1.3 Thesis Outline	4
2 Fundamentals	7
2.1 Cirrus Cloud Properties	7
2.2 Cirrus Cloud Formation	9
2.2.1 Homogeneous Nucleation	10
2.2.2 Heterogeneous Nucleation	12
2.2.3 Competition	13
2.3 Ice Supersaturated Regions	14
3 Methodology	17
3.1 Parcel Model Framework	17
3.2 Cloud Ice Nucleation	18
3.2.1 Parameterisation of Homogeneous Nucleation	19
3.2.2 Parameterisation of Heterogeneous Nucleation	24
3.2.3 Interaction of Nucleation Processes	27

3.3	Depositional Growth	30
3.3.1	Kinetic and Thermodynamic Formulation	30
3.3.2	Depositional Growth Timescale	34
3.4	Ice Nuclei Budget Variable for Heterogeneous Nucleation	36
3.5	Sedimentation	37
4	Application in Numerical Weather Prediction Models	41
4.1	Model Microphysics	42
4.2	Applied Methodics	45
4.3	Vertical Velocity Parameterisations	47
4.3.1	Fluctuations Induced by Turbulent Kinetic Energy	47
4.3.2	Sub-grid Scale Orography Induced Velocity	48
4.4	Idealised COSMO Model Simulations of Orographic Cirrus	50
4.4.1	Comparison with INCA measurements	55
4.5	Case Study With a Refined Regional COSMO-DE	58
4.5.1	Model Setup	59
4.5.2	Comparison to Meteosat Satellite Data	61
5	Comparison of the Cloud Ice and Ice Supersaturation for the GME	65
5.1	Ice Water Content Comparison with CALIPSO Data	66
5.1.1	Zonal and Meridional Ice Water Content Averages	69
5.1.2	High Cloud Frequency of Occurrence	80
5.2	Ice Supersaturation	84
5.2.1	Ice Supersaturation Frequencies in the GME	84
5.2.2	Comparison to CALIPSO GEOS-5 atmospheric data	88
5.2.3	Comparison to IFS data	90
5.2.4	Ice Supersaturated Regions	92
6	Discussion of Results	97

6.1	Summary of Results	97
6.2	Interpretation of Results	99
6.2.1	Cloud ice	100
6.2.2	Ice Supersaturation	102
6.2.3	Scale dependencies of ice microphysics processes	103
7	Conclusion and Outlook	107
	Nomenclature and Abbreviations	110
	Bibliography	115
	Acknowledgements	128
	Curriculum Vitæ	130

Zusammenfassung

Die Entstehung von Zirren geschieht auf mehreren Skalen, was eine Herausforderung für die Parametrisierung in Numerischen Wettervorhersagemodellen darstellt. Um die Vorhersage von Zirren und Eisübersättigung in der Modellkette des Deutschen Wetterdienstes (DWD) zu verbessern, werden die kontrollierenden mikrophysikalischen Prozesse untersucht und in einem neuen Wolkeneismikrophysikschema parametrisiert. Die Skalenabhängigkeit des Eismikrophysikschemas wird anhand von idealisierten, sowie realen Modellläufen mit dem Regionalmodell (COSMO) und dem Globalmodell (GME) ermittelt. Die Entwicklung des 2-Momenten 2-Moden Wolkeneisschemas beinhaltet neuartige Parametrisierungen der zwei Hauptentstehungsprozesse von Wolkeneispartikeln, homogenes und heterogenes Gefrieren. Homogene Nukleation von flüssigen Aerosolen wird in Regionen mit hohen atmosphärischen Eisübersättigungen (145-160 %) und hohen Kühlraten ausgelöst. Heterogenes Gefrieren ist abhängig von der Existenz von Eiskernen und erfolgt bereits bei niedrigen Eisübersättigungen. Die größeren heterogen gefrorenen Eispartikel können eine vorhandene Eisübersättigung abbauen und somit das Einsetzen von homogener Nukleation verhindern. Um eine Überschätzung von heterogen nukleiertem Eis zu verhindern, wurden Wolkeneissedimentation und eine prognostische Bilanzgleichung für aktivierte Eiskerne eingeführt. Eine Relaxations-Zeitskalen-Methode für das Depositionswachstum der 2-Eismoden und der größeren Schneeflocken erlaubt eine konsistente Behandlung für den Abbau der Eisübersättigung.

Ein Vergleich zwischen dem GME unter Verwendung des operationellen und dem neuen Wolkeneisnukleationsschema zeigte, dass die Entstehungsposition der Zirren von der Dynamik des Modells dominiert wird und gleich bleibt, während die innere Struktur der Eiswolken sich stark unterscheidet. Insbesondere wurde eine Verringerung des Eiswassergehaltes zwischen 9 und 11 km beobachtet. Dies stellt gemäß Auswertungen mit dem Wolkeneiswasser Produkt des CALIPSO (Cloud-Aerosol Lidar and Infrared Pathfinder Satellite Observations), eine Verbesserung gegenüber dem operationellen Schema dar. Weitere Vergleiche mit dem IFS (Integrated Forecast System) Modell des europäischen Zentrums für mittelfristige Wettervorhersage zeigten klare Verbesserungen hinsichtlich der Verteilung von Eisübersättigung mit dem neuen 2-Momenten Wolkeneisschema. Besonders erlaubt die Verwendung des neuen Schemas auch die Erfassung der Eisübersättigung innerhalb von Wolken, die mit direkten Messungen übereinstimmt. Hingegen dem IFS, dem eine Annahme der Sättigung innerhalb von Wolken zu Grunde liegt, kann somit mit dem neuen Wolkeneisschema eine physikalischere Beschreibung der Eisübersättigung erreicht werden.

Abstract

Cirrus cloud genesis is a multiscale problem. This makes the parameterisation in numerical weather prediction models a challenging task. In order to improve the prediction of cirrus clouds and ice supersaturation formation in the German Weather Service (DWD) model chain, the controlling physical processes are investigated and parameterised in a new cloud ice microphysics scheme. Scale dependencies of the ice microphysical scheme were assessed by conducting simulations with an idealised and realistic regional Consortium for Small-Scale Modeling (COSMO) model setup and a global model (GME). The developed two-moment two-mode cloud ice scheme includes state-of-the-art parameterisations for the two main ice creating processes, homogeneous and heterogeneous nucleation. Homogeneous freezing of supercooled liquid aerosols is triggered in regions with high atmospheric ice supersaturations (145 – 160%) and high cooling rates. Heterogeneous nucleation depends mostly on the existence of sufficient ice nuclei in the atmosphere and occurs at lower ice supersaturations. The larger heterogeneously nucleated ice crystals can deplete ice supersaturation and inhibit subsequent homogeneous freezing. In order to avoid an overestimation of heterogeneous nucleation, cloud ice sedimentation and a prognostic budget variable for activated ice nuclei are introduced. A consistent treatment of the depositional growth of the two ice particle modes and the larger snowflakes using a relaxation timescale method was applied which ensures a physical representation for depleting ice supersaturation.

Comparisons between the operational and the new cloud ice microphysics scheme in the GME revealed that the location of cirrus clouds is dominated by the model dynamics whereas the cirrus cloud structures strongly differed for the different schemes. Especially a reduction in the ice water content between 9 and 11 km was observed when using the new cloud ice scheme. This change is an improvement as demonstrated by a comparison with the Cloud-Aerosol Lidar and Infrared Pathfinder Satellite Observations (CALIPSO) ice water content product. Further comparisons of the GME with the Integrated Forecast System (IFS) model of the European Centre for Medium-Range Weather Forecasts (ECMWF) show a clear improvement of the ice supersaturation distribution with the new two-moment cloud ice scheme. In-cloud ice supersaturation is correctly captured, which is compliant with in-situ measurements. This is a more physical description than in the IFS model, where in-cloud ice saturation is assumed.

Chapter 1

Introduction

Cirrus clouds influence the radiative properties of the atmosphere significantly and have a high impact on climate and weather (Liou, 1986). Consequently, cirrus cloud parameterisations used in numerical weather prediction (NWP) models have been a target of growing attention in recent years. The characteristics of cirrus depend on their formation process which can occur via homogeneous or heterogeneous nucleation. The triggering of ice nucleation is strongly dependent on the ambient atmospheric condition, especially on ice supersaturation. The amount of atmospheric ice supersaturation influences the development and lifetime of natural and anthropogenic cirrus.

1.1 Research Progress

According to Waliser et al. (2009) current shortcomings in representing cirrus in general circulation models (GCMs) result in errors for the weather and climate forecasts which may lead to uncertainties in climate change projections. Deficits in cirrus cloud modelling mostly result from the spatial and temporal inhomogeneity of atmospheric nucleation (Hegg and Baker, 2009) and the non-linear influence of ice clouds on the atmospheric water distribution and the radiation budget. As an example, substantial differences can occur in the vertical distribution of water vapour depending on how ice crystal fall velocities are represented in the models (Stephens, 2002).

The net-warming effect of cirrus on the climate budget is said to be dominant by the Intergovernmental Panel on Climate Change in 2007 (Forster et al., 2007). This is not trivial, as cirrus either have a warming or cooling effect on the Earth's climate (Cox, 1971). On the one hand, they reflect incoming solar radiation causing atmospheric cooling, and on the other hand they trap outgoing infrared radiation causing atmospheric heating. The net-effect depends on the optical thickness of the cirrus cloud. Thick cirrus balance atmospheric warming and cooling, while thin cirrus have a warming effect on the atmosphere (Chen et al., 2000). Also, the climate effect of ice clouds is very sensitive to cirrus microphysical properties, e.g. ice crystal

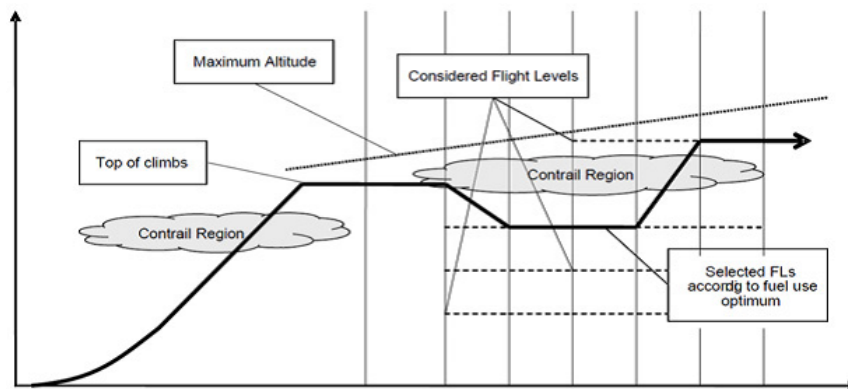


Figure 1.1: Schematic flight route with contrail region avoidance. Contrail regions depict the regions, where the air is ice supersaturated (courtesy of Lufthansa, Stefanie Meilinger).

number concentration, ice crystal habits and ice water content (IWC). Stephens et al. (1990) state that only ice crystals with effective radii larger than $16\mu\text{m}$ have a warming impact. Zhang et al. (1999) discuss that an ice water content of 10mg m^{-3} of stratiform ice clouds has a net-warming effect while an $\text{IWC} \geq 20\text{mg m}^{-3}$ has a net-neutral effect. These sensitivities remain a scientific challenge.

Anthropogenic effects on climate are gaining in importance, among them the impact of airplanes on climate change. When airplanes fly through regions with ice supersaturated air, climate-impacting condensation trails (contrails) can form. From the aircraft emissions, soot is thought to be the dominant aerosol for contrail formation (Heymsfield et al., 2010). Contrails can also form in already existing cirrus clouds, making the previously formed cirrus more opaque. Especially for climate studies, the influence of contrails and contrail-induced cloudiness is of interest. The possibility of a correct ice supersaturation forecast yields the potential to predict the formation of aircraft induced contrail cirrus (Mannstein, 2008). Thus, it is of interest to localise the regions of ice supersaturation occurrence in order to conduct flight level changes (see Fig. 1.1) to reduce anthropogenic induced cloudiness. However, in question is the trade-off between contrail formation and the additional carbon dioxide needed for the flight path change. A possible physical metric for quantifying the short-term climate effect of contrail versus the long-term effect of carbon dioxide is introduced by Deuber et al. (2013).

Cirrus clouds form through homogeneous and heterogeneous nucleation. Homogeneous freezing is thought to be dominant in regions with moderate and strong vertical updrafts and few ice nuclei in cold upper tropospheric regions. Heterogeneous nucleation plays a more important role for regions containing a lot of ice nuclei. In comparison, homogeneous freezing cause higher ice crystal number density and smaller radii to form which lead to a higher albedo effect with a global warming radiative effect (Gettelman et al., 2012). Heterogeneous nucleation results in more frequent and wide spread cirrus which have a smaller optical depth and thus a lower cloud albedo (Haag and Kärcher, 2004). In intermediate regimes where competition between the two mechanisms occur, the global mean ice nucleation concentration varies by a

factor of twenty depending on the amount of available ice nuclei in the air (Barahona et al., 2010). In particular the effects of aerosols on cloud ice nucleation are subject to current research as aerosol-cloud interactions highly influence the size and number distribution of ice crystals. However, the ice nucleation thresholds for the different aerosol species are not well understood (DeMott et al., 2011).

The formation mechanisms of cirrus clouds and their interaction with aerosols is a major field of environmental research and a great variety of approaches regarding the simulation of cirrus cloud formation were published. Examples of such publications describing cirrus formation through the two main processes, homogeneous and heterogeneous nucleation, with double-moment bulk microphysic schemes are e.g., Morrison et al. (2005) and Spichtinger and Gierens (2009a). The parameterisation of homogeneous nucleation for GCMs is described in e.g., Kärcher and Burkhardt (2008) and Barahona and Nenes (2008), and further approaches are discussed in Sec. 3.2.1. Parameterisations for heterogeneous nucleation can be found in e.g., Hoose et al. (2010) and Kärcher and Lohmann (2003), and others are described in detail in Sec. 3.2.2. Through high performance computing and higher grid resolutions, important processes can be explicitly modelled and less limiting assumptions are needed. An example being the use of non-hydrostatic opposed to hydrostatic equations in high resolution models. The improvements also lead to the possibility to represent the microphysical processes in a more sophisticated way in NWP models.

The triggering of homogeneous and heterogeneous nucleation is controlled by the existence of ice supersaturation. The importance of which was only realized in recent years (Gettelman and Kinnison, 2007). Previously in NWP models, ice supersaturation has not received much attention, with the result that the relative humidity with respect to ice was capped at 100% allowing no ice supersaturation to occur. Nowadays, NWP models are ice supersaturation permitting, like the operational NWP models of the German Weather Service (DWD), the Integrated Forecast System (IFS) of the European Centre for Medium-Range Weather Forecast (ECMWF) (Tompkins et al., 2007) and the Community Atmosphere Model (CAM3) from the National Center for Atmospheric Research (NCAR) (Gettelman et al., 2010). To permit ice supersaturation in NWP models is also of importance, as cirrus clouds are overpredicted when forced to form at ice saturation. According to Fusina et al. (2007), the overprediction of high clouds has an effect of 3 K d^{-1} on the heating rate and causes a difference in outgoing longwave radiation of $38 - 40 \text{ W m}^{-2}$. The extent of the climatologic effect of ice supersaturated regions is still not fully understood (Lee et al., 2010).

1.2 Issues to be Resolved

The main objective of this work is to develop an appropriate method to physically model ice supersaturation in the global numerical weather prediction model of the DWD (GME). The global model is chosen as it includes the North Atlantic flight corridor and already allows for the existence of ice supersaturation. The main emphasis lies on implementing an accurate

parameterisation for homogeneous and heterogeneous nucleation, as ice nucleation determines the depletion of ice supersaturation. An additional challenge is the multiscale nature of ice nucleation, along with finding a balance between accuracy and numerical expense.

The research questions of this work are:

- What are the relative roles of homogeneous and heterogeneous nucleation in formation of ice supersaturation and cirrus clouds?
- How can an improved representation of these processes in an NWP model give improved representation of cirrus and ice supersaturation?
- What are the scale dependencies of ice microphysical parameterisations?

For accomplishing a realistic representation, the sensitivities of the cirrus cloud formation processes have to be analysed. Especially mesoscale variability in vertical velocities have to be accounted for, which lead to updrafts of $10\text{-}20\text{ cm s}^{-1}$ and have a length of $10\text{-}100\text{ km}$. The variability in the vertical velocity is a primary mechanism for ice nucleation and ice supersaturation (e.g., Gultepe and Starr (1995), Kärcher and Strom (2003) and Comstock et al. (2008)). Of further importance is how to incorporate aerosol effects and the competition between homogeneous and heterogeneous nucleation determining the global cirrus features (Barahona et al., 2010). Results from the 'Cirrus Parcel Model Comparison Project' (Lin et al., 2002) suggest the critical components in cirrus modeling to be the homogeneous nucleation rate and the depositional growth of ice crystals. For the deposition growth in particular the depositional coefficient causes deviations as it controls the water vapor uptake rate. These issues are discussed in this work.

Analysed is to what extent the ice nucleation mechanisms and ice supersaturation are realistically represented in the NWP models of the DWD. Of interest is to deal with differences in the horizontal and vertical model resolution and the model time step. For example, in coarser models the vertical velocity is not well resolved. Applicable approaches to deal with fluctuations in the vertical velocity and subsequent adiabatic cooling are still missing for global modelling. Thus, the impact of different model resolutions on the microphysics is investigated.

In summary, the main task of this work is to identify the essential factors for cirrus formation and subsequently achieve a physically based description of the ice nucleation mechanisms and a realistic representation of ice supersaturation in NWP models.

1.3 Thesis Outline

In chapter two, a basic introduction to ice supersaturation, cirrus cloud properties and their formation is given. In chapter three, the methodology of the new cloud ice scheme is explained and a novel approach is developed. The individual changes are first tested with a parcel model in order to understand the impact of the individual model changes on cirrus formation.

In chapter four, the new approach is applied to the regional COSMO (Consortium for Small-Scale Modeling) model and presented along with the operational cloud microphysics scheme. Especially the introduction of sub-grid scale variability in the vertical velocity is explained, which is treated differently for different model resolutions and model physics for the regional COSMO model and the global model GME. Idealised simulations of orographic cirrus in the COSMO environment show the sensitivities of cloud ice formation with respect to the individual alterations in the cloud ice scheme. Comparisons to INCA (Interhemispheric differences in cirrus properties from anthropogenic emissions) measurements of the ice water content verifies the idealised model setup. A case study with a refined COSMO-DE model setup further demonstrates the different microphysical behaviour of ice nucleation and ice supersaturation. The results of the operational and new ice cloud scheme are compared to Meteosat Second Generation Satellite Data.

Chapter five focuses on the evaluation for the new cloud ice microphysics scheme in the GME for July 2011. The model ice water content is compared to the CALIPSO (Cloud-Aerosol Lidar and Infrared Pathfinder Satellite Observation) ice water content product. The high-cloud occurrence is verified. For validation of the ice supersaturation and its occurrence, the CALIPSO Cloud Profile atmospheric data GEOS-5 (Goddard Earth Observing System) is used. For further comparison, the relative humidity with respect to ice of the GME is additionally compared to ECMWF Integrated Forecast System (IFS) data.

A discussion of the results of the changed ice nucleation and ice supersaturation is given in chapter six. Especially the positive and negative aspects are pointed out. In the last chapter, the conclusion and outlook is presented.

Chapter 2

Fundamentals

Cirrus clouds and ice supersaturation are directly linked phenomena. In order to understand the interaction and dependencies, an overview of the characteristics of cirrus clouds and their formation as well as ice supersaturation will be given.

2.1 Cirrus Cloud Properties

According to the World Meteorological Organisation (WMO) cirrus clouds are "detached clouds in the form of white, delicate filaments or white or mostly white patches or narrow bands. These clouds have a fibrous (hair-like) appearance, or a silky sheen, or both" (WMO, 1975). This morphological definition already reflects the diversity of these upper troposphere, lower stratosphere clouds, for which a summary of the various species is outlined in Lynch (2002).

Cirrus clouds cover large areas of the Earth's surface. Recent global satellite observations lead to an average of cirrus cloud occurrence of 16.7% (Sassen et al., 2008) whereas mean values higher than 30% were evaluated by use of multispectral High Resolution Infrared Radiation Sounder (HIRS) data high cloud statistics over 8 years (Wylie and Menzel, 1999). Deviations between cirrus cloud occurrences can result from different sensitivities in the measurement techniques.

A climatologic study of global cirrus cloud cover fluctuations carried out by Eleftheratos et al. (2007) shows that the highest occurrences were found to be over the tropics. This is due to anvil clouds which form through strong updrafts in deep convection and are capable of surviving a long time. Moreover, thin and subvisible so-called cold trap cirrus is expected in the tropics (Sassen et al., 2008). In the mid-latitudes the cirrus cloud formation is strongly coupled with the ascent of air due to synoptic and frontal systems and jet streams (Sassen and Campbell, 2001). Forced uplifting at mountains results in orographic cirrus, e.g. wave clouds (Field et al., 2001). Anthropogenic induced cirrus can be obtained due to aircraft condensation trails (contrails)

Property	Mean	Measured Range
Thickness	1.5 km	0.1-8 km
Altitude	9 km	4-20 km
Crystal number density	30 dm ⁻³	10 ⁻⁴ -10 ⁴ dm ⁻³
Ice water content	0.025 g m ⁻³	10 ⁻⁴ -1.2 g m ⁻³
Crystal size	250 μm	1-8000 μm

Table 2.1: Cirrus cloud properties (Dowling and Radke, 1990)

mainly developing from water vapour exhaust (Schumann, 2002).

Cirrus clouds play an important role in the thermodynamic and dynamic system of the Earth's atmosphere through microphysics, dynamic processes, and radiation (e.g., Liou et al. (1991), Gultepe and Starr (1995), and Gu and Liou (2000)). Depending on the cirrus cloud properties they potentially have a cooling effect as they reflect solar radiation back into space (Albedo effect), but can also add to atmospheric warming by inhibiting longwave infrared radiation from escaping (Hartmann et al., 1992). Measurements performed in the Central Equatorial Pacific Experiment (CEPEX) suggest that 'thin' cirrus reduces incoming solar radiation on average by 6 W m^{-2} (Heymsfield and McFarquhar, 1996) and 'thick' cirrus on average by 29 W m^{-2} (Hartmann et al., 1992). The effect of cirrus on the radiative energy budget is mostly determined by the optical depth τ_c , which is the product of the mass extinction coefficient and ice water content (IWC), integrated over the cloud thickness. An optical depth of $\tau_c < 0.03$ is typical for subvisual cirrus, between 0.03-0.3 for thin cirrus, and from 0.3 to 3.0 for opaque cirrostratus (Sassen and Cho, 1992). The cloud optical depth is dependent on the mean effective size of the ice particles and the integrated IWC over the cloud depth, i.e the ice water path (IWP). For a constant IWP, ice crystals with a smaller mean effective radii increase the cloud albedo, which means that more short wave radiation is reflected. As a consequence they increase net radiative heating at the cloud top and corresponding cooling below opposed to larger mean effective sizes (Liou et al., 1991). The ice crystal size is dependent on the ambient temperature and decrease for higher cloud tops at lower temperatures (Heymsfield and Platt, 1984). The IWC can be derived as function of the temperature (e.g., Liou (1992), Schiller et al. (2008)) and Dowling and Radke (1990) state the IWC to range between 10^{-4} - 1.2 g m^{-3} (see Tab. 2.1).

The ice crystal number density in cirrus clouds as evaluated by Krämer et al. (2009) considering 20 flights and are subdivided into three temperature intervals. Warm cirrus with temperatures above 205 K where observed to most frequently have ice crystal number densities 0.5 - 10 cm^{-3} for 225-240 K and 0.05 - 1 cm^{-3} for temperatures between 205-225 K. In cold cirrus $T < 205 \text{ K}$ unexpectedly low number densities of 0.005 - 0.2 cm^{-3} were found (Krämer et al., 2009). Hoyle et al. (2005) state that higher values of 50 cm^{-3} can be measured and require small-scale temperature fluctuations. Differences in ice crystal number densities depend on the genesis process and measurement technique. Yano and Phillips (2011) suggest the reason for the occurrence of high number densities is due to fragmentation of ice-ice collisions (Yano and Phillips, 2011). Studies by Field et al. (2006) and Heymsfield (2007) state that over-

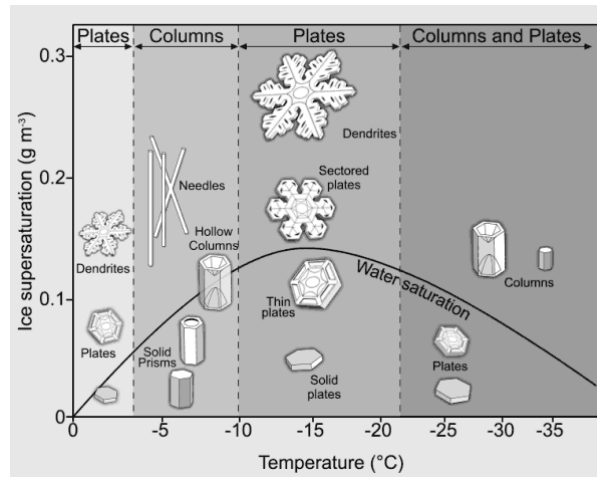


Figure 2.1: Morphology diagram depicting the different ice crystal shapes dependent on temperature and ice supersaturation (Emersic, 2012).

estimations in aircraft measurements might have occurred due to shattering of big ice crystals on the inlets of instruments. Comstock et al. (2008) assume that the shattering potentially leads to overestimations of two orders of magnitude in previously measured number densities. This result is still under discussion as it would have severe consequences for previously conducted model validations with aircraft measurements. In Sec. 2.2 the number densities and particle sizes resulting from different formation mechanisms of cirrus clouds will be discussed in further detail.

The ice particle shapes and sizes are highly variable. Baum et al. (2005) optimised a particle size distribution by using in situ data from mid-latitude and tropical ice clouds. Ice crystal maximum dimensions $D_{i,max} < 60\mu\text{m}$ are found to consist of 100% droxtals, $60\mu\text{m} < D_{i,max} < 1000\mu\text{m}$ is 15% 3D bullet rosettes, 50% solid columns, and 35% hexagonal plates. Maximum dimensions $1000\mu\text{m} < D_{i,max} < 2000\mu\text{m}$ have the combination of habits 45% hollow columns, 45% solid columns, and 10% aggregates. Maximum dimensions larger than $2000\mu\text{m}$ were found to consist of 97% 3D bullets and 3% aggregates (Baum et al., 2005). The different particle shapes and complexities strongly vary with the ambient temperature and ice supersaturation, with an overview shown in Fig. 2.1.

2.2 Cirrus Cloud Formation

The two primary cirrus cloud formation mechanisms in the upper troposphere are homogeneous and heterogeneous nucleation. Classical nucleation theory provides a basis for understanding the atmospheric processes and dynamic effects that cause cirrus clouds to form or dissipate. The classical approach is derived from the change in Gibbs free energy, being a thermodynamic potential for phase change. A free energy barrier for nucleation separates the initial liquid

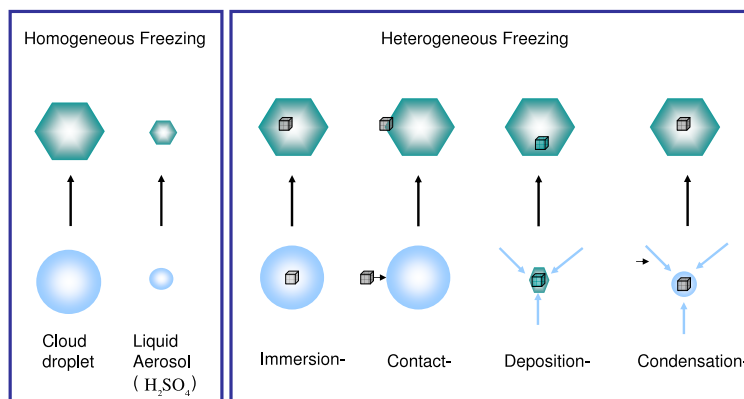


Figure 2.2: Schematic diagram for the ice nucleation modes based on Leisner (2008).

metastable phase from a solid stable phase. Once the particle is of a greater size than the critical radius it is activated. The activation of a drop at constant pressure and temperature is described by the nucleation rate giving the number of ice embryos in a liquid drop per unit time. The basic theoretical concepts are thoroughly discussed in e.g., Pruppacher and Klett (1997), Jacobsen (2005) and Hegg and Baker (2009). When using such an approach for simulations one will typically run into complications dealing with computational expenses and missing realistic intermolecular potential functions (Hegg and Baker, 2009). Thus it is of interest to formulate efficient parameterisations that capture the physical behaviour of the nucleation processes. This section deals with the general process description explaining the classical theory while state-of-the-art parameterisations will be discussed in Chap. 3. First, the basics of homogeneous and heterogeneous freezing mechanisms will be explained, with their mutual competition discussed subsequently.

2.2.1 Homogeneous Nucleation

The process of homogeneous freezing is mostly associated with pure cloud droplets freezing at -38°C (Heymsfield and Sabin, 1989). Yet in the atmosphere the existence of supercooled liquid aerosol particles plays a significant role in influencing the formation of cirrus clouds. This process plays a dominant role in cold cirrus (consisting of ice crystals) formation in water-subaturated conditions (DeMott et al., 1994). Homogeneous nucleation is not necessarily homomolecular and on the whole, at least one other chemical is present. The most common of these is sulfuric acid (H_2SO_4), which forms aqueous solutions droplets (Tabazadeh et al., 1997). Substantial ice supersaturation above 145% (Koop et al., 2000) is necessary in order for aqueous solutions to freeze.

A critical supersaturation threshold $S_{i,cr}$ for the onset of homogeneous freezing dependent on temperature is derived by Koop et al. (2000). An important process for the triggering of this regime are high vertical velocities and the subsequent adiabatic temperature decrease and thus ice supersaturation increase. Hence, in gravity waves homogeneous nucleation triggers number densities of 50cm^{-3} (Hoyle et al., 2005). Grasping this process is especially important for interpreting high number densities and consequently the effects of optical density on radiation (e.g., Kärcher and Solomon (1999), Hallett et al. (2002)). Especially small ice particles with diameters smaller than $100\mu\text{m}$ complicate the distinction between a warming and cooling effect of the cirrus clouds on the Earth's surface temperature (Fu and Liou, 1993).

The classical nucleation theory approach uses an explicit nucleation rate J , often given in units of $\text{cm}^{-3}\text{s}^{-1}$. A diagnostic formulation of J describing the freezing rate of supercooled aerosol particles per unit time and per unit volume of aerosol is proposed in Koop et al. (2000). The nucleation rate is of special interest for solving the analytical equation for the change in number density n_i for homogeneous nucleation:

$$\frac{dn_i}{dt} = n_0 J V_0 \quad \text{with} \quad V_0 = \frac{4\pi r_0^3}{3}. \quad (2.1)$$

The initial volume V_0 with the typical freezing aerosol radius $r_0 = 0.25\mu\text{m}$ and the aerosol number density prior to freezing n_0 , where realistic values are $100\text{-}300\text{cm}^{-3}$ (Minikin et al. (2003), Spichtinger and Gierens (2009a)). In order to calculate the nucleation rate it has to be noted that the relative humidity RH_w is equal to the water activity a_w when pure liquid bulk water is in equilibrium to water vapour. The water activity a_w is the ratio of the vapor pressure of the solution to the water pressure of pure water at the same temperature. Thus a_w gives the temperature-, concentration-, and pressure- dependent water activity of a solution, in this case H_2SO_4 , and $RHi(T, p)$ of ice. Setting $RH_w = a_w$, the nucleation rate is then calculated by Koop et al. (2000)

$$\log(J) = -906.7 + 8502\Delta RH_w - 26924(\Delta RH_w)^2 + 29180(\Delta RH_w)^3 \quad (2.2)$$

with $\Delta RH_w = RH_w - RHi$. The relative humidity with respect to ice is calculated by $RHi = (e_v/e_{si}(T))100\%$, whereas the frequently used ice saturation ratio is $S_i = RHi/100$, analogue for water.

This is implemented in a parcel model introduced in Sec. 3.1. In Fig. 2.3 the number densities resulting from the nucleation rate for different temperatures in a rising air parcel is depicted. Homogeneous nucleation is triggered at pressures below 350hPa and temperatures approximately below 235K (Kärcher and Lohmann, 2002) thus the values are chosen accordingly. Exemplarily the critical nucleation rate for $S_{i,cr}$, namely $J_{cr} = 3(4\pi r_0^3 \Delta t)^{-1}$ results in $J_{cr} \approx 10^{10}\text{cm}^{-3}\text{s}^{-1}$ for the typical time step for general circulation models (GCM) of $\Delta t = 20\text{min}$ (Kärcher and Lohmann, 2002). In Tab. 7.2. in Pruppacher and Klett (1997) this approximated nucleation rate J_{cr} is reached for a supercooling of about 39°C which agrees well with the Koop et al. (2000) results. As Jensen and Toon (1994) state, the nucleated ice crystal number is insensitive to the number of available aqueous aerosols as the competition for water vapour causes the event to cease.

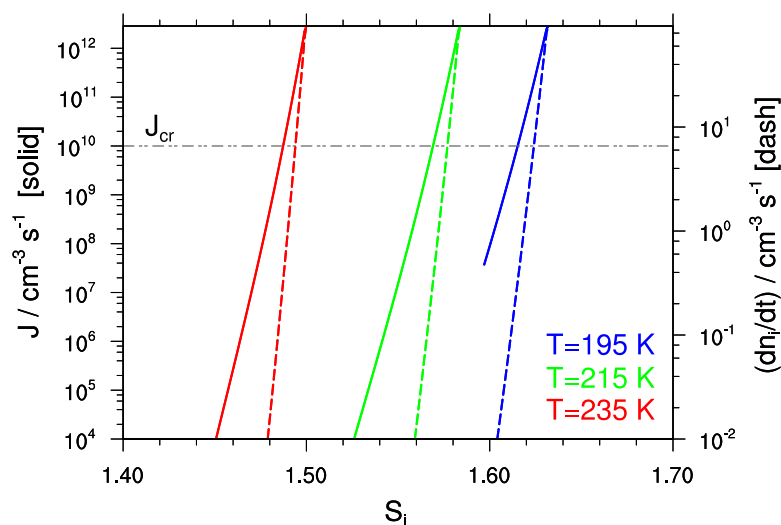


Figure 2.3: The dependency of the homogeneous nucleation rate (Koop et al., 2000) on the temperatures $T = 195, 215, 235$ K and the ice supersaturation ratio and the resulting ice crystal density rates. The initial background aerosol is set to the high value of $n_0 = 500 \text{ cm}^{-3}$ in order to prevent a limiting effect on the nucleation rate. The dashed reference line shows the critical nucleation rate J_{cr} from Kärcher and Lohmann (2002).

This empirical approach to classical theory is introduced in order to clarify the homogeneous nucleation process. High relative humidities correlate to high nucleation rates causing a high ice crystal number densities, see Fig. 2.3. The described Koop et al. (2000) scheme is a good approach for validating a homogeneous nucleation parameterisation as it explicitly resolves the ice crystal number density.

2.2.2 Heterogeneous Nucleation

Heterogeneous freezing requires the presence of ice nuclei (IN) which reduce the energy barrier to form a new phase. Typically available in the atmosphere are dust, soot and organic substances and experimental studies proved volcanic ash to be an efficient IN (Fornea et al., 2009). A characteristic IN concentration in the upper troposphere is $0.01\text{-}100 \text{ dm}^{-3}$ which is low compared to the total of available aerosol (Hoose et al., 2010). Ice nuclei concentrations of $1000\text{-}20000 \text{ dm}^{-3}$ do not automatically generate ice particles but, furthermore, cloud top temperatures must usually decrease to -20°C before significant heterogeneous ice nucleation takes place (Ansmann et al., 2008).

The four fundamental kinds of heterogeneous freezing processes are contact, immersion, condensation and deposition nucleation (see Fig. 2.2). Vali (1985) distinguishes the nucleation processes as follows:

- *Deposition nucleation* The formation of ice in a (supersaturated) vapour environment.

- *Freezing nucleation* The formation of ice in a (supercooled) liquid environment:
 - *Condensation freezing* The sequence of events whereby a cloud condensation (CCN) initiates freezing of a condensate.
 - *Contact freezing* Nucleation of a supercooled droplet subsequent to an aerosol particle coming into contact with it.
 - *Immersion freezing* Nucleation of supercooled water by a nucleus suspended in the body of water.

Ladino and Abatt (2013) investigated deposition nucleation between 223 K and 203 K in the presence of dust and found that the barrier to deposition nucleation becomes larger at lower temperatures with the critical ice supersaturation ratio exceeding 1.7 for 203 K, surpassing the homogeneous nucleation threshold which is 1.56 for this temperature (Koop et al. (2000), Ren and MacKenzie (2005)). The most efficient nucleation mode for cirrus formation is thought to be immersion freezing (e.g., Gierens (2003), Kärcher and Lohmann (2003)), which is not easily distinguishable from condensation freezing needing water saturation.

Ice nuclei are grouped according to their diameter size into the coarse mode $D > 2.5 \mu\text{m}$ and fine mode $D < 2.5 \mu\text{m}$ which is subdivided into the nucleation mode (also known as Aitken) particles $D < 0.1 \mu\text{m}$ and the accumulation mode germs $0.1 \mu\text{m} < D < 2.5 \mu\text{m}$ (Whitby and Cantrell, 1976). Insoluble particles like soot accumulate in the nucleation mode while dust particles are primarily found in the coarse mode (Ansmann et al., 2008).

Classical nucleation theory has been applied to heterogeneous freezing with supercooled water on an IN (e.g., Khvorostyanov and Curry (2004), Eastwood et al. (2008)). Nevertheless, it is still assumed to have some shortcomings in particular involving contact and immersion freezing (Fornea et al., 2009). As a result, the classical theory approach for heterogeneous nucleation rates is still object of current discussions (Curry and Khvorostyanov, 2012). Thus a parameterisation taking into account different species of IN and the sensitivity towards cooling and saturation is desirable. Parameterisations for heterogeneous nucleation are introduced in Sec. 3.2.2.

2.2.3 Competition

The interaction between homogeneous and heterogeneous nucleation is of particular interest for cirrus development. Competition is caused by heterogeneous freezing commencing at warmer temperatures and, depending on the amount and hygroscopicity of the aerosols available, depleting the ice supersaturation before homogeneous freezing is triggered. Thus the existence of IN reduces cloud ice number (Haag and Kärcher, 2004). An overview as well as their competition can be seen in Fig. 2.4 (Ren and MacKenzie, 2005). Shown is the development of ice supersaturation over time of an adiabatically rising air parcel. Depending on the atmospheric conditions, i.e. temperature, number of ice nuclei, pressure and vertical velocity, the thresholds for the ice nucleation regimes can be reached. In this case S_0 denotes the commence of freezing

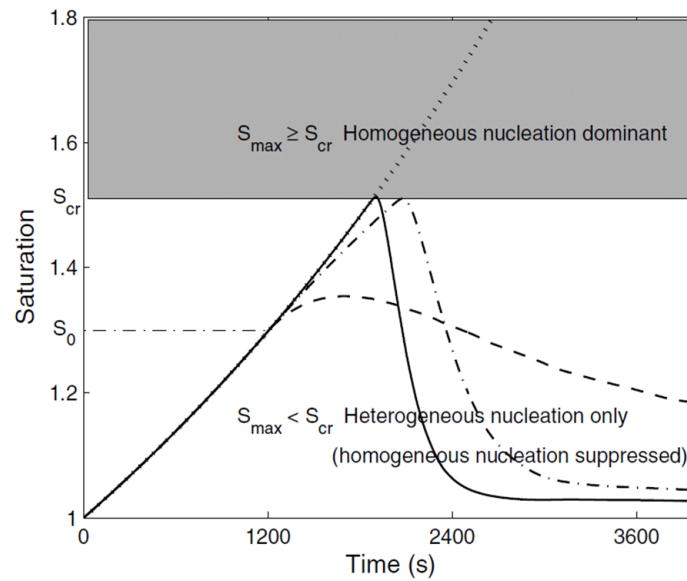


Figure 2.4: Overview of the triggering of the ice nucleation processes considering an adiabatically lifted air parcel over time (Fig. from Ren and MacKenzie (2005)). Due to cooling, the threshold ice supersaturation ratios S_0 for heterogeneous or, in this plot, S_{cr} for homogeneous freezing are reached. In the case of a rapidly ascending parcel both mechanisms can be triggered causing a competition of the ice crystals for available water vapour (depicted by the dash-dotted line).

accounting for ice nuclei and S_{cr} the triggering of homogeneous nucleation. In Fig. 2.4 the exponentially rising dotted line represents the case in which no nucleation were to take place. The solid line demonstrates the nucleation with no present ice nuclei. The dashed and the dashed-dotted line both depict freezing commencing at S_0 . The difference is that the dashed line represents heterogeneous nucleation which is capable of removing the supersaturation while in the case of the dashed-dotted line the homogeneous nucleation threshold $S_{i,cr}$ is reached.

In young cirrus there is a competition between generating supersaturation by the cooling of the air parcel due to updraft and reducing the saturation due to depositional growth. Once the threshold for nucleation is reached, depositional growth commences and depletes the ice supersaturation. As stated in Krämer et al. (2009), the chemical bond of the available ice-forming aerosols may determine the freezing thresholds to trigger either nucleation. Critical supersaturations for heterogeneous and homogeneous freezing derived from classical theory are given in Khvorostyanov and Curry (2009).

2.3 Ice Supersaturated Regions

Ice supersaturated regions (ISSRs) have been identified in the past as cloud free air masses in the upper troposphere that exceed saturation with respect to ice (Spichtinger, 2004). However, ice supersaturation was found to also occur in cirrus clouds and differences in the detection

limits of the instruments lead to discrepancies in measurements concerning in-cloud and cloud-free air masses. Using a Mobile Aerosol Raman Lidar (MARL) with a detection limit for ice clouds with an optical depth of less than 10^{-4} , Immler et al. (2008) found that ISSRs almost always contain ice particles.

ISSRs are mostly confined to the layer beneath the tropopause, which is susceptible to seasonal features (Gierens et al., 2012). ISSRs were detected to occur most frequently in the pressure levels 147 and 215 hPa by using Microwave Limb Sounder (MLS) data (Spichtinger et al., 2003b). In the tropics they are frequently found in both pressure levels, while ISSRs are mostly detected at 215 hPa in the mid-latitude storm tracks during boreal summer and autumn (Spichtinger et al., 2003b). According to data from the Measurement of Ozone by Airbus in-service Aircraft (MOZAIC) project, these regions have a broad horizontal size with a mean path length of about 150 km (Gierens and Spichtinger, 2000), while their vertical extension is 1 – 2 km (Spichtinger et al., 2003a). The vertical depth of the ISSR decreases mainly with temperature, which explains the occurrences of thicker ISSRs in higher latitudes (Gierens et al., 2012).

Ice supersaturation is required for forming ice crystals via ice nucleation and is also responsible for subsequent growth through depositional growth. Thus cirrus, as well as contrail formation and lifetime, highly depend on the existence of ice supersaturation. Furthermore, subvisible cirrus (SVC) is also frequently embedded in ISSRs (Gierens and Spichtinger, 2000) only having optical depths of $\tau_c < 0.03$ and ice particles of about $< 50 \mu\text{m}$ diameter (Lynch and Sassen, 2002). The correlation of ice supersaturated regions with cloudiness is also important for the radiation budget. Fusina et al. (2007) state that through thin cirrus in ISSRs changes in the outgoing longwave radiation (OLR) up to 64 W m^{-2} and a difference in the reflected shortwave flux of 79 W m^{-2} are possible. Thus a correct representation of ice supersaturation and the regions of its occurrence is essential to be included in numerical weather prediction models.

Chapter 3

Methodology

In order to describe the nucleation mechanisms introduced in Sec. 2.1, state-of-the-art parameterisations are described in this chapter. They are tested and further adaptations are made in order to fulfil the requirement of achieving a more physical treatment of ice supersaturation in numerical weather prediction models. The simulated cloud ice properties depend on the choice of parameterisation for the homogeneous and heterogeneous nucleation. The triggering of which is controlled by the updraft causing an adiabatic cooling which in turn augments ice supersaturation. If a sufficient amount of ice nuclei (IN) is available, homogeneous nucleation can be suppressed by pre-existing heterogeneously formed ice. This behaviour is accounted for by introducing a budget variable for activated IN. After nucleation has been triggered, diffusional growth on the ice particles depletes the ambient water vapour. When the mass of ice crystals is sufficiently large the particles sediment, thereby restructuring the cloud. These effects are dominant in cirrus cloud formations and dynamics and consequently have to be accounted for.

For a better understanding of the ice cloud processes, they are investigated within an isolated parcel model environment. First, the two-mode two-moment cloud ice microphysics scheme and parcel model setup will be introduced. Then the parameterisations for the ice nucleation and the subsequent depositional growth and ramification of ice supersaturation will be discussed. Next a tracking variable for nucleated heterogeneous ice is introduced and the terminal vertical velocity for sedimenting ice crystals is discussed. The theory will be explained consecutively while the applications of these modifications to Numerical Weather Prediction (NWP) models will be shown in Chap. 4. As the parameterisations and modifications are meant to improve the operational NWP models of the German Weather Service (DWD) the alterations are compared to the currently implemented methods wherever possible.

3.1 Parcel Model Framework

In order to study the effects and sensitivities of the different nucleation mechanisms a parcel model for a two-moment two-mode cloud ice scheme is implemented to investigate var-

ious aspects of the parameterisations. Hereby an air parcel lifted dry adiabatically in upper-troposphere conditions is studied. Of interest for the calculations are the ice saturation ratio S_i , the ice crystal number density n_i , the ice particle radius r_i and resulting mass m_i . The air parcel rises with a constant velocity w where the adiabatic cooling causes the ice saturation ratio S_i to increase. The ice saturation ratio is defined as

$$S_i = \frac{e_v}{e_{si}(T)} \quad (3.1)$$

with e_v and e_{si} being the vapour pressure and the saturation vapour pressure over ice calculated using the Murphy and Koop (2005) parameterisation. An increase in S_i can either trigger heterogeneous nucleation if a sufficient amount of ice nuclei is available or homogeneous freezing if high vertical velocities are present. Once ice crystals are formed, depositional growth decreases the water vapour mixing ratio q_v , thereby depleting the ice supersaturation.

The initial conditions are specified by the pressure p , the temperature T , the vertical velocity w and the ice saturation ratio S_i . Additional parameters are the time step Δt , the set number density of liquid aerosol particles (1000 cm^{-3}) and background aerosol particles that potentially act as ice nuclei (IN) ($1\text{-}30 \text{ dm}^{-3}$). A monodisperse distribution and an initial aerosol particle radius prior to freezing of $r_{i,0} = 0.25 \mu\text{m}$ is assumed. The initial particles are considered spherical and thus the mass $m_{i,0}$ of the ice particles is calculated through

$$m_{i,0} = \frac{4\pi}{3} \rho_i r_{i,0}^3 \quad (3.2)$$

with the ice particle mass density $\rho_i = 0.925 \times 10^3 \text{ kg m}^{-3}$.

Depending on ambient conditions, cloud ice freezing is triggered and quantified by ice crystal number densities $n_{i,\text{hom}}$ and $n_{i,\text{het}}$ with the ice mass mixing ratios $q_{i,\text{hom}}$ and $q_{i,\text{het}}$ for homogeneous and heterogeneous nucleation, respectively. The temporal evolution of the freezing process is described by a conservation equation for the water mass and the temperature equation incorporating latent heat release and adiabatic cooling:

$$0 = \frac{dq_v}{dt} + \frac{dq_{i,\text{hom}}}{dt} + \frac{dq_{i,\text{het}}}{dt} \quad (3.3)$$

$$\frac{dT}{dt} = \frac{dq_v}{dt} \frac{L_s}{c_p} - \frac{g}{c_p} w \quad (3.4)$$

where $g = 9.81 \text{ m s}^{-2}$ is the acceleration by gravity and $c_p = 1005 \text{ J kg}^{-1} \text{ K}^{-1}$ the specific heat capacity of air at constant pressure and $L_s = 2.836 \times 10^6 \text{ J kg}^{-1}$ is the latent heat of sublimation. The equations are numerically integrated using the Euler forward scheme. This model is the environment in which the parameterisations and other relevant processes are discussed.

3.2 Cloud Ice Nucleation

A great variety of parameterisations for heterogeneous and homogeneous freezing of supercooled aerosols exist in the literature. In the following, the emphasis lies on the parameterisation for homogeneous nucleation developed by Kärcher et al. (2006, KHL06 hereafter), which

takes into account pre-existing ice crystals from heterogeneous freezing. The latter is included by use of an empirical parameterisation which is thoroughly described in Phillips et al. (2008). In order for the parameterisation to be valid for all mesoscale NWP models, an adaption is made for numerical stability to be assured over all time steps. The formation of cirrus clouds is then investigated by use of the parcel model. In order to gain an indication for the quality of the parameterisations, further approaches are implemented. As homogeneous freezing of liquid aerosols is currently not included in the DWD models, the explicit approach of Koop et al. (2000) is considered for comparison. The heterogeneous nucleation scheme is compared to a modified Fletcher formula (Fletcher, 1962) which is operational in the DWD NWP models. The nucleation processes as well as their competition will next be introduced and analysed separately. The various schemes are then discussed and evaluated.

3.2.1 Parameterisation of Homogeneous Nucleation

In the NWP models at the DWD, cloud water is assumed to freeze homogeneously at temperatures below -37°C while freezing of liquid aerosols is not yet included in the microphysical scheme. In the following, the most important equations from the KHL06 scheme will be introduced for e.g., the critical ice supersaturation ratio $S_{i,\text{cr}}$, the ice crystal number density n_i , the ice crystal radius r_i , and the fictitious vertical velocity w_p , which accounts for pre-existing ice particles. Special attention is paid to the different timescales for the processes taking place during the homogeneous nucleation. For verification, the KHL06 scheme is compared to Koop et al. (2000) in which the nucleation rate is parameterised and the ice crystal number density is explicitly calculated (see Sec. 2.2.1).

The challenge to correctly model homogeneous nucleation lies in the differing timescales related to the nucleation event. These include the model time step Δt , the point in time where homogeneous nucleation is triggered t_{cr} , the period of the freezing event τ_{freez} and the length of depositional growth τ_{dep} depicted in Fig. 3.1. Typical values are $\tau_{\text{freez}} = 17.38\text{ s}$ and $\tau_{\text{dep}} = 2000\text{ s}$ for the temperature $T = 220\text{ K}$ and the vertical velocity of $w = 10\text{ cm s}^{-1}$. The timescales for process-oriented models are typically $\Delta t < \tau_{\text{freez}} < \tau_{\text{dep}}$ while for climate models and the Integrated Forecast System (IFS) of the European Center of Mediumrange Forecast (ECMWF) it is $\tau_{\text{freez}} < \tau_{\text{dep}} < \Delta t$. In the current IFS scheme based on Tompkins et al. (2006), the homogeneous nucleation is assumed to be triggered as soon as the critical supersaturation is reached. The relative humidity with respect to ice is then reduced to 100% within the same model time step. Thus as soon as nucleation is triggered the ice supersaturation is depleted and no in-cloud supersaturation remains. When applying the homogeneous nucleation parameterisation to the DWD models it has to be valid for both regimes, i.e. the high resolution regional COSMO model with $\Delta t = 23\text{ s}$ and the global model GME with $\Delta t = 133\text{ s}$ where the sequence of timescales may

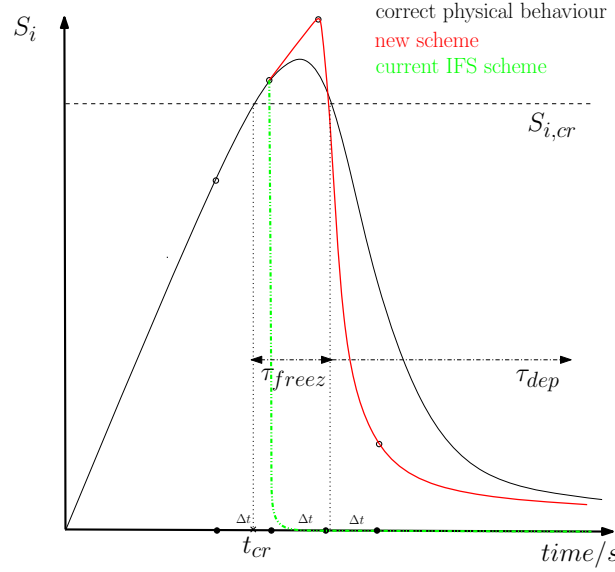


Figure 3.1: The timescales t_{cr} , τ_{freez} and τ_{dep} are sketched in relation to an arbitrary model timestep Δt marked by \circ . Shown is the correct physical behaviour of the ice supersaturation evolution (black), the new cloud ice scheme (red) and the current IFS scheme (green). Difficulties arise when the model time step Δt is too large to fully resolve the freezing event but too small to entirely capture the freezing event.

vary between

$$\Delta t \approx \tau_{freez}, \quad (3.5)$$

$$\Delta t < \tau_{freez} < \tau_{dep} \quad \text{and} \quad (3.6)$$

$$\tau_{freez} < \tau_{dep} < \Delta t. \quad (3.7)$$

In order to take these scale differences into account and avoid double counting, it is necessary to specify the time t_{cr} at which the threshold for the homogeneous nucleation event $S_{i,cr}$ is exceeded. This critical ice supersaturation ratio

$$S_{i,cr} = 2.349 - \frac{T}{259.00K} \quad (3.8)$$

is a temperature dependent analytical fit from Ren and MacKenzie (2005) based on the results from Koop et al. (2000). As the KHL06 parameterisation takes the competition between the two processes into account a second condition has to be fulfilled. Namely that the model updraft w is larger than a fictitious vertical velocity w_p accounting for pre-existing ice particles

$$w_p = \frac{a_2 + a_3 S_i}{a_1 S_i} R_i, \quad w_p \geq 0 \quad (3.9)$$

with

$$a_1 = \frac{L_s M_w g}{c_p R T^2} - \frac{M g}{R T}, \quad a_2 = \frac{1}{n_{sat}} \quad \text{and} \quad a_3 = \frac{L_s^2 M_w m_w}{c_p p T M}. \quad (3.10)$$

The parameters needed in the following are latent heat of sublimation $L_s = 2.836 \times 10^6 \text{ J kg}^{-1}$, molecular mass of water $M_w = 18 \times 10^{-3} \text{ kg mol}^{-1}$, universal gas constant $R = 8.314$

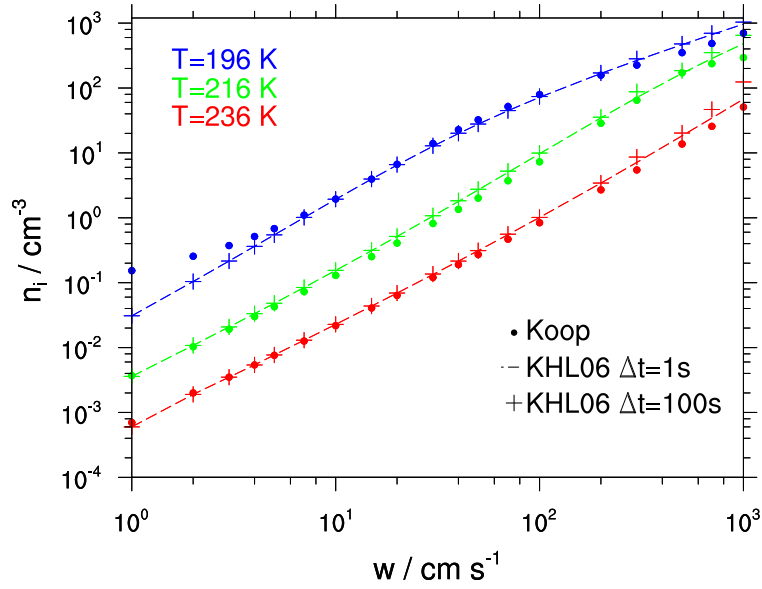


Figure 3.2: For homogeneous nucleation a clear proportionality between the ice crystal number density and the vertical velocity is depicted. The setup is chosen as in KL02 with $p = 220$ hPa and large initial aerosol number density n_0 always being higher than $n_{i,\text{hom}}$. Shown are the simulated values using the Koop et al. (2000) parameterisation and the KHL06 parameterisation with the additional conditions listed in Eq. (3.20)-(3.23).

$\text{J mol}^{-1} \text{K}^{-1}$, molecular mass of air $M = 29 \times 10^{-3} \text{ kg mol}^{-1}$ and the mass of a water molecule $m_w = 3 \times 10^{-26} \text{ kg}$. The term $n_{\text{sat}} = e_{\text{si}}/(k_b T)$ denotes the number density at saturation per unit volume, where $k_b = 1.38065 \times 10^{-23} \text{ J K}^{-1}$ is the Boltzmann constant. As lower velocities cause lower ice supersaturations, reducing the velocity has the same effect as nucleated crystals that dismantle the saturation due to depositional growth. The freezing or growth term used in Eq. (3.10) is given by

$$R_i = \frac{4\pi}{v_i} n_i r_i^2 \frac{dr_i}{dt}, \quad (3.11)$$

where $v = 3.234 \times 10^{-29} \text{ m}^{-3}$ denotes the specific volume of a water molecule with respect to ice and the depositional growth \dot{r}_i as defined in the kinetic equation used by Kärcher and Lohmann (2002, KL02 hereafter), see Sec. 3.3.

In the case of $w < w_p$ any further nucleation is suppressed. The sensitivity of the cloud ice number density n_i towards w is shown in KL02 where the following relation is derived

$$n_i \propto w^{3/2} n_{\text{sat}}^{-1/2}. \quad (3.12)$$

This supports the approach of accounting for pre-existing ice through the artificial downdraft term w_p . The dependence of the ice crystal numbers on the vertical velocity is also depicted in Fig. 3.2 for different temperatures. Shown are the KHL06 scheme for model time steps $\Delta t = 1$ s and $\Delta t = 100$ s as well as the Koop parameterisation with an adaptive time step for the nucleation event. The high number densities for low vertical velocities and $T = 196$ K in the Koop

scheme are due to the high initial number of background aerosols $n_0 = 1000 \text{ cm}^{-3}$ which enters Eq. (2.1). With more realistic values such as $n_0 = 100 \text{ cm}^{-3}$ the Koop line (not shown) matches the KHL06 lines. The impact of a different initial pressure due to diffusion, aerosol geometric mean size and distribution on the n_i - w relationship are thoroughly discussed in Spichtinger and Gierens (2009a). The ice crystal number density from the KHL06 parameterisation is

$$n_{i,\text{hom}} = \frac{a_1 S_{i,\text{cr}}}{a_2 + a_3 S_{i,\text{cr}}} (w - w_p) R_{im}^{-1}, \quad (3.13)$$

where

$$R_{im} = \frac{4\pi b_1}{v} \frac{b_2}{b_2^2} \frac{\delta^2}{1 + \delta} \left[1 - \frac{1}{\delta^2} + \frac{1}{\delta^2} \left(\frac{(1 + \delta)^2}{2} + \frac{1}{\kappa} \right) f(\kappa) \right] \quad (3.14)$$

is the freezing or growth integral analytically solved for a set radius r_0 . Subsequently the used terms will be introduced. The function $f(\kappa)$ is an asymptotic expansion including an analytically derived errorfunction to prohibit divergence when κ is close to 1 (see detailed derivation in Ren and MacKenzie (2005)). The terms $b_1 = v\alpha_d v_{\text{th}} n_{\text{sat}} (S_i - 1)/4$ and $b_2 = \alpha_d v_{\text{th}} / (4D_v C)$ with the thermal speed of water molecules v_{th} , the diffusion coefficient of water vapour in the air D_v and the capacitance $C = 1$ for spherical particles. The deposition coefficient is set to $\alpha_d = 0.5$ which will be thoroughly discussed in Sec. 3.3.1. In Eq. (3.14), δ is the dimensionless ice particle size parameter. The dimensionless parameter κ is the ratio of timescales of the initial growth and freezing timescale and is used for distinguishing between the slow and fast growth regime ($\kappa \ll 1$ slow growth regime, $\kappa \gg 1$ fast growth regime). It depends on the vertical velocity and the particle size conditions:

$$\delta = b_2 r_0, \quad \kappa = \frac{2b_1 b_2}{1 + \delta} \tau_{\text{freez}}. \quad (3.15)$$

Once the requirements for homogeneous freezing are fulfilled the characteristic timescale from KL02 for the freezing event depicted in Fig. 3.1 is

$$\tau_{\text{freez}}^{-1} = \left(\frac{\partial \ln(J)}{\partial T} \right)_{S_i=S_{i,\text{cr}}} \frac{dT}{dt}. \quad (3.16)$$

Inserting the adiabatic cooling rate and the parameterisation for the change of nucleation rate with temperature as stated in Ren and MacKenzie (2005) yields

$$\tau_{\text{freez}}^{-1} = [T(0.004T - 2) + 304.4] \frac{g w}{c_p}. \quad (3.17)$$

In order to determine the time of the nucleation event several variations are included. First, the time interval is determined, in which the critical value of $S_{i,\text{cr}}$ is reached. In KL02 the time interval between the initial value S_0 and the reaching of the critical saturation $S_{i,\text{cr}}$ is given. Replacing S_0 with the value for S_i of the current time step will give the remaining time until the critical saturation is reached:

$$t_{\text{cr}} = \frac{1}{a_1 w} \ln \left(\frac{S_{i,\text{cr}}}{S_i} \right). \quad (3.18)$$

Combining Eq. (3.17) and Eq. (3.18) determines the duration of the nucleation event. If $(t_{\text{cr}} + \tau_{\text{freez}}) < \Delta t$ the nucleation event is captured within the next model time step. The supersaturation at the end of the next time step is estimated by the extrapolation from KHL06

$$S_i(t + \Delta t) = S_i + a_1 S_i(w - w_p)\Delta t. \quad (3.19)$$

Thus $t_{\text{cr}} + \tau_{\text{freez}}$ determines when a nucleation event occurs and only if $S_i(t + \Delta t) > S_{i,\text{cr}}$ will the nucleation event take place at the current time step. In summary the homogeneous nucleation event is triggered if the four conditions are fulfilled:

$$1) S_i > S_{i,\text{cr}} \quad (3.20)$$

$$2) w > w_p \quad (3.21)$$

$$3) t_{\text{cr}} + \tau_{\text{freez}} < \Delta t \quad (3.22)$$

$$4) S_i(t + \Delta t) > S_{i,\text{cr}}. \quad (3.23)$$

While 1) and 2) were already predefined conditions from KHL06, points 3) and 4) are newly implemented. This leads to a physically based approach to capture the characteristic ice supersaturation overshoot to occur in the parcel model which is important for NWP models with a model time step of $\Delta t \approx 100$ s. Using only the original criteria 1) and 2) from Eq. (3.20)- (3.23) would result the nucleation event to be triggered as soon as $S_{i,\text{cr}}$ is reached. Yet higher ice supersaturation values are possible through the extension of the criteria. In Haag et al. (2003) this higher peak in S_i above $S_{i,\text{cr}}$ is explained to be a non-equilibrium effect which is shown to increase with decreasing temperature. This is due to slower ice particle growth and continuous cooling during the constant lifting of the parcel.

In KHL06 the variations of the ice crystal radius for the timescale of the freezing event τ_{freez} and the model time step Δt are taken into account in order to improve the result of the ice particle diameter. When nucleation commences the radius $r_i(\tau_{\text{freez}})$ is calculated by use of the KHL06 parameterisation. The next value of interest is the ice crystal radius $r_{i,\infty}$ for $t \rightarrow \infty$ proposed in KL02, which also takes commencing depositional growth into account. By using the ice water mass

$$m_{i,\infty} = \frac{\pi}{6} m_w \frac{a_1 S_{i,\text{cr}}}{a_2 + a_3 S_{i,\text{cr}}} w \tau_{\text{freez}} + m_w n_{\text{sat}}(S_{i,\text{cr}} - 1) \quad (3.24)$$

the mean ice particle radius results in

$$r_{i,\infty} = \left(\frac{3m_{i,\infty}}{4\pi\rho_i n_{i,\text{hom}}} \right)^{1/3} \quad (3.25)$$

The intermediate radius for the model time step $r_i(\Delta t)$ is then determined by iteration between $r_i(\tau_{\text{freez}})$ and $r_{i,\infty}$.

The comparison of the KHL06 scheme including the alteration for the triggering of the homogeneous nucleation event to Koop et al. (2000) is shown in Fig. 3.3. The latter scheme is hereby considered as the 'truth' as it uses a diagnostic nucleation rate based on a classical nucleation

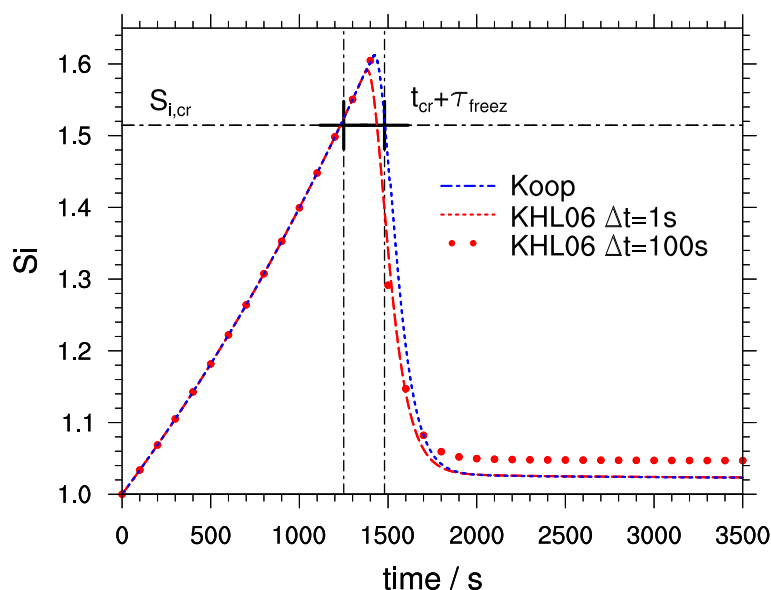


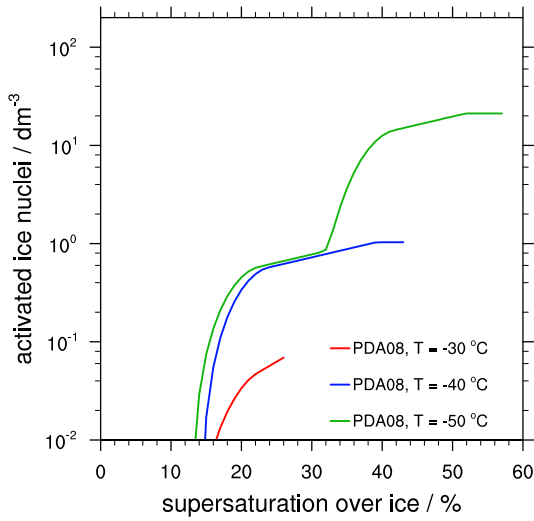
Figure 3.3: The development of ice supersaturation over time with the initial conditions $T = 220$ K, $p = 220$ hPa and a constant updraft $w = 25$ cm s^{-1} causing homogeneous nucleation to be triggered at $S_{i,\text{cr}}$. The KHL06 homogeneous nucleation is compared to the Koop scheme (Koop et al., 2000) using the time steps $\Delta t = 1$ s and $\Delta t = 100$ s. The overshoot is captured as the nucleation event is delayed to occur in the last critical saturation time step taking $t_{\text{cr}} + \tau_{\text{freez}}$ into account.

scheme and an adaptive time step around the nucleation event. It can be seen that the ice saturation curve shows the same behaviour for the explicitly resolved Koop et al. (2000) scheme as for the KHL06 scheme with time steps $\Delta t = 1$ s and $\Delta t = 100$ s. Only implementing the KHL06 scheme would have caused a triggering of the nucleation event, as soon as $S_{i,\text{cr}}$ is reached. Through the new conditions listed as Eq. (3.22)- (3.23) the scheme becomes robust for larger time steps. Although these conditions only hold under the assumption that the vertical velocity is sufficiently constant. The asymptotic value for $t \rightarrow \infty$ of the ice saturation ratio in Fig. 3.3 does not reach $S_i = 1$ due to the ongoing cooling of the air parcel resulting from the constant updraft. Because of good physical behaviour the KHL06 parameterisation became the scheme of choice and with the modifications it is robust enough for operational applications. The calculation of the pre-existing heterogeneously formed ice crystals which potentially suppresses homogeneous nucleation is described in the following.

3.2.2 Parameterisation of Heterogeneous Nucleation

Heterogeneous nucleation is triggered at warmer temperatures, i.e. $T > -40^\circ\text{C}$, depending on the existence of ice nuclei in the atmosphere, and thus often reduces ice supersaturation before homogeneous freezing can set in. In the past, empirical parameterisations have been developed in which the IN depend on either ice supersaturation (e.g., Meyers et al. (1992)) or on temperature. The latter is also used for the heterogeneous nucleation parameterisation scheme

a) deposition mode



b) condensation/immersion mode

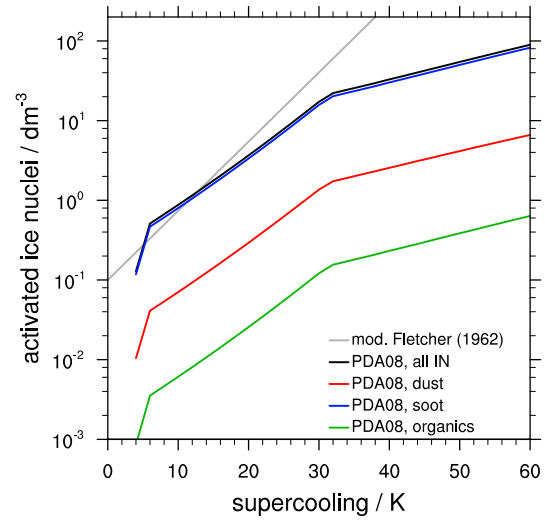


Figure 3.4: The activated ice nuclei for black carbon, insoluble organic carbon and dust/metallic particles according to Phillips et al. (2008) as a function of the supercooled temperature and the ice supersaturation. Plot a) depicts depositional freezing and b) represents the number densities for the condensation and immersion mode for the initial number densities, $DM = 162 \text{ dm}^{-3}$, $BC = 15 \text{ cm}^{-3}$ and $O = 1.77 \text{ cm}^{-3}$ compared to the modified Fletcher (1962) equation.

by Fletcher (1962), which is currently implemented in an altered form in the DWD models. In the following, the modified Fletcher parameterisation is compared to the heterogeneous ice nucleation scheme by Phillips et al. (2008, PDA08 hereafter) with respect to the resulting ice crystal number densities.

In the parameterisation proposed in PDA08, the number densities are derived by using empirical dependencies of aerosol chemistry and accounting for various IN. This is obtained by assuming the active IN to be approximately proportional to the aerosol's total surface area. The data used is constrained by measurements of the continuous flow diffusion chamber (CFDC). In the heterogeneous nucleation scheme, it is explicitly distinguished between inorganic black carbon (BC), insoluble organic carbon (O) and dust/metallic aerosols (DM). This permits a coupling to aerosol model climatologies in the future. In the parcel model the initial number densities for the IN are set as proposed in PDA08, namely $n_{DM} = 162 \text{ dm}^{-3}$, $n_{BC} = 15 \text{ cm}^{-3}$ and $n_O = 1.77 \text{ cm}^{-3}$. These values are based on six field campaigns. Sensitivity studies concerning the initial IN values and their influence in NWP models will be conducted in the following chapters.

The scheme takes into account the model temperature, pressure, water vapour mixing ratio and supersaturation ratio. The concentration of active IN from species X (i.e. DM, BC and O) within a size interval $d \log D_X$ as described in detail in PDA08 is

$$n_{IN,X} = \int_{\log[0.1 \mu\text{m}]}^{\infty} (1 - \exp[\mu_X(D_X, S_i, T)]) \frac{dn_X}{d \log D_X} d \log D_X, \quad (3.26)$$

which is valid for $T < 0^\circ\text{C}$ and $1 < S_i \leq S_{i,w}$ where $S_{i,w}$ is the value for water saturation.

The function μ_X comprises various relations for the modes and surface area giving the average number of activated embryos per insoluble aerosol particle with the size D_x . The resulting activated ice nuclei number densities for the deposition and condensation/immersion modes in dependence of supersaturation over ice and supercooling is depicted in Fig. 3.4. The organic substances show the greatest impact for the deposition mode while soot is the dominant IN in the condensation/immersion mode.

The frozen ice nuclei fractions $n_{\text{frac},X}$ of the individual groups are calculated by dividing the nucleated ice crystal concentration through the total initially available number of ice nuclei for each species IN_X . The total heterogeneously nucleated number density $n_{i,\text{het}}$ then yields

$$n_{i,\text{het}} = \sum IN_X n_{\text{frac},X}. \quad (3.27)$$

Larger particles have a higher nucleation efficiency due to more effective and active sites. The assumed minimum diameter for an IN is $D_i = 0.1 \mu\text{m}$. Comparisons presented in PDA08 show that the resulting number concentrations for heterogeneously nucleated ice crystals lie in the same range as the Lohmann and Diehl (2006), Liu and Penner (2005), Khvorostyanov and Curry (2004) and Meyers et al. (1992) schemes. A validation and further discussions of this scheme can be found in Eidhammer et al. (2009) and Phillips et al. (2009). In Phillips et al. (2013) a modified approach of this heterogeneous nucleation scheme is given (see also Sec. 6.2.1).

In the operational models at the DWD, the empirical parameterisation of heterogeneous nucleation only depends on T and does not differentiate between the different nucleation modes, i.e. it includes condensation, immersion, contact and deposition freezing in a single equation. The classical Fletcher-formula (Fletcher, 1962) is given by

$$n_{i,\text{het}} = n_0 \exp(0.6(T_0 - T)), \quad n_0 = 0.01 \text{ m}^{-3}, \quad T_0 = 273.15 \text{ K}. \quad (3.28)$$

The ice crystal numbers resulting from Eq. (3.28) at $T \approx -40^\circ\text{C}$ are found to overestimate $n_{i,\text{het}}$ by three orders of magnitude and underestimates the ice nuclei concentrations by about two orders of magnitude at moderately low temperatures $T \approx -10^\circ\text{C}$ (Doms et al., 2004). In order to counteract underestimations at high temperatures, additional so-called ice enhancement (e.g., ice crystal fragmentation, ice splinter production in riming) is implicitly taken into account. The resulting operational parameterisation for the number density for ice crystals (Doms et al., 2007)

$$n_{i,\text{het}}(T) = n_0 \exp(0.2(T_0 - T)), \quad n_0 = 100 \text{ m}^{-3} \quad (3.29)$$

is based on a fit to aircraft measurements in stratiform clouds (Hobbs and Rangno, 1985; Meyers et al., 1992) with n_0 being an empirical parameter. Comparisons of the activated ice nuclei n_{IN} to the PDA08 parameterisation show that for low supercooling values $T < -20^\circ\text{C}$ the number of activated ice nuclei are still overestimated, see Fig. 3.4. Further comparisons of the resulting cloud ice number densities are illustrated and discussed in Sec. 3.2.3. In Sec. 3.4 an additional ice nuclei budget variable for activated IN is introduced.

	New Parameterisations	Operational Parameterisations
Homogeneous Nucleation	$n_{i,\text{hom}} = \frac{a_1 S_{cr}}{a_2 + a_3 S_{cr}} (w - w_p) R_{im}^{-1}$ see Eq. (3.13) Kärcher et al. (2006)	—
Heterogeneous Nucleation	$n_{i,\text{het}} = \sum IN_X n_{\text{frac},X}$ see Eq. (3.27) Phillips et al. (2008)	$n_{i,\text{het}} = n_0 \exp(0.2(T_0 - T))$ see Eq. (3.29) Fletcher (1962) modified

Table 3.1: Overview of the new and operational ice nucleation parameterisations along with their equation for the number densities.

3.2.3 Interaction of Nucleation Processes

In the proposed nucleation scheme, the previously introduced homogeneous parameterisation based on KHL06 is coupled to the heterogeneous nucleation schemes. This will allow a competition between the processes, which results in a more realistic approach. Heterogeneous freezing sets in at warmer temperatures and, depending on the amount and hygroscopicity of the aerosols available, may reduce the ice supersaturation before homogeneous freezing is triggered. An overview of the processes as well as their competition was given in Sec. 2.2.3 and illustrated in Fig. 2.4. The critical ice crystal number concentration needed in order to suppress subsequent homogeneous freezing is analytically derived by Gierens et al. (2003), Eq. 21, and also by Barahona and Nenes (2009), Eq. 20, for monodisperse ice nuclei based on cloud parcel model equations. The competition between the two nucleation mechanisms in cirrus clouds was also investigated with 2-D simulations by Spichtinger and Gierens (2009b).

Depending on the ambient atmospheric conditions, i.e. pressure, temperature, number of available IN and vertical velocity, either homogeneous, heterogeneous or both freezing mechanisms are triggered. An important aspect in correctly coupling the homogeneous and heterogeneous parameterisations are the different cirrus properties resulting from either regime. Heterogeneous nucleation potentially becomes dominant in contrail and cirrus regions with slow updrafts (Lin et al., 2002). Vertical velocities less than 20 cm s^{-1} are thought to be where heterogeneous nucleation has the maximum impact on cirrus cloud formation whereas homogeneous nucleation gains importance at higher velocities (DeMott et al., 1997).

The main objective is to investigate the different behaviour of the operational parameterisations in the NWP models of the DWD and the new cloud ice nucleation scheme. However, as currently no parameterisation for homogeneous freezing of liquid aerosols is implemented, only the heterogeneous nucleation scheme from PDA08 is compared with the modified Fletcher equation while for homogeneous freezing the KHL06 scheme with altered triggering is solely used, see Tab. 3.1.

In order to investigate the mutual interaction of the two nucleation schemes an intermediate scenario is chosen with the ambient temperature being $T = 230 \text{ K}$, the pressure $p = 220 \text{ hPa}$,

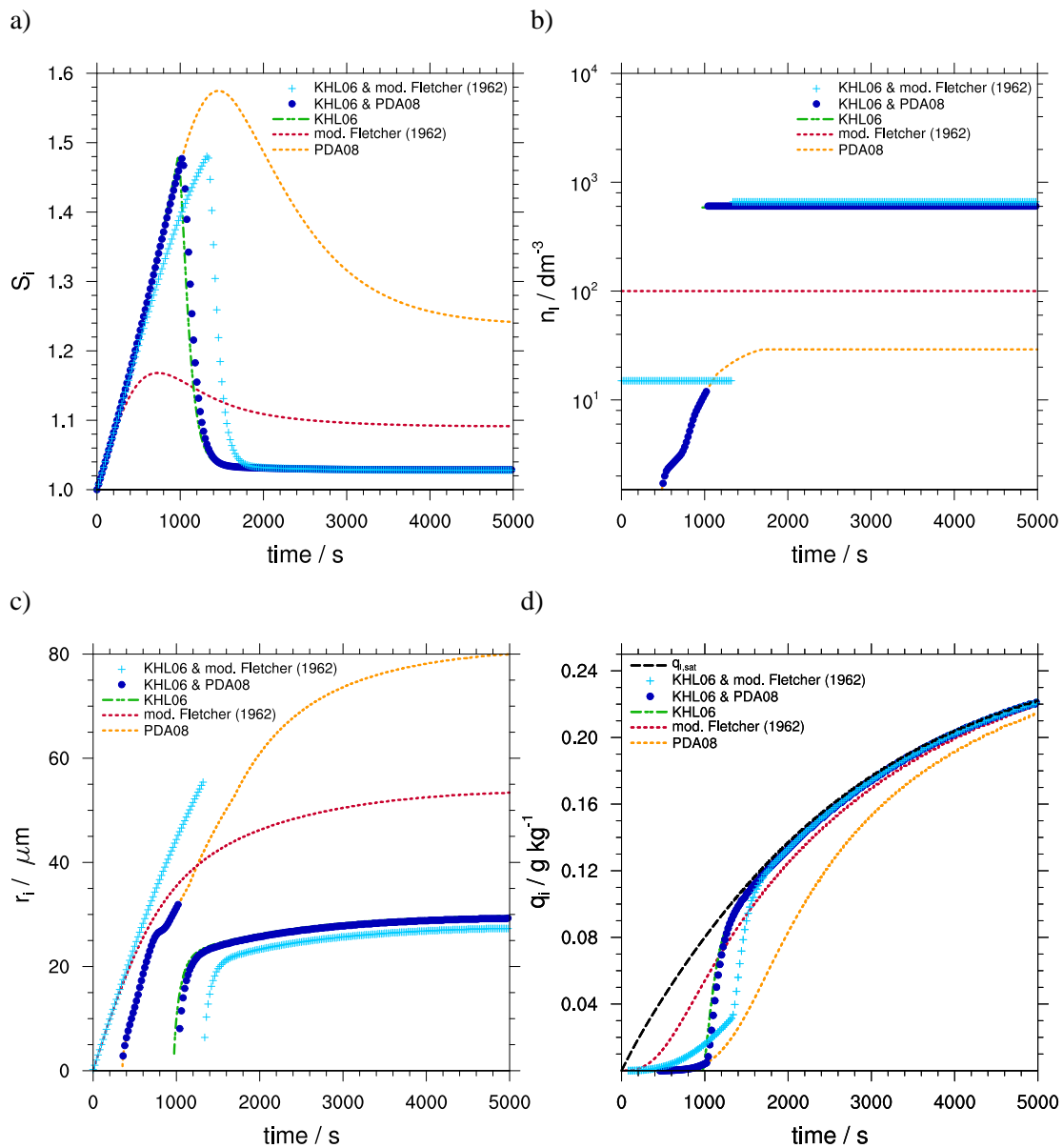


Figure 3.5: Parcel model simulations with the initial values for the temperature $T = 230\text{K}$, the pressure $p = 220\text{hPa}$, and the vertical velocity $w = 40\text{cm s}^{-1}$, which reveal the characteristics of homogeneous and heterogeneous nucleation as well as their interaction. Used are the KHL06 homogeneous nucleation scheme merged once with the heterogeneous schemes applying the modified Fletcher equation and once with PDA08. Different confining maximum values for $n_{i,\text{het}}$ and $n_{i,\text{hom}}$ lead to the competition between the two processes (light and dark blue symbols), purely homogeneous freezing (green line) and solely heterogeneous nucleation (orange and red lines for PDA08 and the modified Fletcher equation, respectively). In a) the ice supersaturation ratio, in b) the ice crystal number density, in c) the ice crystal radius and in d) the cloud ice mixing ratio for the two modes are shown. In d) also the cloud ice mixing ratio for saturation is depicted by the dashed black line.

and the constant vertical velocity $w = 40\text{cm s}^{-1}$. Three scenarios are considered:

- 1) no available ice nuclei (homogeneous freezing)
- 2) upper limit for the activated IN is 100dm^{-3} (heterogeneous freezing)
- 3) upper limit for the heterogeneous ice crystal density $n_{i,\text{het}} = 15\text{dm}^{-3}$ (mixed freezing).

In Fig. 3.5a the development of the ice supersaturation ratio for the above mentioned scenarios over time is shown. The number densities in b) and the cloud ice mixing ratio in d) result from adding the homogeneous and heterogeneously originated particles together. The mean ice crystal radius in Fig. 3.5c is defined by $r_i = \frac{n_{i,\text{hom}}r_{i,\text{hom}} + n_{i,\text{het}}r_{i,\text{het}}}{n_{i,\text{hom}} + n_{i,\text{het}}}$ to stress the differences in particle size for the two ice modes. This definition also explains the gap with abrupt increase in Fig. 3.5c.

The purely homogeneous nucleation case is represented by the green line and is triggered at the critical ice supersaturation ratio $S_{i,\text{cr}} = 1.47$. Regarding the solely heterogeneous nucleation scenario clear differences are noticeable. The ice number crystal concentration resulting from the modified Fletcher equation causes all the available IN to be activated at once reaching the limit $n_{i,\text{het}} = 100\text{dm}^{-3}$ within the first time step (Fig. 3.5b) and quickly depletes the ice supersaturation to its asymptotic value (Fig. 3.5a). This scenario is unrealistic in conjunction with the PDA08 scheme, as the IN are activated over time until $n_{i,\text{het}} = 29\text{dm}^{-3}$ and struggle to reduce the amount of available ice supersaturation (Fig. 3.5a) while homogeneous nucleation is unphysically suppressed. However, this clearly demonstrates the difference in IN activation between the two heterogeneous nucleation schemes. The operational NWP scheme easily overestimates the activated IN for the amount of background aerosol available.

In Fig. 3.5 the light and dark blue lines show the competition between the homogeneous freezing and the activation of IN using the modified Fletcher equation and the PDA08 scheme, respectively. The higher the ice crystal number density resulting from the heterogeneous nucleation, the later homogeneous nucleation is capable of being triggered. This clearly shows the struggle between decreasing ice supersaturation due to existing ice crystals and its increase because of the air parcel's constant lifting depicted in Fig. 3.5a. The ice crystal radius (Fig. 3.5c) plays a great role as well, as the larger heterogeneous ice particles grow slower than the smaller homogeneous ice crystals but deplete the ice supersaturation quicker due to their larger surface area. This is clearly depicted in Fig. 3.5 as the heterogeneously nucleated particles from the modified Fletcher equation cause homogeneous freezing to be postponed. The cloud ice mixing ratios q_i shown in Fig. 3.5d asymptotically approach the dashed black line, which is the cloud ice mixing ratio for saturation $q_{i,\text{sat}}$. This result already indicates that for regions with mature cirrus clouds or with persistent updraft, the cloud ice mixing ratio is going to be similar for both ice nucleation schemes. Yet differences in the cirrus cloud evolution are expected, depicted in Fig. 3.5d where the region of interest is $t < 2000\text{s}$ as the discrepancy between the schemes is the largest here. Especially the cloud ice mixing ratios from the heterogeneous nucleation case depicted by the red and orange line in Fig. 3.5d differ to a large extent. Choosing the modified Fletcher's equation (red line), as it is done in the NWP models of the DWD at the time being, the cloud ice mixing ratios are overestimated for young cirrus, i.e. $t < 1000\text{s}$.

In summary, homogeneous freezing evokes ice particles to have smaller radii but larger number densities while heterogeneous nucleation generates larger but fewer ice particles. After the triggering of the nucleation events the depositional growth plays a major role in the further development of the ice crystals as they compete for the available water vapour in the mixed

regime. To further investigate this phenomenon the equations and the timescales for depositional growth are considered in Sec. 3.3.

3.3 Depositional Growth

After nucleation sets in, the further development of the ice crystals is distinguished by diffusional growth, i.e. deposition/sublimation. Depositional growth is coupled with the release of latent heat causing an increase in buoyancy which potentially increases vertical motion. This in turn will directly affect the supersaturation as it intensifies the water vapour supply for diffusional growth. This feedback motivates the necessity of an accurate physical description. The equations currently accounting for deposition in the DWD models will be explained and compared to different kinetic and thermodynamic approaches. The resulting depositional timescales along with a physical treatment for the ice crystal modes will be discussed thereafter.

3.3.1 Kinetic and Thermodynamic Formulation

In literature there are two different ways of formulating depositional growth, namely the kinetic and thermodynamic formulation. The kinetic formulation is based on gas kinetics where the individual particles are considered. The thermodynamic formulation is based on macro-physical quantities and equilibrium states. These are equivalent formulations yet for smaller ice crystals the kinetic regime is favored while larger ice crystals are rather considered to grow in the thermodynamic regime. Shown in the following, is how the kinetic and thermodynamic formulation relate to each other. A general way of calculating the growth rate of an individual ice crystal is via the change in water vapour mixing ratio q_v and ice mass m_i

$$\frac{dq_v}{dt}\Big|_{\text{dep}} = -\frac{1}{\rho_a} \int_0^\infty \frac{dm_i(r_i)}{dt} f(x, y, z, r_i, t) dr_i \quad (3.30)$$

$$\frac{dm_i}{dt} = 4\pi\rho_i r_i^2 \dot{r}_i \quad (3.31)$$

where $f(x, y, z, r_i, t) dr_i$ denotes the size distribution and $n_i = \int f(x, y, z, r_i, t)$ the number density. In the following, the size distribution is a delta function as the parcel model only accounts for a monodisperse size distribution. With this assumption and after inserting the mass change with respect to the radius, the integral can be simplified to

$$\frac{dq_v}{dt}\Big|_{\text{dep}} = -\frac{n_i \dot{m}_i}{\rho_a} = -\frac{4\pi}{\rho_a} \rho_i n_i r_i^2 \dot{r}_i. \quad (3.32)$$

First, the kinetic regime is considered, which becomes important for particles with radii comparable to the mean free path of air molecules. The kinetic equation for the change in crystal size \dot{r}_i used in Eq. (3.11) based on KL02 is given by

$$\frac{dr_i}{dt} = \frac{m_w}{\rho_i} \frac{\alpha_d v_{\text{th}}}{4} \frac{n_{\text{sat}}(S_i - 1)}{1 + \frac{\alpha_d v_{\text{th}} r_i}{4D_v}} = \frac{b_1}{1 + b_2 r_i}, \quad (3.33)$$

where D_v is the diffusion coefficient of water vapour in air. In Eq. (3.33) the value $\alpha_d = 0.5$ is the deposition coefficient (also named accomodation or kinetic coefficient) of water molecules onto ice particles which are assumed spherical as proposed by Spichtinger and Gierens (2009a). The deposition coefficient is one of the most uncertain parameters in cloud microphysics and is especially important in the kinetic regime (Gierens et al., 2003). Typical values for α_d range from 0.005 to 1, where values lower than 0.1 lead to an insufficient depositional growth resulting in high ice number concentrations and high ice supersaturations (Harrington et al., 2009). The mass accomodation coefficient is an also poorly known correction term in the kinetic growth regime and is normally set to one and is neglected in the following. The deposition and thermal accomodation coefficients both have the function to reduce the effective diffusivity and consequently to slow down the growth of small particles.

Substituting Eq. (3.33) into Eq. (3.32) as well as $S_i = (q_v - q_{v,si})/q_{v,si} + 1$ and $n_{\text{sat}} = e_{si}/k_b T$ results in the kinetic formulation for the change in water vapour mixing ratio restricted to depositional growth

$$\left. \frac{dq_v}{dt} \right|_{\text{dep}} = - \frac{\pi n_i r_i^2 m_w \alpha_d v_{\text{th}} e_{si}}{q_{v,si} \rho_a k_b T \left(1 + \frac{\alpha_d v_{\text{th}} r_i}{4 D_v} \right)} (q_v - q_{v,si}). \quad (3.34)$$

The thermodynamic equation is based on Maxwell's diffusion equation (Maxwell, 1890), which was verified by laboratory studies for frozen prolate spheroids with diameters D_i larger than $100 \mu\text{m}$ (Korolev et al., 2003). Maxwell's diffusion equation is based on steady-state assumptions of a spherical ice crystal in an isothermal surrounding. The formulation as given by Khvorostyanov (1995) and Khvorostyanov and Sassen (1998a, KS98 hereafter) reads:

$$\frac{dr_i}{dt} = \frac{D_v \rho_a C}{\rho_i Q_i r_i \xi_i^2} (q_v - q_{v,si}), \quad (3.35)$$

in which C represents the capacitance and ξ_i the characteristic dimension of crystals. The term $Q_i = 1 + (L_s/c_p)(\partial q_{v,si}/\partial T)$ accounts for psychrometric corrections. When assuming spherical particles $C = \xi_i = 1$ and $Q_i \approx 1$. Inserting Eq. (3.35) into Eq. (3.32) yields the change in mixing ratio

$$\left. \frac{dq_v}{dt} \right|_{\text{dep}} = - \frac{4\pi}{\rho_a} \rho_i n_i r_i^2 \frac{D_v \rho_a C}{\rho_i Q_i r_i \xi_i^2} (q_v - q_{v,si}) \quad (3.36)$$

$$= -4\pi D_v r_i n_i (q_v - q_{v,si}). \quad (3.37)$$

The thermodynamically based depositional rate used in the COSMO model and GME includes the formfactor for hexagonal plates $a_{i,m} = 130 \text{kg m}^{-3}$. The diameter D_i is defined through $m_i = a_{i,m} D_i^3$ and is restricted to $200 \mu\text{m}$. Additionally the Howell factor (Howell, 1948) H_i incorporates the effects coupled to the difference in ambient air and drop temperature and thus thermal diffusivity.

$$\left. \frac{dq_v}{dt} \right|_{\text{dep}} = - \frac{4\pi D_v D_i n_i}{1 + H_i} (q_v - q_{v,si}) \quad (3.38)$$

where

$$H_i = \frac{D_v L_s^2}{K_T R_v T^2} \rho_a q_{v,si}. \quad (3.39)$$

Without accounting for H_i , the equations 3.37 and 3.38 are equivalent.

As it is of interest how the kinetic equation is related to the thermodynamic formulation, the rate of change in radius Eq. (3.33) is converted into Eq. (3.35). The key difference between both equations lies in the factor

$$1 + \frac{\alpha_d v_{th} r_i}{4D_v} \xrightarrow{r_i \rightarrow \infty} \frac{\alpha_d v_{th} r_i}{4D_v}. \quad (3.40)$$

The detailed formulation reads

$$\frac{\alpha_d v_{th} r_i}{4D_v} = \frac{1}{8} \sqrt{\frac{8k_b T}{\pi m_w}} r_i \left(2.11 \times 10^{-5} \left(\frac{T}{T_0} \right)^{1.94} \left(\frac{p_0}{p} \right) \right)^{-1} \quad (3.41)$$

for $\alpha_d = 0.5$ and the mean of the magnitude of the thermal velocity v_{th} . Thus when considering ice crystal radii $r_i \gg r_{i,0}$ the kinetic approach can be reformulated by performing the simplification Eq. (3.40). Subsequently $S_i = (q_v - q_{v,si})/q_{v,si} + 1$ and $n_{sat} = e_{si}/(k_b T)$ are inserted into Eq. (3.33) leading to

$$\frac{dr_i}{dt} = \frac{m_w \alpha_d v_{th}}{\rho_i} \frac{4D_v}{4} \frac{e_{si}}{\alpha_d v_{th} r_i k_b T} \frac{(q_v - q_{v,si})}{q_{v,si}} \quad (3.42)$$

$$= \frac{m_w D_v}{\rho_i r_i} \frac{e_{si}}{k_b T} \frac{(q_v - q_{v,si})}{q_{v,si}}. \quad (3.43)$$

When substituting $e_{si} = R_v/R_a p q_{v,si}$, the Boltzmann constant $k_b = R_a/N_a$ and the mass of a water molecule $m_w = M_w/N_a$ with N_a being the Avogadro constant

$$\frac{dr_i}{dt} = \frac{D_v \rho_a}{\rho_i r_i} (q_v - q_{v,si}) \quad (3.44)$$

is obtained which yields the thermodynamic equation Eq. (3.35) for spherical particles. Thus for homogeneously frozen ice crystals having small ice particle sizes comparable to the mean free path of air molecules it is advisable to use the kinetic equation. The assumption Eq. (3.40) for the thermodynamic formulation holds for the larger heterogeneously nucleated ice crystal radii. In the following, the thermodynamic approach coupled with the Howell factor as described by Eq. (3.38) is applied to heterogeneous hexagonal ice crystal plates.

In question is to what extent the kinetic and thermodynamic formulation and ice crystal habit, i.e. spherical or hexagonal plate, influence the ice crystal growth. In Fig. 3.6 the time evolution of ice crystal radii for the different depositional growth approaches is depicted in dependence of ambient atmospheric conditions favouring homogeneous (Fig. 3.6a) or heterogeneous (Fig. 3.6b) nucleation. Hereby the choice of α_d for the kinetic formulation KL02 is emphasised. The spherical and hexagonal plate based on KS98 and the Howell formulation are considered for the thermodynamic approaches, respectively. For this plot the parcel model time step is set to $\Delta t = 1$ s and the air parcel is at rest, i.e. with no updraft, where only the initial setting distinguishes the nucleation scenarios. To choose a realistic scenario for the homogeneous freezing, the nucleation event is triggered according to Eq. (3.8). The nucleation

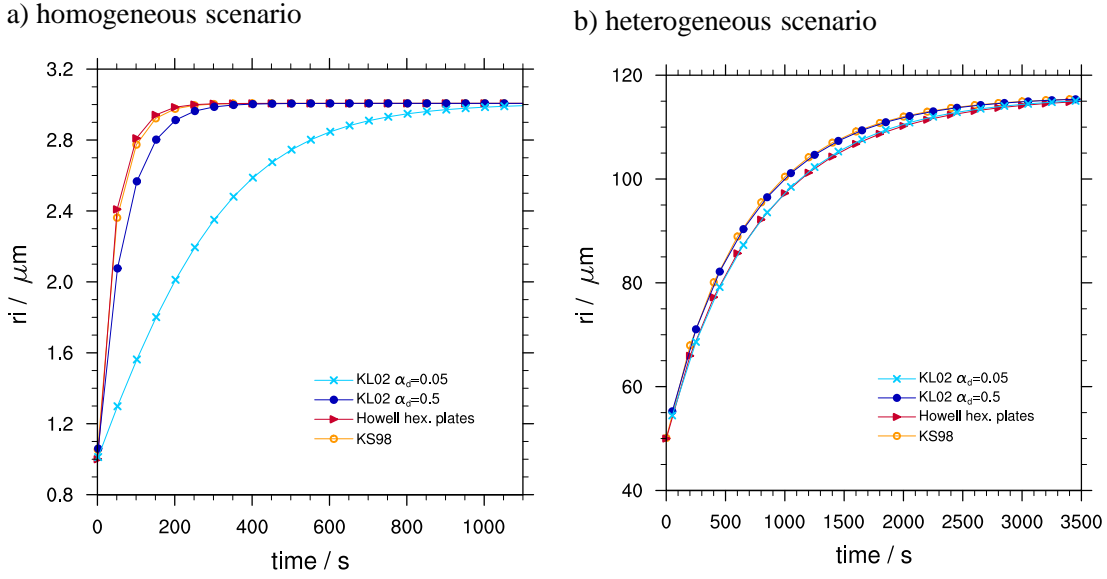


Figure 3.6: The change in ice crystal radii over time for the homogeneous a) and heterogeneous b) scenario for the kinetic and thermodynamic depositional growth rates is depicted. For the homogeneous nucleation, the initial ice crystal radius is $r_{i,0} = 1 \mu\text{m}$, the ice crystal number density is set to $n_i = 10 \text{cm}^{-3}$, and the temperature is $T = 200 \text{K}$. In the heterogeneous nucleation scenario, the initial ice crystal radius is $r_{i,0} = 50 \mu\text{m}$, the constant ice crystal number density is $n_i = 10 \text{dm}^{-3}$, and the temperature is set to $T = 240 \text{K}$. The pressure is $p = 240 \text{hPa}$ for both scenarios. The dark and light blue lines show the influence of the deposition coefficient on the kinetic depositional growth rate. The ice crystal radii resulting from thermodynamic depositional growth rate considering spherical ice particles and hexagonal plates are shown in orange and red, respectively.

threshold for heterogeneous is not as simple and varies for different ice nuclei species. Thus for heterogeneous freezing conditions the simplified freezing threshold

$$S_{w,\text{cr}} = \left(\frac{T}{T_0} \right)^{\frac{M_w L_m^{ef}}{RT}} \quad (3.45)$$

is applied based on Khvorostyanov and Curry (2004) where L_m^{ef} is the effective latent heat of melting in cal g^{-1} for which the approximation given in Khvorostyanov and Curry (2009) is used. $L_m^{ef} = c_{L0} + c_{L1}T_c + c_{L2}T_c^2 + c_{L4}T_c^4$ with T_c in $^\circ\text{C}$ and the dimensionless coefficients $c_{L0} = 79.7$, $c_{L1} = 0.333$, $c_{L2} = -2.5 \times 10^{-3}$ and $c_{L4} = 0.8 \times 10^{-7}$. The critical ice saturation ratio for heterogeneous nucleation then results from $S_{i,\text{cr}} = S_{w,\text{cr}} e_{sw}/e_{si}$.

First, the evolution of an ice crystal with an initial radius of $r_{i,0} = 1 \mu\text{m}$ resembling a homogeneous nucleated ice crystal size as shown in Fig. 3.6a is discussed. As diffusional growth occurs after the nucleation event is triggered, the initial value for ice supersaturation for homogeneous freezing is $S_{i,\text{cr}} = 1.58$ resulting from Eq. (3.8) for $T = 200 \text{K}$. The constant ice crystal number density $n_i = 10 \text{cm}^{-3}$ is prone to occur in gravity wave scale updrafts of $w \approx 10 \text{cm s}^{-1}$. Noticeable is that depositional growth by use of the thermodynamic approach depletes the ice supersaturation quickly causing the asymptotic ice crystal radius $r_i = 3 \mu\text{m}$ to be obtained at $S_i = 1$ within 250 s. In accordance with Harrington et al. (2009) a vast difference is noticeable

when changing the deposition coefficient from $\alpha_d = 0.5$ (Spichtinger and Gierens, 2009a) to $\alpha_d = 0.05$ (Stevens, 2011). In Fukuta and Walter (1970) it is also commented that the kinetic growth approach resembles the Maxwellian equation when setting the deposition coefficient to one. This is because of the lower efficiency of diffusional growth with a lower deposition coefficient causing ice supersaturation to reach higher values due to the slow depletion.

For the heterogeneous freezing scenario the critical ice saturation ratio resulting from Eq. (3.45) yields $S_{i,cr} = 1.28$ for $T = 240$ K. The initial ice crystal number density $n_i = 10 \text{ dm}^{-3}$ with the radius growing from $r_{i,0} = 50 \mu\text{m}$ to $r_i = 115 \mu\text{m}$ in 3500 s. As can be seen in Fig. 3.6b, there are no essential differences between the kinetic, the thermodynamic, the spherical or the hexagonal formulation.

Essentially, the kinetic formulation for diffusional growth shows a higher sensitivity towards the efficiency of the ice supersaturation depletion. While the larger heterogeneous particles accumulate more mass, the radius of the smaller homogeneous ice grows faster in comparison. This also justifies the monodisperse assumption made for Eq. (3.32). These differences for the depositional growth motivates a coupled approach to model the competition between heterogeneous and homogeneous formed ice crystals for the available water vapour in an ice supersaturated environment. The coupled approach is pursued and investigated in Sec. 3.3.2.

3.3.2 Depositional Growth Timescale

The goal is to achieve a physical description for ice supersaturation and consequently for depositional growth, as it plays an important role in its depletion. The competition for existing water vapour of the ice crystals developed by either homogeneous or heterogeneous freezing determines the ice particle number (DeMott et al., 1997). The competition highly depends on the timescale of diffusional growth for either cloud ice mode. The deposition timescale τ_{dep} was schematically depicted in Fig. 3.1 and will be analysed subsequently.

The ice microphysics scheme in the NWP models of the DWD includes a limitation for the deposition rate where the minimum deposition rate is $(q_v - q_{v,si})/\Delta t$ in order to prevent more water vapour to be depleted than available after the depositional growth rate has been calculated. The necessity of this limitation motivates a more physical handling of the depositional growth rate. Also a bulk ice treatment results in higher cloud ice mixing ratio, as a one mode scheme uses the sum of nucleated cloud ice causing a quicker subsequent crystal growth. Thus it is desirable to distinguish the ice modes and to treat the depositional growth rates separately. A relaxation approach of the supersaturation towards an equilibrium state was already considered in Korolev and Mazin (2003), Kärcher and Burkhardt (2008) as well as Wang and Penner (2010). However, the phase relaxation approach proposed in Morrison et al. (2005) for high resolution cloud models additionally includes the interaction of all hydrometeor species. This approach is adapted to the two-mode two-moment ice nucleation parcel scheme where the number density $n_{i,x}$ and cloud ice $q_{i,x}$ are treated separately for $x = hom, het$ respectively. The

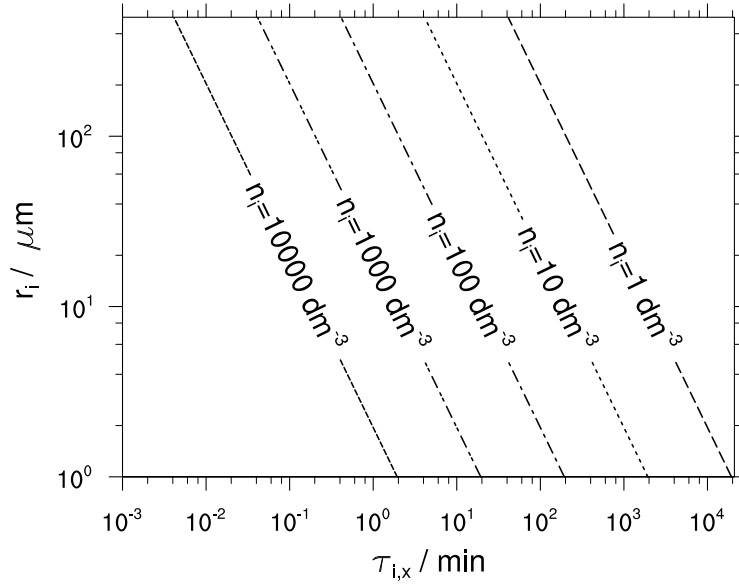


Figure 3.7: The plots show the dependency of the depositional freezing timescales on the mean ice crystal radius and number density for $T = 240$ K and $p = 220$ hPa.

change for the water vapour mixing ratio yields

$$\left. \frac{dq_{v,x}}{dt} \right|_{\text{dep}} = -\frac{\chi(q_v - q_{v,si})}{\tau_{i,x} \Delta t} \times \left[1 - \exp\left(\frac{-\Delta t}{\chi}\right) \right] \quad (3.46)$$

corresponding to the deposition rate for cloud ice τ_{dep} which will be distinguished between for the two ice modes $\tau_{i,\text{hom}}$ and $\tau_{i,\text{het}}$. The general deposition relaxation time χ results from

$$\chi = [(\tau_{i,\text{hom}}^{-1} + \tau_{i,\text{het}}^{-1})]^{-1} \quad (3.47)$$

with the timescales being defined as

$$\tau_{i,x}^{-1} = \left. \frac{dq_v}{dt} (q_v - q_{v,si})^{-1} \right|_x. \quad (3.48)$$

Due to the dependency of q_v on n_i and r_i as seen in Eq. (3.32), the timescales for different mean ice crystal radii and number densities are investigated. The timescale indicates the ability of the air parcel to absorb vapour and the phase transition of vapour to ice. In this section only the depositional timescale for cloud ice is accounted for whereas later simulations include the further interaction of depositional growth of snow (see Eq. (4.28) in Sec. 4.2).

In figure Fig. 3.7 the different timescales for the thermodynamic Howell equation (Howell, 1948) with hexagonal ice crystal shapes are depicted for $T = 240$ K. The analogous change in ice crystal radius is depicted in Fig. 3.6b. Values for the timescales vary between $\tau_{i,x} = 0.24$ s for $r_i = 500 \mu\text{m}$ and $n_i = 10^4 \text{dm}^{-3}$ and longer relaxation times of $\tau_{i,x} = 322$ h for $r_i = 1 \mu\text{m}$ and $n_i = 1 \text{dm}^{-3}$. This shows how larger ice crystal radii and higher number densities reduce the depositional growth timespan. Ice crystal phase relaxation timescales are also noted in Table A1 from Khvorostyanov and Sassen (1998b) based on the thermodynamic approach with spherical

particles, i.e. $\tau_{\text{dep}} = (4\pi D_v n_i r_i)^{-1}$. A comparison shows that $\tau_{i,x}$ shown in Fig. 3.7 is about $\approx 70\%$ smaller than the timescales from Khvorostyanov and Sassen (1998b). This discrepancy is based on differing approximations of the diffusion coefficient D_v of water vapour in dry air. The formulation used in the parcel model was proposed by Pruppacher and Klett (1997) and is temperature and pressure dependent and results in much higher D_v values for low atmospheric pressures than only temperature-related descriptions assuming sea level pressure.

Including the relaxation timescales into the depositional growth cloud ice scheme leads to a more physical approach and more realistic ice supersaturation values. The connection of the relaxation timescale to the quasi-stationary ice supersaturation state is approximated by Khvorostyanov and Sassen (1998b) with

$$(S_i - 1)|_{\text{eq}} = 1.1 \times 10^{-3} w \tau_{\text{dep}} \text{ in } \%. \quad (3.49)$$

The equilibrium value thus results from the vertical updraft w in m s^{-1} and crystal phase relaxation timescale in s . This shows that intermediate values $n_i = 100 \text{ dm}^{-3}$ and $r_i = 100 \mu\text{m}$ mostly found at the top of cirrostratus (DeMott et al., 1994) have $\tau_{i,x} = 121 \text{ s}$ and $(S_i - 1)|_{\text{eq}} = 1.33\%$ for $w = 10 \text{ cm s}^{-1}$. This indicates that no subsequent ice formation through homogeneous nucleation would take place and heterogeneous nucleation is dominant in such a regime (Khvorostyanov and Sassen, 1998b).

Not only the relaxation timescale approach but also the application of the two ice modes alters the depositional growth. The new relaxation timescale approach is coupled to the improved cloud ice scheme. This presents a more physical handling of the water vapour available for this process. Also the possibility of competition for available water vapour between the ice modes and potentially snow is given. In the DWD models this was neglected so far and the diffusional growth for the ice phases was calculated with the Euler forward scheme independent of each other with a saturation limiter ensuring that not more water vapour is depleted than available.

3.4 Ice Nuclei Budget Variable for Heterogeneous Nucleation

Ice nuclei are unequally distributed in the upper atmosphere. Yet, in the heterogeneous nucleation scheme by PDA08 a constant concentration of the three aerosol species is assumed. A more sophisticated way for representing ice nuclei in the cloud ice scheme, would be to use a coupled prognostic aerosol model, such as the COSMO-ART (ART stands for Aerosol and Reactive Trace gases) (Vogel et al., 2009). Such a coupling would be numerically too expensive for operational use at this time. However, the constant amount of available ice nuclei based on PDA08 is not realistic and could potentially lead to an overestimation of heterogeneously nucleated ice crystals. To prohibit such an overestimation of nucleated ice crystals due to the amount of predetermined IN a tracking variable for activated IN is introduced. Motivated by this, a tracer variable $n_{i,\text{nuc}}$ is introduced .

The predefined aerosol number density from PDA08 $n_{\text{IN,PDA08}}$ serves as an initial value and remains constant over all time steps. These are reduced by previously nucleated ice nuclei

$n_{i,\text{nuc}}$. As only the dynamics of an air parcel are considered in this chapter the number density of available ice nuclei at a given time step n_{IN} is simply given by

$$n_{\text{IN}} = n_{\text{IN,PDA08}} - n_{i,\text{nuc}}. \quad (3.50)$$

The ice nuclei budget variable $n_{i,\text{nuc}}$ from Eq. (3.50) limits newly nucleated heterogeneous ice because already activated IN are taken into account in every time step. A similar approach was taken by Cohard and Pinty (2000) for cloud condensation nuclei (CCN). This simplified approach to account for spatial variability of ice nuclei counteracts the same amount of unactivated/background IN to be available, which would be advantageous for heterogeneous nucleation. A more detailed discussion of this simple IN tracking approach will be given in Sec. 4.2. The prognostic equation for the activated ice nuclei concentration $N_{i,\text{nuc}}$ is given in Eq. (4.27).

3.5 Sedimentation

In the operational DWD NWP models ice crystals are considered as non-precipitating, i.e. the process of sedimentation is neglected. Yet its importance is emphasised in the studies of e.g., Spichtinger and Gierens (2009a) and Spichtinger and Cziczo (2010). It is stated that the high ice supersaturation found in cirrus clouds are a potential feedback of sedimentation as the ice crystals fall out prior to ice supersaturation depletion. The impact of the ice crystal terminal velocities on the build up and the decay of cirrus clouds is also stressed by Heymsfield and Iaquinta (2000) while Jensen et al. (2011) highlight its limiting effect due to radiative-dynamic interactions. The implementation of cloud ice sedimentation in the ECMWF global model and its effect on radiation is also discussed by Jakob (2002). Therefore it is essential to include this process in the following studies.

Typical ice fallout formulations are a function of the specific ice content (Jakob, 2002) or of temperature and pressure (Heymsfield and Iaquinta, 2000). Alternatively, the mass-dimension $m - D$ and area-dimension $A - D$ relations are used,

$$m = \alpha D^\beta \quad \text{and} \quad A = \gamma D^\sigma \quad (3.51)$$

where D is the maximum dimension, α and β the mass-size and γ and σ the area-size relation exponents depending on the geometry.

A physically based power-law like representation for the relation between the Reynolds number Re and the Best number X is given by Mitchell (1996) while Mitchell and Heymsfield (2005) reformulated this in terms of $m - D$ and $A - D$ parameters. A continuous formulation over the entire size range of liquid and crystalline particles is presented by Khvorostyanov and Curry (2005, KC05 hereafter). Additional corrections for the transition of laminar to turbulent flow and change in air density are accounted for. This resulting terminal fall velocity as a function

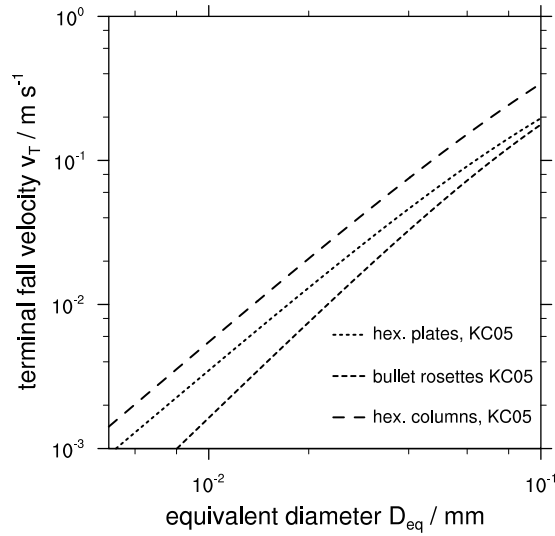


Figure 3.8: The plot depicts the terminal velocities for different ice crystal shapes based on Khvorostyanov and Curry (2005) with the reference air density $\rho_a = 1.225 \text{ kg m}^{-3}$.

of D as stated in KC05 is

$$v_{i,T} = A_v D^{B_v}, \quad (3.52)$$

$$\text{with } A_v = a_{Re} \rho_a^{b_{Re}-1} \eta^{1-2b_{Re}} \left(\frac{2\alpha g}{\gamma} \right)^{b_{Re}}, \quad (3.53)$$

$$\text{and } B_v = b_{Re}(\beta - \sigma + 2) - 1. \quad (3.54)$$

The continuous functions a_{Re} and b_{Re} are determined in terms of the relation $Re(X) = a_{Re} X^{b_{Re}}$ and are defined in Eq.(2.7)-(2.8) in KC05 and η is the dynamic viscosity. The equivalent diameter described by Eq. (3.51) is used with the exponents for small hexagonal plates $\alpha = 0.5870086$, $\beta = 2.45$, $\gamma = 0.120285$ and $\sigma = 1.85$ (Mitchell, 1996). Terminal velocities for different geometries, namely hexagonal plates, bullet rosettes and hexagonal columns and their equivalent diameters are depicted in Fig. 3.8 using the reference air density $\rho_a = 1.225 \text{ kg m}^{-3}$. For consistency hexagonal plates are assumed hereafter since this geometry is already chosen for the depositional growth.

Larger ice crystals have a greater acceleration with height than smaller particles ($r_i \approx 30 - 40 \mu\text{m}$) because of the lower air density. Thus it is important to choose an accurate description which accounts for this size discrepancy as is done in KC05. Recent laboratory and field studies conducted by Heymsfield and Westbrook (2010) show that the terminal velocities were previously overestimated by the latter parameterisation for particles smaller than $100 \mu\text{m}$, especially when considering open geometries. Considering hexagonal plates reduces this shortcoming. As shown in Heymsfield and Westbrook (2010), this method for calculating the terminal velocity for Reynolds numbers $Re \approx 100$ yields almost identical results to Mitchell (1996) and Mitchell and Heymsfield (2005).

In summary, sedimentation serves as an important sink for cloud ice. So far this process is neglected in the NWP models at DWD but is now implemented in the new cloud ice scheme by use of the KC05 parameterisation for the terminal velocity.

Chapter 4

Application in Numerical Weather Prediction Models

In the previous chapter, the theoretical background of the new ice cloud scheme was explained and sensitivities studied by using a parcel model. In the following, the microphysical scheme implemented in the high resolution regional model COSMO and the global model GME will be introduced. As the NWP model physics and dynamics are more complex than the adiabatically lifted air parcel, the key equations based on the methodics introduced in Chap. 3 are extended.

It needs to be stressed that the same ice microphysics scheme which includes the implementation of the improvements is used for all the model setups. Changed parameters for investigating sensitivities for the different scales are explicitly stated. Of special interest are the additional source terms for the vertical velocity in order to account for sub-grid scale updrafts. These differ for the COSMO model, where the turbulent kinetic energy (TKE) will be used (Sec. 4.3.1), while the sub-grid scale orography (SSO) scheme is applied for local vertical velocity enhancements in the GME (Sec. 4.3.2).

In this chapter the emphasis lies on the application of the previously described cloud ice scheme in the NWP model chain of the DWD. First, the model microphysics as operationally implemented in the DWD models is presented. Subsequently the performed modifications will be explained including the superposed derived vertical velocities from the TKE and SSO scheme. Second, COSMO model simulations will be performed. These consist of an idealised and a real case simulation. The idealised orographic flow simulation will be compared to measurements from the INCA campaign. Third, the validity of the refined COSMO-DE case study will be evaluated by use of Meteosat Second Generation satellite data. Attention will be particularly paid to the sensitivity of the cloud ice scheme to the vertical velocity. This includes an approach to derive sub-grid scale variability for later use in the global model.

4.1 Model Microphysics

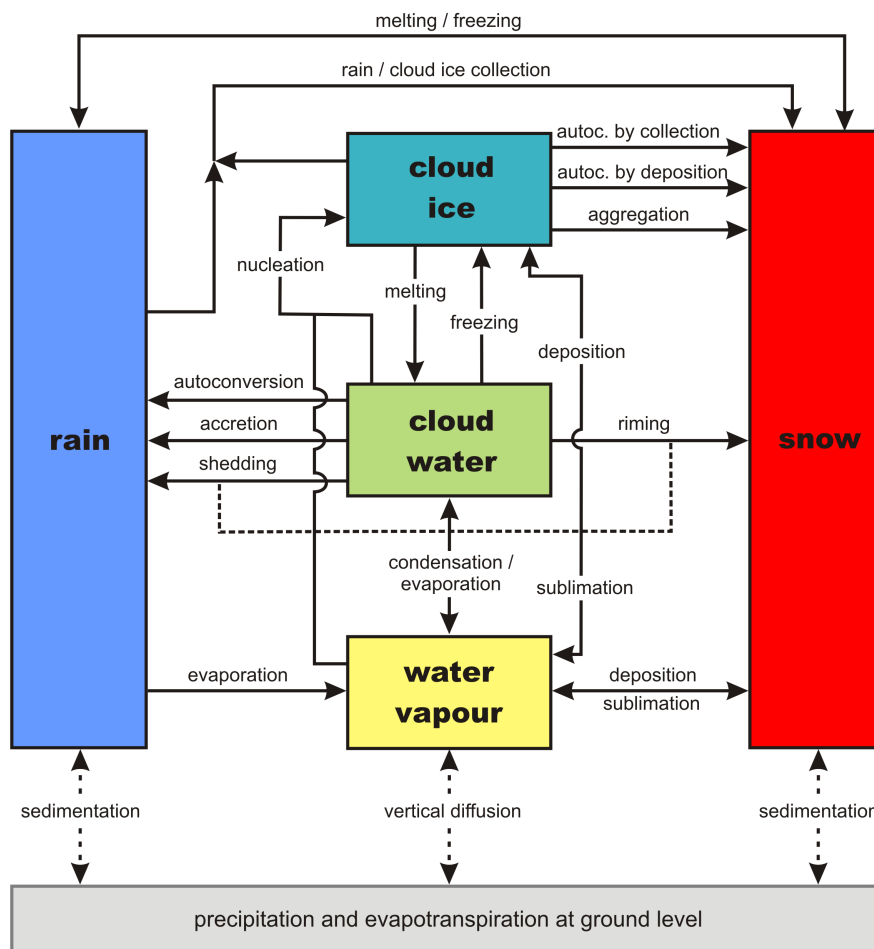


Figure 4.1: Illustration of various microphysical processes in the COSMO/GME (Schulz and Schättler, 2010).

Following the COSMO model documentation by Doms et al. (2007) the cloud ice relevant processes in the COSMO model and GME concerning cloud ice will be covered. The bulk-water continuity model is run in prognostic mode for the two precipitating categories rain and snow with their mass fractions q_r and q_s and the non-precipitating quantities water vapour, cloud water and cloud ice with mass fractions q_v , q_c and q_i , respectively. A schematic overview for the different microphysical processes is given in Fig. 4.1. The generic budget equation in advection form is

$$\frac{\partial q_{l,f}}{\partial t} + v \cdot \nabla q_{l,f} - \frac{1}{\rho_a} \frac{\partial P_{l,f}}{\partial z} = S_{l,f} - \frac{1}{\rho_a} \nabla \cdot F_{l,f} \quad (4.1)$$

where l and f stand for liquid and solid water substances, and $S_{l,f}$ for the cloud microphysical sources and sinks per unit mass of moist air. $F_{l,f}$ denotes the turbulent fluxes and $P_{l,f}$ is defined by

$$P_{l,f} = \rho_a q_{l,f} v_{l,f}^T \quad (4.2)$$

and represents the precipitation or sedimentation fluxes dependent on the mean terminal fall velocities of the particles $v_{i,f}^T$. Thus Eq. (4.1) holds for the prognostic precipitation categories q_r and q_s . The mass fractions q_v , q_c and q_i are considered to be non-precipitating thus having a negligible fall velocity in the operational model setup. The sedimentation fluxes P_v , P_c and P_i are therefore neglected at this stage and Eq. (4.1) simplifies to

$$\frac{\partial q_{v,c,i}}{\partial t} + v \cdot \nabla q_{v,c,i} = S_{v,c,i} - \frac{1}{\rho_a} \nabla \cdot F_{v,c,i}. \quad (4.3)$$

On the other hand, turbulent fluxes are neglected for q_r and q_s since the precipitating fluxes are much larger. The conservation equations for the two-category ice scheme for water vapour, cloud water, cloud ice, rain and snow as stated in Doms et al. (2007) read:

$$\frac{\partial T}{\partial t} = A_T + \frac{L_v}{c_{pd}}(S_c + S_r) + \frac{L_s}{c_{pd}}(S_i + S_s) \quad (4.4)$$

$$\frac{\partial q_v}{\partial t} = A_{q_v} + S_v \quad (4.5)$$

$$\frac{\partial q_c}{\partial t} = A_{q_c} + S_c \quad (4.6)$$

$$\frac{\partial q_i}{\partial t} = A_{q_i} + S_i \quad (4.7)$$

$$\frac{\partial q_r}{\partial t} = A_{q_r} + \frac{1}{\rho_a} \frac{\partial}{\partial z} (\rho_a q_r v_r^T) + S_r \quad (4.8)$$

$$\frac{\partial q_s}{\partial t} = A_{q_s} + \frac{1}{\rho_a} \frac{\partial}{\partial z} (\rho_a q_s v_s^T) + S_s. \quad (4.9)$$

The advection terms A also summarise other processes, e.g. turbulent diffusion for q_v , q_c and q_i . As cloud ice is of primary interest in this work, the transfer rates for this category are given explicitly:

$$S_i = S_{nuc} + S_{c,frz} + S_{i,dep} - S_{i,melt} - S_{i,au} - S_{aud} - S_{agg} - S_{i,cri} \quad (4.10)$$

with the explanation for the terms in Tab. 4.1. A source term is obtained by integrating the rate of mass growth $\dot{m}(D)$ of an individual particle with diameter D over the full spectral distribution given by an empirical particle size distribution $f(D)$:

$$S = \frac{1}{\rho_a} \int_0^\infty \dot{m}(D) f(D) dD. \quad (4.11)$$

In the case of cloud ice a monodisperse distribution is assumed.

The description of the source terms for the nucleation processes S_{nuc} , $S_{c,frz}$, depositional growth $S_{i,dep}$ and autoconversion S_{aud} are changed in the context of this study and are described at first in their original form. In the operational scheme, the heterogeneous nucleation rate is given by

$$S_{nuc} = \begin{cases} \frac{1}{\rho_a} \frac{m_{i,0}}{\Delta T} n_i(T), & \text{if } T < T_d, q_i = 0 \text{ and } q_v \geq q_{v,si} \\ \frac{1}{\rho_a} \frac{m_{i,0}}{\Delta T} n_i(T), & \text{if } T_d \geq T \geq T_{nuc}, q_i = 0 \text{ and } q_v \geq q_{v,sw} \\ 0, & \text{else} \end{cases} \quad (4.12)$$

where $T_{nuc} = 267.15$ K serves as the nucleation threshold and $T_d = 248.15$ K distinguishes between cloud ice formation at water saturation $q_{v,sw}$ and depositional freezing for ice supersaturation. The assumed initial mass of cloud ice crystals is $m_{i,0} = 10^{-12}$ kg and the number of

S_{nuc}	heterogeneous nucleation of cloud ice
$S_{c,frz}$	nucleation of cloud ice due to homogeneous freezing of cloud water
$S_{i,dep}$	deposition growth and sublimation of cloud ice
$S_{i,melt}$	melting of cloud ice to form cloud water
$S_{i,au}$	autoconversion of cloud ice to form snow due to aggregation
S_{aud}	autoconversion of cloud ice to form snow due to deposition
S_{agg}	collection of cloud ice by snow (aggregation)
$S_{i,cri}$	collection of ice by rain to form snow.

Table 4.1: Explanations for the transfer rates for cloud ice.

ice particles per unit volume of air n_i is described as a function of T . The calculation for the ice nuclei which are activated below the freezing point $n_{IN,a}$ is based on the modified Fletcher formula Eq. (3.29) in Sec. 3.2.2.

If the temperature falls below the threshold of $T_{frz} = 236.15$ and supercooled cloud droplets exist, they are instantly frozen by homogeneous freezing.

$$S_{c,frz} = \begin{cases} q_c/\Delta t, & \text{if } T < T_{frz} \text{ and } q_c > 0 \\ 0, & \text{else} \end{cases} \quad (4.13)$$

The depositional growth equations were thoroughly discussed in Sec. 3.3. In the models, it is stated analogue to Eq. (3.38) for hexagonal plates

$$S_{i,dep} = c_{i,dep} n_i m_i^{1/3} (q_v - q_{v,si}) \quad (4.14)$$

with $c_{i,dep} = 4D_v a_{i,m}^{-1/3} / (1 + H_i) = 1.3 \cdot 10^{-5}$ (SI-units) assuming that the Howell factor H_i changes relatively slowly for differing temperatures and pressures. The depositional growth and sublimation are restricted to water saturation, and the Euler forward scheme is used for calculation.

$$S_{i,dep} = \begin{cases} \min(q_i/\Delta t, (q_v - q_{v,si})/\Delta t), & \text{if } q_v > q_{v,si} \\ \max(-q_i/\Delta t, (q_v - q_{v,si})/\Delta t), & \text{if } q_v < q_{v,si}. \end{cases} \quad (4.15)$$

In the single moment cloud ice scheme a monodisperse size distribution is assumed with the mean cloud ice crystal mass being

$$m_i = \min(\rho_a q_i n_i^{-1}, m_{i,max}), \quad \text{where } m_{i,max} = 10^{-9} \text{ kg} \quad (4.16)$$

where the $m_{i,max}$ was introduced to limit the ice crystal diameter to the maximum of $D_{i,max} = 200 \mu\text{m}$.

The autoconversion rate S_{aud} of cloud ice for snow formation due to depositional growth is given by

$$S_{aud} = \frac{S_{i,dep}}{1.5(m_{s,0}/m_i)^{2/3} - 1} \quad (4.17)$$

where $m_{s,0} = 3 \cdot 10^{-9} \text{kg}$ is the initial mass for snow crystals equivalent to $D_{s,0} = 300 \mu\text{m}$. This process can reduce the ice crystal depositional growth rate by as much as 65% for $m_i = m_{i,\text{max}}$.

Further terms needed in Eq. (4.10) which remain unchanged in this study are $S_{i,\text{melt}}$, $S_{i,\text{au}}$, S_{agg} and $S_{i,\text{cri}}$. Instantaneous melting occurs in case of the temperature rising above T_0

$$S_{i,\text{melt}} = \begin{cases} q_i/\Delta t, & \text{if } T > T_0 \text{ and } q_i > 0 \\ 0, & \text{else} \end{cases} \quad (4.18)$$

The collection of cloud ice by rain serves as a sink for q_i and source for snow. The parameterisation of the transfer rate describing this process is

$$S_{i,\text{cri}} = \frac{\pi}{4} E_{i,r} q_i \int_0^\infty D^2 v_{T,r}(D) f_r(D) dD. \quad (4.19)$$

Evaluation of the integral in Eq. (4.19) yields

$$S_{i,\text{cri}} = c_{i,\text{cri}} q_i (\rho_a q_r)^{7/8} \quad (4.20)$$

with the rate coefficient

$$c_{i,\text{cri}} = \frac{15}{32} \sqrt{\pi} \frac{E_{i,r}}{\rho_w} v_{r,0} A_r^{1/8}. \quad (4.21)$$

The collection efficiency $E_{i,r}$ of small ice particles being collected by rain is set to $E_{i,r} = 0.8$ and $v_{r,0} = 130 \text{m}^{1/3} \text{s}^{-1}$ yielding $c_{i,\text{cri}} = 1.72$ in SI-units.

$S_{i,\text{agg}}$ is the transfer rate due to aggregation of snow and cloud ice and reads

$$S_{i,\text{agg}} = c_{\text{agg}} q_i (\rho_a q_s)^{13/12} \quad (4.22)$$

with the mean collection rate coefficient $c_{\text{agg}} = 25.8$ (SI-units) for snow crystals collecting ice particles.

The parameterisation for the autoconversion of cloud ice to snow due to cloud ice crystal aggregation $S_{i,\text{au}}$ is simply set to

$$S_{i,\text{au}} = \max(c_{i,\text{au}}(q_i - q_{i,0}), 0) \quad (4.23)$$

with the coefficient $c_{i,\text{au}} = 10^{-3} \text{s}^{-1}$ for cloud ice and the autoconversion threshold is set to $q_{i,0} = 0$.

This describes the status quo of the cloud ice sources in the current operational scheme of the NWP models at the DWD. As mentioned beforehand, particular attention is set to the terms S_{nuc} , $S_{c,\text{frz}}$, $S_{i,\text{dep}}$ and S_{aud} , the modifications of which are specified in Sec. 4.2.

4.2 Applied Methodics

Previously the theoretical approaches were described and tested in a parcel model environment (see Sec. 3). For the NWP setup a few adaptations of the formulations are required. In this

section the two-moment two-mode model equations for the cloud ice scheme are presented. In this context the previously introduced equations of the depositional growth timescale (see Sec. 3.3.2), tracking variable (see Sec. 3.4) and sedimentation (Sec. 3.5) are adapted for the COSMO/GME.

For a better comprehension of the impact of the different nucleation schemes a two-moment two-mode cloud ice nucleation scheme is implemented. It consists of the mass fraction of cloud ice in the air $q_{i,x}$ and the ice crystal number fraction $N_{i,x}$ with $x = hom, het$ respectively. In the microphysical scheme the sources for these prognostic variables are

$$S(q_{i,x}) = (S_{nuc} + S_{c,frz} + S_{i,dep} + S_{i,melt} - S_{i,au} - S_{agg} - S_{i,cri})|_x \quad (4.24)$$

$$S(N_{i,x}) = \left(S_{nuc} + \frac{S_{c,frz}}{m_c} - \frac{S_{i,melt} + S_{i,au} + S_{agg} + S_{i,cri}}{m_i} \right) |_x \quad (4.25)$$

where $m_i = q_i/N_i$ denotes the mean ice crystal mass and $m_c = \frac{\pi}{6}\rho_w D_c^3$ the assumed average mass of a cloud droplet with diameter $D_c = 50\mu\text{m}$. The source terms $S_{i,melt}|_x$, $S_{i,au}|_x$, $S_{agg}|_x$ and $S_{i,cri}|_x$ are calculated as described in Sec. 4.1. The term $S_{nuc}|_{hom}$ results from the homogeneous nucleation scheme described in Sec. 3.2.1 while the heterogeneous nucleation rate $S_{nuc}|_{het}$ results from the empirical parameterisation stated in Sec. 3.2.2. The resulting ice crystal number density of the latter scheme is also used as an immersion freezing source rate

$$S_{c,frz}|_{het} = m_c \frac{N_{i,het}(t) - N_{i,het}(t-1)}{\Delta t}. \quad (4.26)$$

The number of heterogeneously nucleated ice crystals is confined by the ice nuclei budget variable described in simple form in Sec. 3.4. The prognostic formulation of the activated ice nuclei concentration $N_{i,nuc}$ includes the advection term. Additionally in this formulation, a mixing time scale τ_{mix} is introduced. The time scale is an estimation about when previously activated ice nuclei are available again for further heterogeneous nucleation. Throughout this study τ_{mix} is set to two hours. The total implemented prognostic form of the number of activated ice nuclei $N_{i,nuc}$ per unit mass is

$$\frac{\partial N_{i,nuc}}{\partial t} + v \cdot \nabla N_{i,nuc} = \frac{\partial N_{i,het}}{\partial t}|_{het} - \frac{N_{i,nuc}}{\tau_{mix}}. \quad (4.27)$$

The IN budget equation Eq. (4.27) provides a prognostic approach to trace previously activated ice nuclei without being numerically too costly.

Ice crystals then grow or sublimate due to diffusional growth. In the model, snow also depends on the water vapour resources for deposition. In the operational scheme limiting ensures that the amount of water vapour depleted does not exceed the available amount. To avoid a restriction and to follow a more physical treatment the phase relaxation approach for high resolution cloud models (Morrison et al., 2005) is applied, which includes the interaction of all hydrometeor species. The relaxation timescale method is adapted to the two-mode two-moment cloud ice nucleation scheme. Droplet and rain phase relaxation times are neglected. Also, the temperature changes due to radiation and the Bergeron-Findeisen that are included in Morrison et al. (2005)

are not accounted for explicitly in the following. The resulting equation for the depositional growth rate for the two-ice mode and snow scheme is

$$S_{i,dep}|_x = -\frac{\chi(q_v - q_{si})}{\tau_{i,x} \Delta t} \left[1 - \exp\left(\frac{-\Delta t}{\chi}\right) \right] \quad (4.28)$$

giving the deposition rate for cloud ice and snow with $x = het, hom, snow$ and χ being the general deposition relaxation time

$$\chi = [(\tau_{i,hom}^{-1} + \tau_{i,het}^{-1} + \tau_{snow}^{-1})]^{-1}. \quad (4.29)$$

The change in the depositional growth equation motivates to neglect the autoconversion term of cloud ice to form snow due to deposition $S_{i,aud}$ because this term reduces the depositional growth rate and thus dismantles cloud ice.

After diffusional growth the cloud ice crystals are subject to sedimentation. To account for cloud ice sedimentation in the present study, the terminal velocity $v_{i,T}$ for hexagonal ice crystals discussed in Sec. 3.5 is introduced into the prognostic equations

$$\frac{\partial q_{i,x}}{\partial t} = A_{q_{i,x}} + \frac{1}{\rho} \frac{\partial}{\partial z} (\rho q_{i,x} v_{i,T}|_x) + S_i|_x, \quad (4.30)$$

$$\frac{\partial N_{i,x}}{\partial t} = A_{N_{i,x}} + \frac{1}{\rho} \frac{\partial}{\partial z} (\rho N_{i,x} v_{i,T}|_x) + S_i|_x, \quad (4.31)$$

where $A_{q_{i,x}}$ and $A_{N_{i,x}}$ represent the advection terms and $S_i|_x$ subsumes the source terms. This results in the full model equations for the COSMO model and GME. A further extension is made in the calculation for the vertical velocity as it differs for both models being described in Sec. 4.3.

4.3 Vertical Velocity Parameterisations

The nucleation process is highly dependent on the vertical velocity, as described in Sec. 3.2. The different horizontal model resolutions of the COSMO model and GME call for a different handling of sub-grid scale fluctuations. In the following the approach from Joos et al. (2008) is adapted to derive additional fluctuations by use of the turbulent kinetic energy and the sub-grid scale orography. The vertical velocity is enhanced by use of the turbulent kinetic energy (*TKE*) in the COSMO model and the GME uses the sub-grid scale orography induced velocity derived from the SSO scheme. An additional resolution-dependent sub-grid scale parameterisation for the vertical velocity in the GME is derived from COSMO model simulations. This sub-grid scale updraft velocity w_{sgs} is described later in Sec. 6.2.3.

4.3.1 Fluctuations Induced by Turbulent Kinetic Energy

The turbulent kinetic energy is treated as a prognostic variable in the COSMO model having the advantage of including further physical effects opposed to the diagnostic treatment as used

in the global model GME. Thus vertical diffusion and TKE production through sub-grid scale thermic circulation can be accounted for in the COSMO model (Baldauf et al., 2010). The TKE scheme therein is based on a hierarchy order 2.5 closure model (classification based on Mellor and Yamada (1974)).

The vertical velocity used in the proposed cloud ice scheme is calculated from the square root of the TKE and a scalable factor. In the climate model ECHAM5 (European Center/Hamburg 5) the relation $w_{TKE} = 0.7\sqrt{TKE}$ based on an isotropic assumption for sub-grid scale fluctuations is applied (Lohmann et al., 1999). Analogue to Joos et al. (2008), this assumption is implemented into the COSMO model. The resulting total vertical velocity for the ice nucleation scheme is $w = w_{COSMO} + w_{TKE}$.

4.3.2 Sub-grid Scale Orography Induced Velocity

The global model GME uses a diagnostic relation for the mean global kinetic energy which does not deliver useful turbulent kinetic energy values for the upper troposphere due to uncertainties within the choice of length scale. The horizontal resolution of the GME used in this study is 30km and leads to the necessity of explicitly parameterizing the local variability in the vertical velocity.

In the GME, the vertical velocity results from the change in pressure ω using the hydrostatic equation

$$w = -\omega/(\rho_a g). \quad (4.32)$$

The vertical velocity is enhanced by adding the term w_{SSO} in order to introduce fluctuations and higher values for the cloud ice microphysical scheme. Hereby w_{SSO} evolves from the sub-grid scale orographic drag parameterisation based on Lott and Miller (1997). The vertical velocity induced by propagating gravity waves is formulated in Joos et al. (2008) as

$$w_{SSO} = kU \min(\delta h, \delta h_{sat}). \quad (4.33)$$

Assuming a mountain with the form $z = h(x) = h_m \sin(kx)$ and the height h_m , a projected horizontal wind speed U and a wave number $k = 2\pi/L$. The length scale of the grid-point region $L(z)$ is given by twice the horizontal width of the mountain seen by the upstream flow

$$L(z) \approx 2 \max(b \cos \Psi, a \sin \Psi) \left(\frac{Z_{blk} - z}{z + \mu} \right)^{1/2}, \quad (4.34)$$

with the depth of the blocked layer Z_{blk} , the standard deviation of the orography μ , the angle between incident flow and orographic principal axis Ψ , and the half mountain width in the cross- and along-ridge a, b , respectively. The mountain parameters a, b are calculated by using the mean slope, standard deviation and anisotropy of the model orography.

Following Joos et al. (2008) the flow is thought to be nearly hydrostatic and the Coriolis force is neglected. The vertical displacement of the flow is described by δh and the change of the

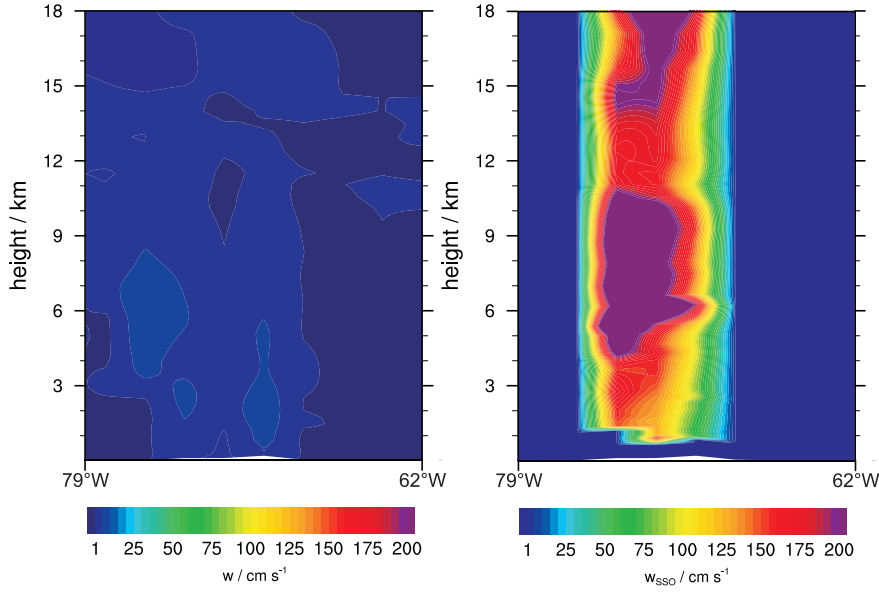


Figure 4.2: The cross section over the Andes from 79°W - 62°W and 53°S for the INCA campaign on the 5th April 2000 at 18:00 UTC over the Andes. The plot shows the increased vertical velocity due to additional forcing from the sub-grid scale. The mean grid vertical velocity is depicted on the left and the right shows the GME velocity with orographic induced enhancement.

amplitude of the gravity waves with height is represented by

$$\delta h^2 = \frac{\rho_h N_h U_h h_m^2}{\rho_a N U} \quad (4.35)$$

with the Brunt-Väisälä frequency N and the horizontal wind speed U at model level. The averaged values between surface and mountain peak are denoted by the subscript h . The minimum Richardson number is

$$R_{i,\min} = R_i \frac{1 - N\delta h/U}{1 + R_i^{1/2} (N\delta h U)^2} \quad (4.36)$$

with $R_i = (N/(dU/dz))^2$ for the background flow. The term δh_{sat} is calculated by use of Eq. (4.36) and is the saturation amplitude corresponding to $R_i = 0.25$, the threshold of instability. This allows to calculate w_{SSO} according to Eq. (4.33).

This parameterised vertical velocity is depicted in Fig. 4.2. Shown is a meridional cut of the INCA campaign flight route over the Andes analogue to Fig. 6 in Joos et al. (2008). For comparison only the positive values are plotted. On the left hand side of Fig. 4.2 the normal model vertical velocity is shown with values about 1 cm s^{-1} . On the right hand side of Fig. 4.2 the sub-grid scale orography induced vertical velocity is depicted which reaches high values of around 200 cm s^{-1} . Capturing these high peaks in the vertical velocity is of importance for the ice nucleation mechanisms when dealing with a global model. The dependency of vertical fluctuations on cirrus formation is highlighted in the next section, Sec. 4.4.

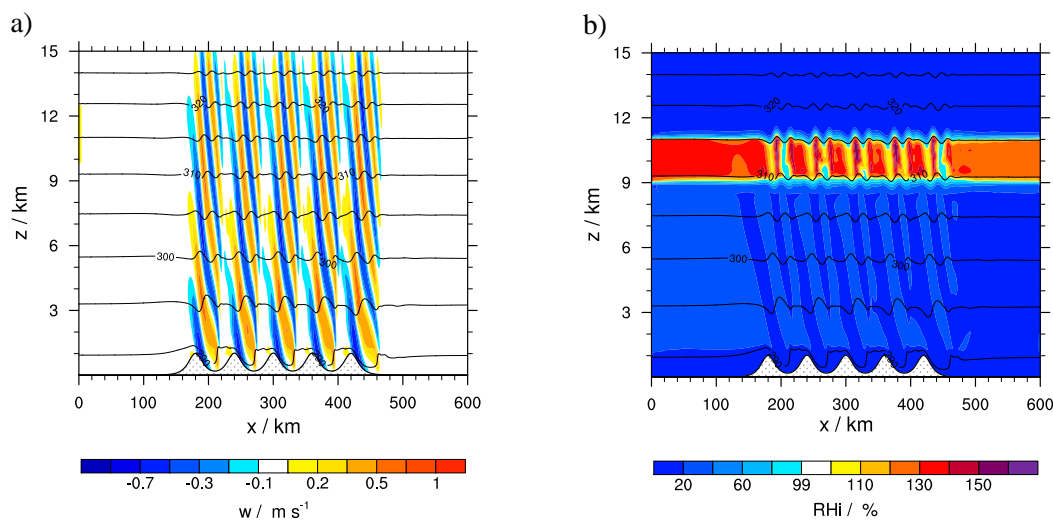


Figure 4.3: Orographic test case with 1 km mountain height, a 2 km deep ice supersaturated layer with $RH_i = 130\%$ after 2h simulation time, and an initial horizontal wind $u_0 = 12 \text{ m s}^{-1}$.

4.4 Idealised COSMO Model Simulations of Orographic Cirrus

In order to test and comprehend the previously described modifications of the cloud ice scheme, they are implemented in the COSMO model environment. Idealised simulations with a horizontal resolution of $\Delta x = 1 \text{ km}$, 99 vertical layers and a time step of $\Delta t = 8 \text{ s}$ are run for 12 hours. The sensitivity of the ice nucleation processes toward the orographic forcing and available ice nuclei is investigated by varying the maximum mountain height h_{max} and a scaling factor for ice nuclei χ_{IN} . The artificial model orography h_{surf} consists of five bell-shaped hills with half-width $a = 20 \text{ km}$ and height h_{max} . The surface topography in x -direction for the number of hills n is given by

$$h_{\text{surf}}(x) = \frac{h_{\text{max}}}{\left(\frac{((x/2-1)-(n-3)3a)^2}{a^2} + 1\right)^2}. \quad (4.37)$$

Together with the initial horizontal wind speed of $u_0 = 12 \text{ m s}^{-1}$ gravity waves are excited. Additionally, a 2 km deep layer between 9-11 km is initialised with the relative humidity with respect to ice of $RH_i = 130\%$. This setup is illustrated in Fig. 4.3 after a simulation time of 2 hours. Depicted are the vertical velocity w (Fig. 4.3a) and RH_i (Fig. 4.3b) along with the isolines for a mountain height of 1 km.

The main factors controlling cirrus cloud properties are the variability in vertical velocity influencing the real and the existence of background aerosols. The topography height influences the intensity of gravity waves: an increase leads to a stronger orographic forcing. To investigate the effect of ice nuclei on the development of cirrus clouds a factor χ_{IN} is introduced as a scaling parameter for the amount of available IN, i.e. for $n_{\text{DM}} = 162 \text{ dm}^{-3}$, $n_{\text{BC}} = 15 \text{ cm}^{-3}$ and $n_{\text{O}} = 1.77 \text{ cm}^{-3}$. Setting this factor to $\chi_{\text{IN}} = 1$ results in the ice nuclei quantity proposed in Phillips et al. (2008). While stronger updrafts trigger homogeneous freezing of liquid aerosols, the quantity of IN in the atmosphere governs the heterogeneous nucleation. Haag and Kärcher

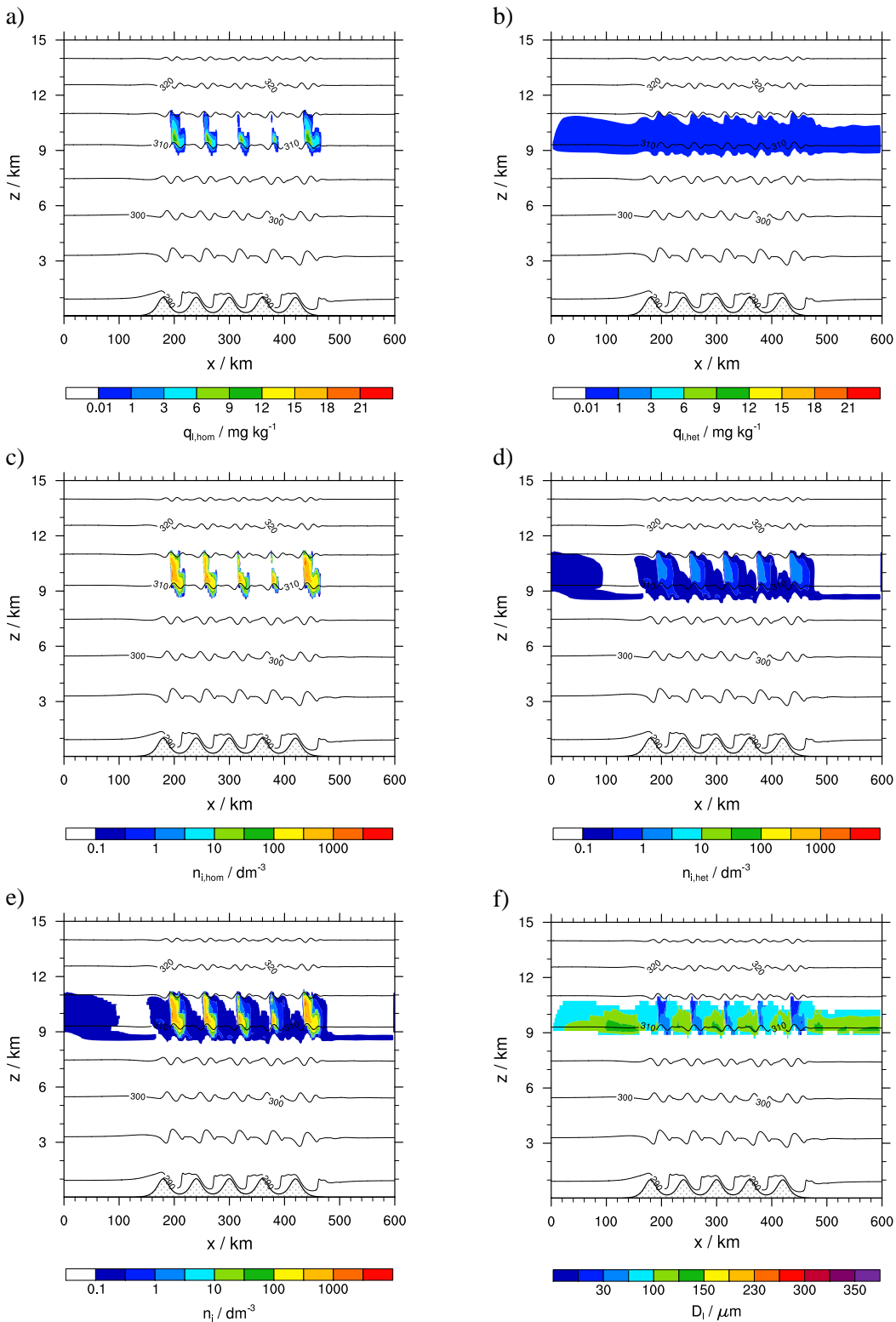


Figure 4.4: The initial conditions for this idealised simulation are $RHi = 130\%$, $h_{\max} = 1 \text{ km}$, $u_0 = 12 \text{ m s}^{-1}$ and $\chi_{\text{IN}} = 0.3$ causing both nucleation regimes to be triggered. Shown are the cloud ice mixing ratio and the cloud ice number density for homogeneous and heterogeneous nucleation in a), b), c) and d), respectively. In e) and f) the entire cloud ice number density and mean diameter is depicted.

(2004) state that some 0.01cm^{-3} IN are a threshold concentration above which the heterogeneous nucleation process becomes dominant and the role of homogeneous nucleation is diminished. Even though this value is strongly dependent on the ambient temperature, the cooling rate and the IN freezing relative humidity need to be further investigated as the controlling factors.

Consequently, the competition of the ice nucleation mechanisms towards the availability of ice nuclei opposed to the effects of the vertical velocity magnitude induced by gravity waves are compared. As an example, the same intermediate setup as in Fig. 4.3 with $\chi_{\text{IN}} = 0.3$ is shown in Fig. 4.4 where both nucleation mechanisms are triggered. Plotted are the heterogeneous and homogeneous mixing ratios $q_{i,\text{hom}}$, $q_{i,\text{het}}$ and number densities $n_{i,\text{hom}}$, $n_{i,\text{het}}$ as well as the total number density n_i and total cloud ice mean diameter D_i . When looking at a regime where the two-modes are active, the different characteristics of the freezing mechanisms become clearly visible. The mean cloud ice mixing ratio $q_{i,\text{het}} = 0.004\text{mgkg}^{-1}$ and number density $n_{i,\text{het}} = 0.03\text{dm}^{-3}$ are one and two magnitudes lower than for homogeneous freezing where the mean values are $q_{i,\text{hom}} = 0.03\text{mgkg}^{-1}$ and $n_{i,\text{hom}} = 3.12\text{dm}^{-3}$. The thicker homogeneously formed cirrus are situated in the regions of strong updraft. This is also noticeable as the cloud ice mean diameter Fig. 4.4f reaches values of $D_i \approx 30\mu\text{m}$ in the regions of strong updraft while maximum values of $D_i \approx 150\mu\text{m}$ are obtained where only IN are available and thus heterogeneous nucleation was triggered. This reduction of the number of ice crystals and subsequent increased effective cloud ice radii is the key effect of IN on cirrus clouds (Haag and Kärcher, 2004).

Ice nuclei in the atmosphere are a necessity for the triggering of heterogeneous freezing. Thus the limitation of available IN by a simplified IN budget has a large impact on cirrus cloud formation. The heterogeneously nucleated ice particles are of greater sizes making them susceptible to sedimentation which alters the cirrus cloud properties. The impact of the tracking of activated IN for a mixing time scale of $\tau_{\text{mix}} = 2\text{h}$ and cloud ice sedimentation are shown exemplarily in Fig. 4.5. The simulation result after 12 hours is plotted when a quasi-stationary state is reached. The mountain height of $h_{\text{max}} = 0.8\text{km}$ and aerosol scaling factor $\chi_{\text{IN}} = 3$ result in a heterogeneous freezing dominated scenario. Fig. 4.5a includes the effect of IN tracking and cloud ice sedimentation in the cloud ice scheme. The corresponding number density of the tracking variable $n_{i,\text{nuc}}$ is plotted in Fig. 4.5b. Not tracking the activated IN means to provide heterogeneous nucleation with a constant amount of IN in every time step. Thus the amount of heterogeneously nucleated particles is higher in Fig. 4.5c, where this is the case, than in Fig. 4.5a. Omitting the IN tracking yields a more stratus like homogeneous cirrus cloud structure apart from the four peaks which amount to $n_{i,\text{het}} \approx 10\text{dm}^{-3}$. Another aspect is the vertical extent of the orographic cirrus cloud being broader in Fig. 4.5a and Fig. 4.5b than in Fig. 4.5d which does not include sedimentation. When the terminal fall velocity of cloud ice crystals is neglected, the cirrus cloud is restricted to the region of the initial ice supersaturation layer. The heterogeneous ice crystal number density in Fig. 4.5d shows the same variability as in Fig. 4.5a due to the limiting tracking variable. Yet in all plots the same overall structure can be seen. The stratiform cirrus results from the high amount of ice supersaturation available.

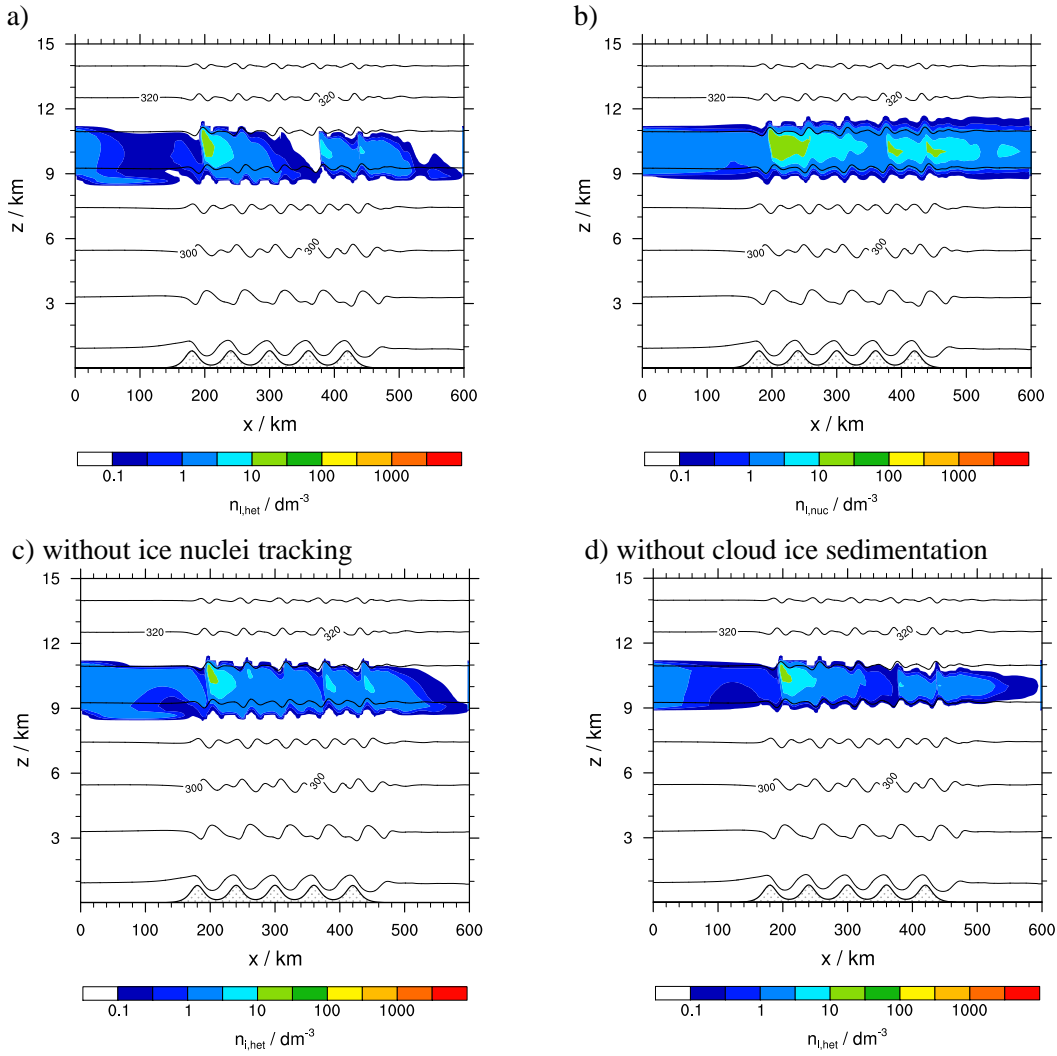
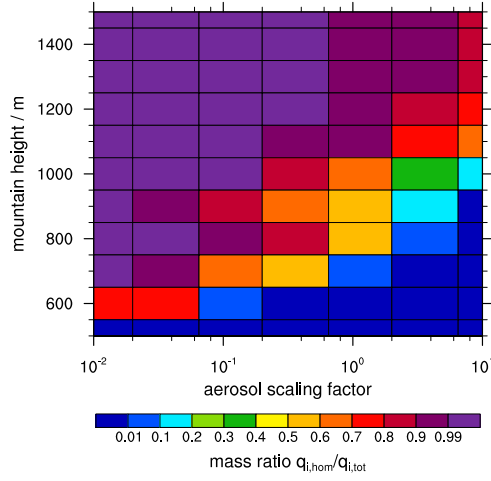


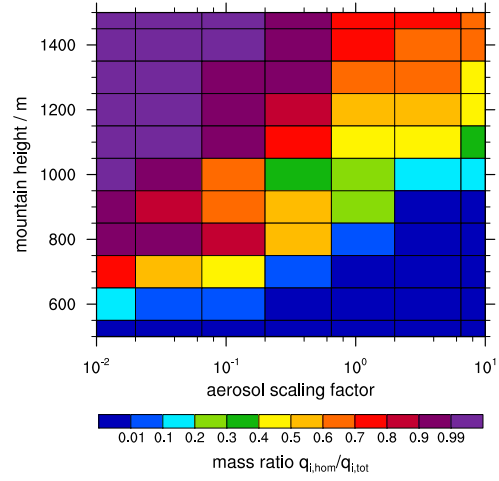
Figure 4.5: Idealised simulations of cirrus cloud developed by heterogeneous freezing after 12h. The ideal setup consists of the mountain height $h_{\max} = 0.8\text{ km}$, the horizontal velocity $u_0 = 12\text{ m s}^{-1}$, the ice supersaturated layer with $RHi = 130\%$ and the factor $\chi_{\text{IN}} = 3$ for the aerosol distribution. The heterogeneously formed cloud ice with cloud ice sedimentation and the limitation of the activated ice nuclei tracking is shown in a). The number density for activated ice nuclei $n_{i,\text{nuc}}$ is shown in b). Simulations without IN tracking and sedimentation are depicted in c) and d), respectively.

The primary gravity wave then serves as an additional trigger for the origin of the ice crystal number density maxima at $x = 200\text{ km}$ with $n_{i,\text{het}} = 50\text{ dm}^{-3}$. Due to the horizontal wind the ice crystals are then advected downstream. A second maxima being a magnitude smaller than the first is then visible over the last hill near $x = 400\text{ km}$ and the ice crystal number density decreases to the right. Thus the tracking of activated ice nuclei reorganises the inner cloud ice crystal distribution while cloud ice sedimentation rather changes the vertical structure. In summary, the introduction of the IN tracking as well as the cloud ice sedimentation process severely alter the spatial structure of cirrus clouds. Consequently these changes in the ice nu-

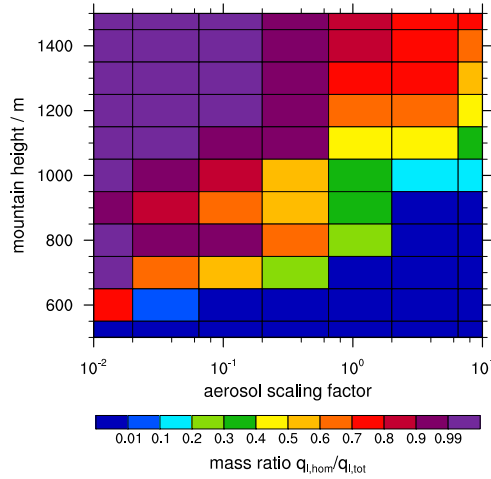
a) full new cloud ice scheme



b) no IN tracking, no cloud ice sedimentation



c) no IN tracking



d) no cloud ice sedimentation

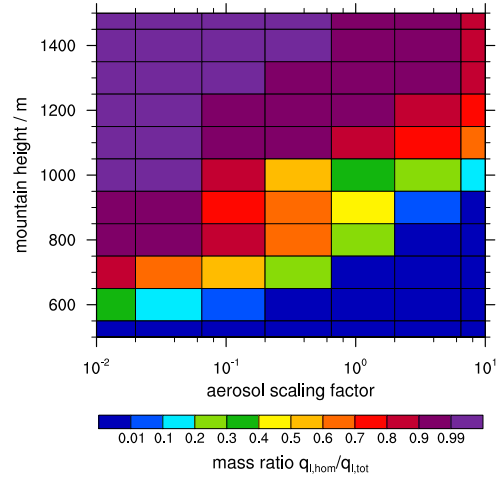


Figure 4.6: Parameter space plot showing the dependency of homogeneous and heterogeneous freezing on orographic forcing and aerosol concentration. The plot a) shows the results with sedimentation and ice nuclei tracking and b) without neither. Figure c) is only with sedimentation and d) is only with the tracking of activated IN.

cleation scheme of the model have a strong impact on the interrelation of heterogeneous and homogeneous nucleation.

Of interest is to individually investigate the impact of the changes made in the cloud ice scheme on the behaviour of the ice nucleation processes, which are depicted in Fig. 4.5. Therefore a parameter study has been performed as to how sensitive the two nucleation mechanisms are with respect to the initial aerosol number density and mountain height. As an aerosol scaling factor $\chi_{IN} = 0.01, 0.03, 0.1, 0.3, 1, 3, 10$ is multiplied to the total of ice nuclei, i.e. the dust, soot and organic quantities. A value of $\chi_{IN} = 1$ represents the IN amount as suggested in Phillips et al. (2008). The maximum mountain height h_{max} for the five hills ranges between 0.5 and 1.5 km for the conducted parameter study.

For the parameter plots in Fig. 4.6 the idealised simulations are sampled over 12 hours regarding the amount of homogeneous cloud ice mixing ratio over the total amount of cloud ice, i.e. $q_{i,\text{hom}}/(q_{i,\text{hom}} + q_{i,\text{het}})$. The focus lies on the effect that the introduction of the ice nuclei tracking variable and cloud ice sedimentation have on the competition between homogeneous and heterogeneous nucleation. In Fig. 4.6a all the cloud ice model changes are included. In Fig. 4.6c the tracking variable is not accounted for, whereas in Fig. 4.6d cloud ice particle sedimentation is not included. In Fig. 4.6b neither of the two are accounted for. The emphasis lies on the diagonal starting at the bottom left corner and ending at the upper right corner. This marks the transition area between the dominant homogeneous freezing for large orographic forcing and low available IN (upper left corner) and the heterogeneous nucleation dominated regime for lower mountain heights and higher IN concentrations (lower right hand corner).

Comparing the full cloud ice scheme in Fig. 4.6a to Fig. 4.6b where the IN budget variable and cloud ice sedimentation are neglected, shows that in Fig. 4.6b the heterogeneous nucleation is dominant. Not accounting for these two changes in the cloud ice scheme leads to an increase in the heterogeneous cloud ice mixing ratio and even influences scenarios with high mountain heights and low IN concentration. Homogeneous freezing dominated regimes are then displaced and only exist for mountain heights above 1000m when there are hardly any ice nuclei available. When only neglecting the tracking variable, the competitive behaviour shown in Fig. 4.6c still looks very similar to plot Fig. 4.6b for strong orographic forcings. However, omitting cloud ice sedimentation modifies the intermediate regimes and extends the transition between the two nucleation mechanisms, as the bigger heterogeneously nucleated ice particles remain in the orographic cirrus cloud and consequently decrease the mass ratio $q_{i,\text{hom}}/q_{i,\text{tot}}$. Thus the parameter study stresses the importance of including these processes in order to achieve a more physical representation of the homogeneous and heterogeneous regimes and their competition.

The idealised simulations lead to the conclusion that, on a small scale, the homogeneous nucleation is a very important process. Furthermore, its substantial dependency on the vertical velocity in order to trigger this process is stressed accordingly. Heterogeneous nucleation, on the other hand, is strongly sensitive to the tracking of previously activated ice nuclei. Cloud ice sedimentation alters the cirrus cloud structure enhancing the dominance of smaller homogeneously nucleated ice crystals as they do not fall out as quickly. The idealised simulations highlight the different cloud ice properties of homogeneously and heterogeneously nucleated ice. Thus it is of importance to include both nucleation mechanisms along with the performed cloud ice scheme improvements in the numerical weather prediction model in order to obtain a more realistic description of the behaviour of cirrus clouds.

4.4.1 Comparison with INCA measurements

Mid-latitude orographic cloud measurements are used to compare the COSMO model in order to see how well the idealised simulations capture realistic events. Hereby INCA (Interhemi-

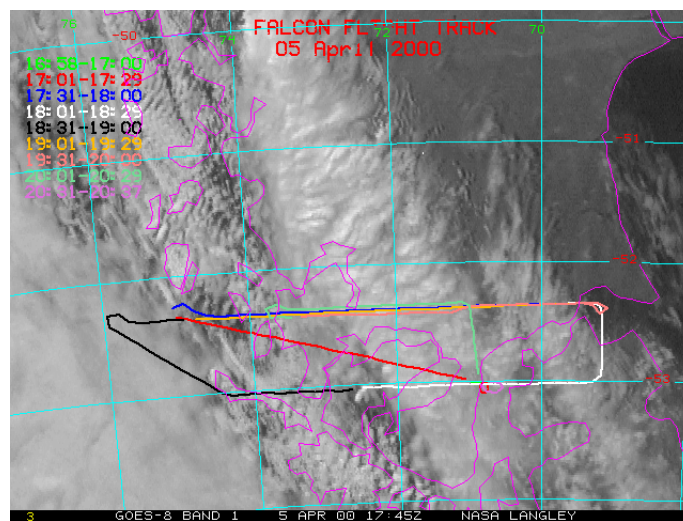


Figure 4.7: DLR Falcon flight path for the INCA campaign on the 5th of April 2000. Of interest is the blue path measured over the time range of 17 : 31-18 : 00h.

spheric differences in cirrus properties from anthropogenic emissions) data (Gayet et al., 2004) measured over Punta Arenas, Chile on the 5th of April 2000 at 18 : 00 UTC was used for comparison. This flight path was chosen as the measurement data include the ice water content and ice crystal number densities for orographic clouds. The respective flight path of the German DLR Falcon at 53°S from 69.2°W to 76°W is depicted in Fig. 4.7. Particle measurements were performed by use of the PMS FSSP-300 optical particle counter and the PMS 2D-C probe. The instruments provide information about the ice crystal diameters from 3 to 800 μm (see Baumgardner et al. (1992) and Gayet et al. (2002)). The parameters derived, which are of interest and will be discussed in the following, are the ice particle number density and the ice water content. The COSMO model setup, initial data and verification is performed analogue to Joos et al. (2009).

For the idealised simulation, a 3D simulation is set up with 40 points in the y -direction. The suitable topography from the National Geographical Data Centre (Hastings et al., 1999) over the Andes is implemented and supplied by Peter Spichtinger. As initial vertical profiles for the temperature, potential temperature, pressure and horizontal wind speed the ECMWF Reanalyse data at 53°S and 78°W used, as shown in Fig. 4.8. The setup also includes an ice supersaturated layer with $RHi = 130\%$ between 8.5 and 9.5km as in the model setup from Joos et al. (2009). Also, Joos et al. (2009) argue that only homogeneous nucleation needs to be considered, as the high vertical velocities and ice supersaturations are assumed to be dominant in orographic cirrus (Kärcher and Strom, 2003). Thus in the performed idealised simulation the aerosol scaling factor is set to $\chi_{IN} = 0.01$ in order to achieve a homogeneously dominated scenario.

The evaluated data depicted in Fig. 4.9 is sampled over 5 hours analogue to Joos et al. (2009). Data utilised from the simulated results lies in the temperature range between 226K and 230K with $RHi > 100\%$ according to the temperatures measured during flight. Plotted in Fig. 4.9 is

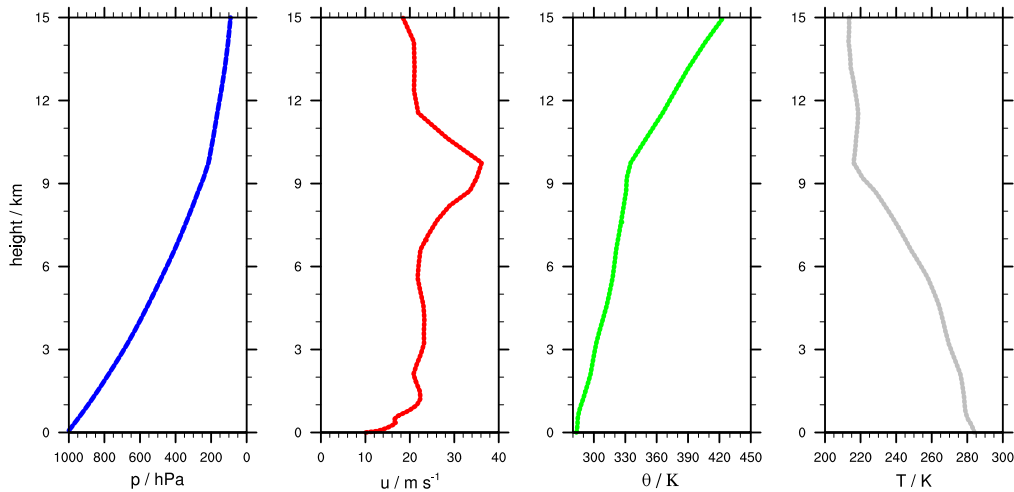


Figure 4.8: Initial vertical profiles from the ECMWF Reanalysis data at 53°S and 78°W for the INCA case study.

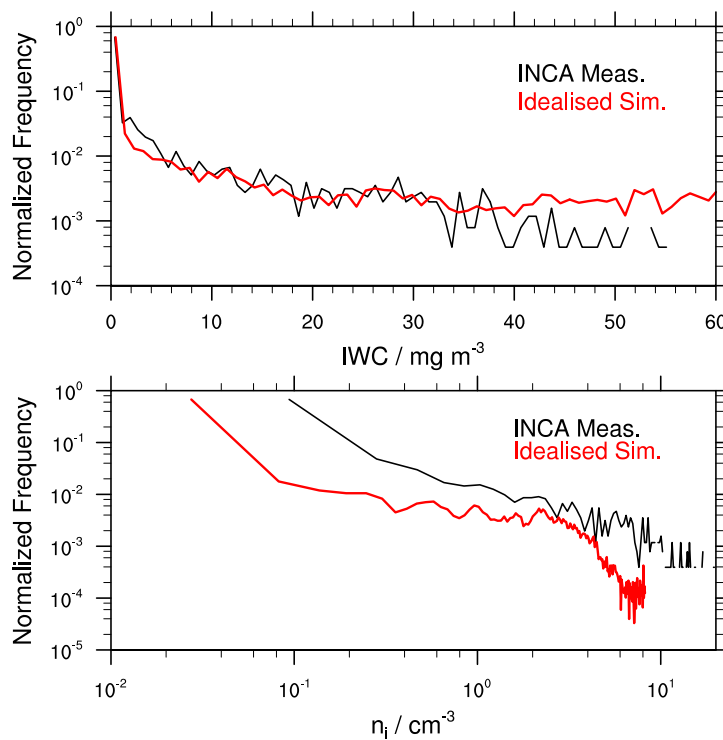


Figure 4.9: The ice water content (top) and the cloud ice number density (bottom) of the idealised COSMO model simulation are compared to the INCA measurements of the 5th of April 2000.

the comparison of the ice water content Fig. 4.9 (top) and ice number density Fig. 4.9 (bottom) of the idealised simulations (red) to the measured INCA data (black). Noteworthy is that the *IWC* for the idealised simulation results from the sum of the cloud ice and snow mixing ratios. As can be seen in the top Fig. 4.9, the overall distribution of the *IWC* is captured well. Yet the

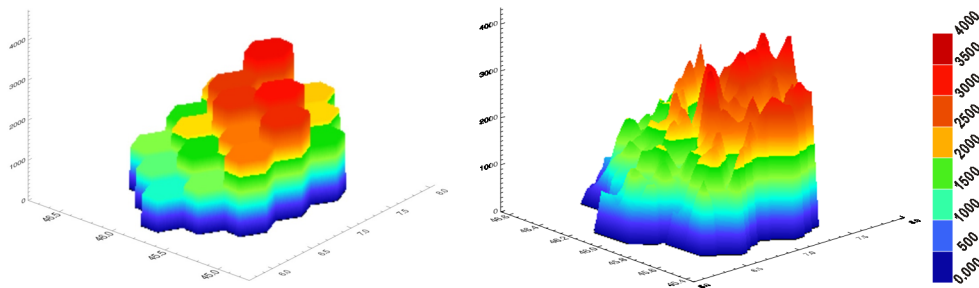


Figure 4.10: The Mont Blanc represented in the GME with a horizontal resolution of $\Delta x = 30$ km (left) and in the COSMO-DE with $\Delta x = 2.8$ km (right).

COSMO model simulations overestimate the IWC above 30 mg m^{-3} where the IWC mainly consists of snow. For the idealised simulation, the frequency of the cloud ice number density n_i is too low for all number densities greater than $n_i = 0.1 \text{ cm}^{-3}$ and includes smaller cloud ice number densities than the INCA measurements. Also, the distribution resulting from the idealised simulation lacks the high values of $n_i = 10 \text{ cm}^{-3}$. The lack in high n_i values indicate a shortcoming of sub scale temperature fluctuations, as homogeneous freezing is the dominant nucleation mode in the idealised simulation. However, the uncertainty of 30% for the particle number concentration and 70% for the ice water content is given in Gayet et al. (2004).

4.5 Case Study With a Refined Regional COSMO-DE

The vertical velocity plays a key role in cirrus cloud formation. In numerical weather prediction models different magnitudes of updrafts are attained depending on their horizontal and vertical resolution. This difference between global and regional NWP models originates, for example, from the representation of the model orography. As an example, the topography of the Mont Blanc is depicted in Fig. 4.10 based on the 1 km^2 dataset Globe (Hastings et al., 1999). The orography with a horizontal GME resolution of $\Delta x = 30 \text{ km}$ is plotted in Fig. 4.10 on the left and with the horizontal COSMO-DE resolution of $\Delta x = 2.8 \text{ km}$ in Fig. 4.10 on the right hand side. The coarser GME grid leads to lower orographic forcing which has a direct feedback on cirrus cloud genesis. This has been studied by means of idealised simulations of orographic cirrus in Sec. 4.4.

In the following, the benefits of the availability of the DWD model chain is exploited. Therefore, a case study for the 26th of August 2011 is conducted by use of a refined COSMO-DE version 4.18 with a horizontal resolution of $\Delta x = 1.7 \text{ km}$, see Sec. 4.5.1. The synoptic situation over Germany on that day consists of an approaching cold front from the west causing frontal cloudiness including cirrus clouds. For this real case simulation the cloud ice mixing ratios of the original COSMO model ice microphysics and the new ice scheme are compared. As reference for the comparison of cloud top heights the Nowcasting Satellite Application Facility Products (NWCSAF) are utilised.

Additionally, the obtained high resolution data set is used for a sub-grid scale variability approach for an enhancement of the vertical velocity in the GME cloud ice scheme derived in Sec. 6.2.3. Hereby the maximum vertical velocities of the COSMO model domain grid points are upscaled to the GME resolution. This is done in order to investigate the sensitivity of the model resolution on the ice microphysical scheme via the updraft.

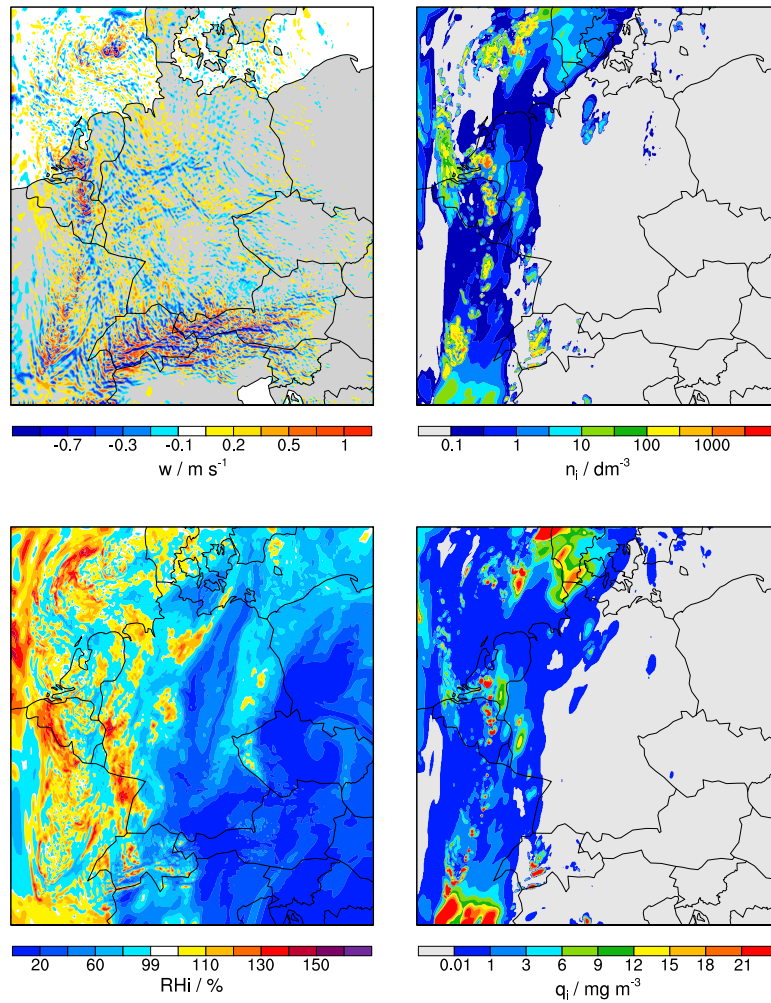
4.5.1 Model Setup

In order to investigate small scale structural effects on cirrus clouds a COSMO-DE with a refined resolution of 1.7 km and the operational 50 vertical layers is used. It needs to be stressed that the microphysical scheme of the COSMO-EU (i.e. without graupel) is used, which is also implemented in the GME as described in Sec. 4.1. For the 26th of August 2011 the whole DWD model chain (GME, COSMO-EU, COSMO-DE) is run for 24 hours, once using the new ice microphysics and once the operational microphysics.

The different model behaviour for both cloud ice schemes are shown in Fig. 4.11 exemplarily for model level 13 with an average pressure of 246.37 hPa. Depicted are the vertical velocity, the ice cloud number density, the cloud ice mixing ratio and the relative humidity over ice for a forecast of 12 hours. In Fig. 4.11a the refined COSMO_{ice} model corresponds to the new ice cloud scheme whereas Fig. 4.11b shows the high resolution COSMO-DE with the COSMO-EU microphysics. The upper plots in Fig. 4.11a show the vertical velocity w and the cloud ice number density n_i between which a strong correlation is noticeable. The regions with high cloud ice number density n_i coincides with those of high vertical velocity w indicating that homogeneous freezing has been triggered. This is supported by the location of the ice supersaturated regions. Also conspicuous are the high values attained by q_i in the regions of homogeneous nucleation.

In comparison, using the operational ice microphysics (Fig. 4.11b) forecasts a structure of cirrus clouds and a relative humidity over ice that look very different. Even though ice supersaturated regions exist, the values of the relative humidity with respect to ice does not often peak over 110%. The horizontal structure of the cloud ice mixing ratio is not as evenly distributed as in Fig. 4.11a but reaches higher local values in total. The number densities can not be compared as this model variable does not exist in the standard COSMO model. The cloud structure is coupled to the ice supersaturated regions and shows no structures arising from high local updrafts. The vertical velocity for the COSMO model is not shown, as it has the same structures as in Fig. 4.11a.

Similar results were obtained at different times and levels (not shown). The real case simulations thus show the expected behaviour with the extended cloud ice scheme. This includes the cirrus cloud structures resulting from high updrafts due to the implementation of homogeneous freezing of liquid aerosols as well as the higher ice supersaturation values. To find out which cloud ice scheme captures the real synoptic cloud structure better, a comparison is conducted with NWCSAF products in the following.

a) COSMO_{ice} model

b) COSMO model

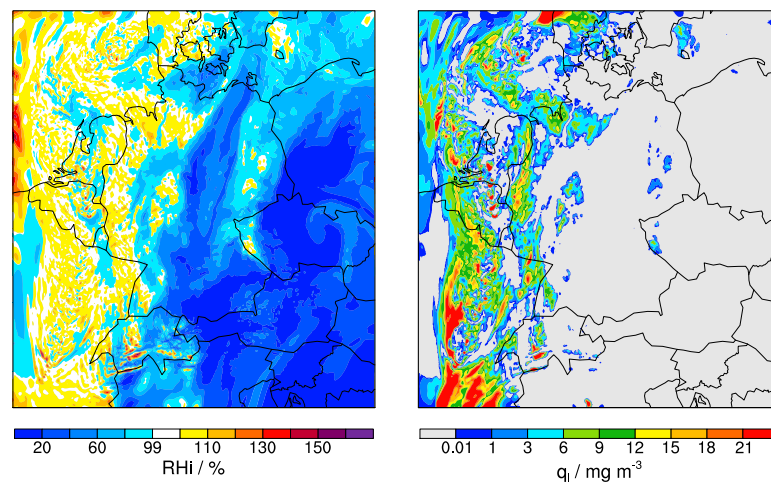


Figure 4.11: COSMO model simulations for the 26th of August 2011 with a forecast of 12h with the new cloud ice scheme a) and the operational ice microphysics b). Shown are the vertical velocity w , ice cloud number density n_i , cloud ice mixing ratio q_i and relative humidity over ice RHi .

4.5.2 Comparison to Meteosat Satellite Data

Data from the main MSG (Meteosat Second Generation) geostationary satellite SEVIRI (Spinning Enhanced Visible and Infrared Imager) are used in order to assess the quality of the refined COSMO-DE forecast for the case study of the 26th of August 2011. SEVIRI is an optical imaging radiometer with four visible and near-infrared and eight infrared channels (Derrien and Gléau, 2005). The SEVIRI data product used is provided every 15 minutes with a horizontal resolution of 5 km, i.e. coarser than the COSMO model run with 1.7 km. Used as reference for the case study is the cloud top height given in steps of 320 m up to about 16 km (EUMETSAT, 2011).

In the following, the COSMO model forecast and MSG data for 26th of August 2011 at 6 UTC are compared. In Fig. 4.12 the cloud top heights from SEVIRI data Fig. 4.12a, the COSMO model run with the improved Fig. 4.12b and operational ice microphysics Fig. 4.12c are depicted. For the COSMO model plots only clouds higher than 4 km are accounted for. Cloud top heights for the COSMO model are determined by the masking of existing mixing ratios for cloud ice, snow or rain greater than 0.1 mg kg^{-1} . The general structure of the cloud band is well captured by the COSMO model simulations although the existence of high clouds is overestimated in the south-west. The simulation with the changed cloud ice scheme in Fig. 4.12b shows an improvement concerning the height of the highest cloud in the north-west lying between 11-12 km rather than between 10-11 km resulting from the operational cloud ice scheme depicted in Fig. 4.12c. Also the horizontal structure of the clouds above 11 km in Fig. 4.12b is more compliant with the SEVIRI data. Yet near 55°N and 10°E an overestimation of clouds and their height is simulated by both COSMO model runs, and the cloud structure is more evenly distributed for the COSMO_{ice} model run.

As the plots are sensitive to the cloud masking threshold it is of interest to know whether the high clouds are of a rather opaque or transparent character. For this, a further cloud product for categorised cloud top height is used, which is depicted in Fig. 4.13a. As such characterizations are not available for the COSMO-DE simulations, the high cloud cover is used as an aid. A striking difference is noticeable for the high cloud structure when using the new ice microphysics. However the operational COSMO model ice microphysics results in an 'all or nothing' opaque cirrus field. Findings by Stapelberg et al. (2010), also using MSG data, show that the COSMO-DE overestimates cloud cover. The new ice microphysics causes a lot more variability in the cloud ice mixing ratio to evolve. Especially the regions for high semi-transparent clouds are captured.

As great differences are noticeable in the horizontal structure of the high cloud structures it is of interest how the cloud top heights of the SEVIRI data compare to the vertical cloud structure of the COSMO and COSMO_{ice} model simulations. Therefore, a cross section at 121°lon for the respective forecast time is plotted. For this purpose the cloud ice mixing ratio is interpolated to the MSG data resolution. Similar results for the vertical structure of the cloud ice field are found previously for the high horizontal clouds. In Fig. 4.14 (lower plot) the operational scheme

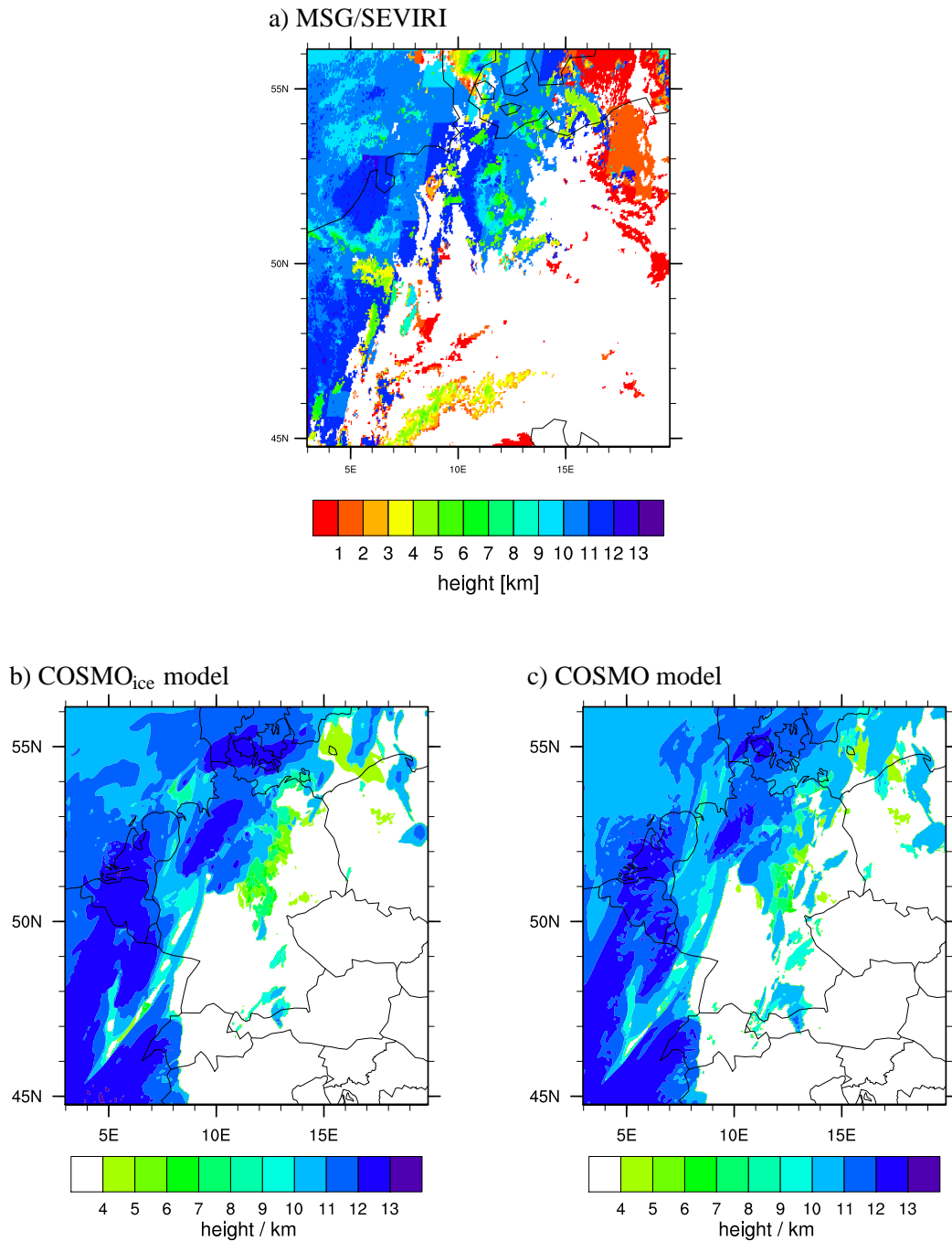


Figure 4.12: Cloud top heights from MSG/SEVIRI a) (Schomburg, pers. communication 2012) and the refined COSMO-DE simulations for the 26th of August 2011 at 6 UTC with the new b) and operational c) ice microphysics. Attention has to be paid to the colour scale differences.

forecasts a cloud ice mixing ratio with a uniform character while the new cloud ice scheme (top) shows more variability. It also reduces cloud cover at 53° lat which is compliant with the MSG data cloud top height (black line). The general reduction of cloud ice explains the existence of high semi-transparent clouds for the COSMO_{ice} model. Interestingly, the vertical spread of the

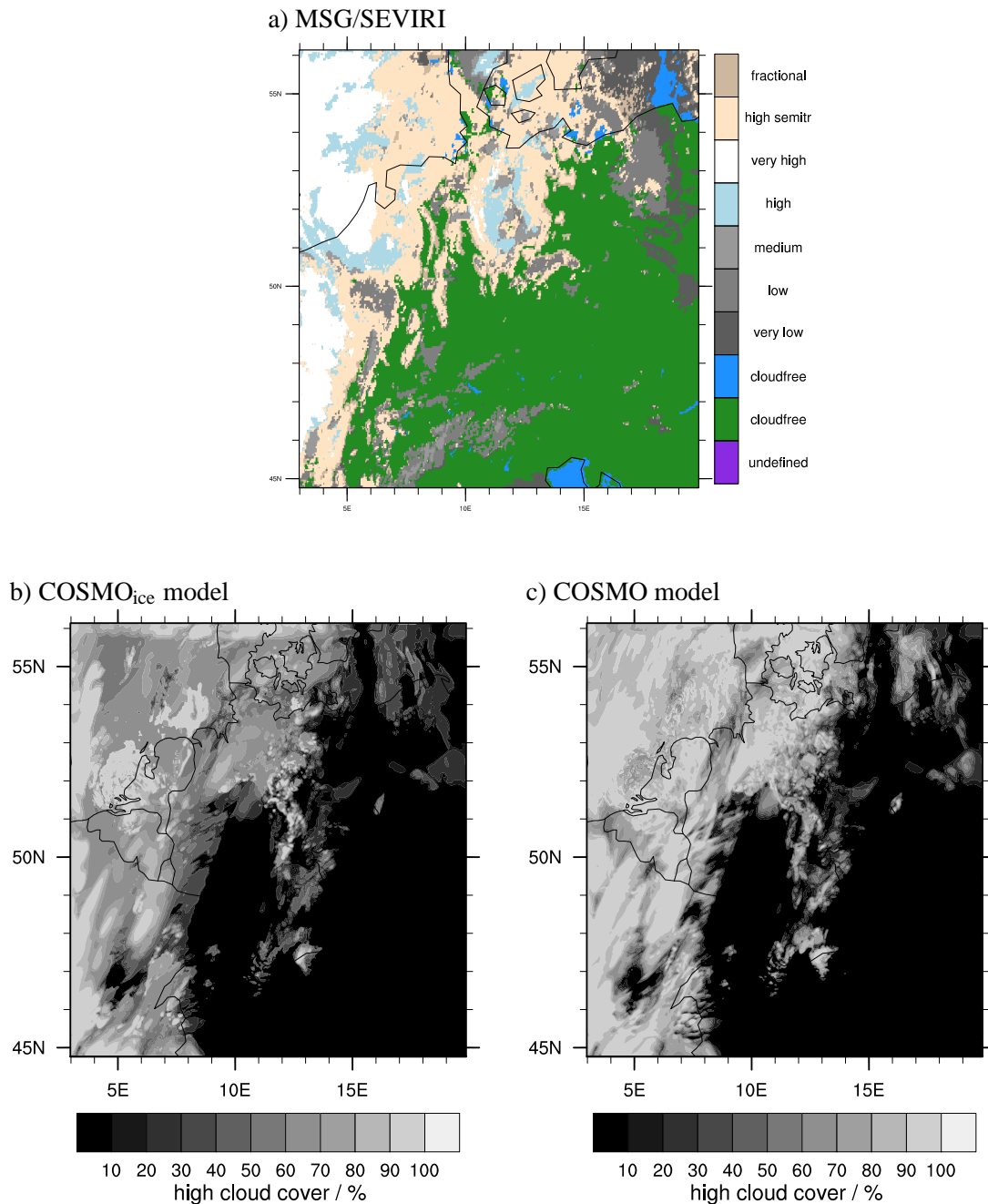


Figure 4.13: Categorized cloud top heights supplied by the NWCSAF Cloud Product are depicted in a) (Schomburg, pers. communication 2012). In b) and c) the percentage of high cloud cover from the refined COSMO-DE simulations with the new and operational ice microphysics is shown, respectively.

cloud ice mixing ratio increases as well. However, the general occurrence of clouds as well as the overestimation of cloud top heights remain unchanged. This is probably due to the model dynamics and water vapour availability.

As was anticipated, the cirrus cloud structures seem to be improved with the new cloud ice

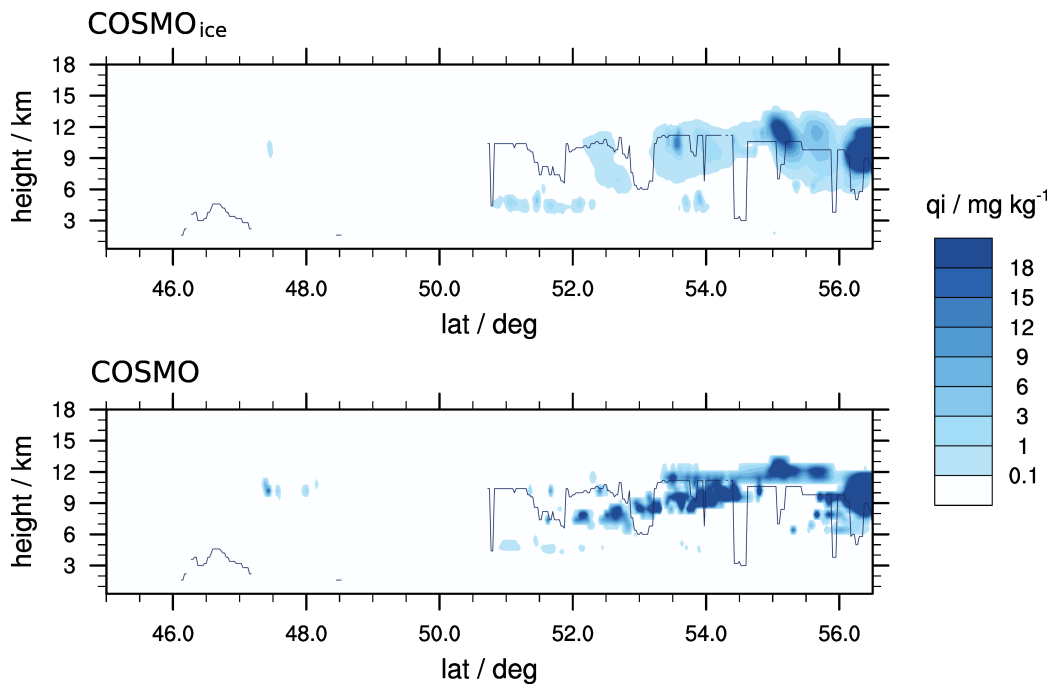


Figure 4.14: Comparison of the cloud cross section of the refined COSMO-DE domain at 121° lon for the 26th of August 2011, 06 UTC. The black line shows the cloud top height for the SEVIRI data. On the top the cloud ice mixing ratio using the new cloud ice microphysics is depicted while the lower plot shows the cloud ice simulated with the operational COSMO model microphysics scheme.

scheme implemented in the COSMO model as high semitransparent clouds are now captured. The structure of high clouds are modified in their horizontal and vertical variability, as opposed to the conform opaque cirrus fields resulting from the operational COSMO model simulations. Nevertheless both models still overpredict cirrus cloud fields in general. The cirrus occurrences are sustained while the magnitude of the existing cloud ice is changed. Further work concerning the evaluation of the new cloud ice scheme in the COSMO model is currently conducted (see Reitter et al. (2013)).

Chapter 5

Comparison of the Cloud Ice and Ice Supersaturation for the GME

In the following, the new and the operational ice nucleation scheme and the ice supersaturation of the global model are evaluated. For this purpose data of the Cloud-Aerosol Lidar and Infrared Pathfinder Satellite Observation (CALIPSO (Winker et al., 2003)) are used for July 2011. These data were obtained from the NASA Langley Research Center Atmospheric Science Data Center. The global model GME (Majewski et al., 2002) version 2.26 is used with a mesh size of 30 km and 60 vertical layers with an icosahedral-hexagonal grid. The microphysics scheme as described in Sec. 4.1 is used. The GME with the implemented new ice microphysics is denoted by GME_{ice} hereafter.

In order to verify the GME and GME_{ice} cloud ice scheme, data from the Cloud Aerosol Lidar with Orthogonal Polarization (CALIOP) is used, which is the primary instrument on the CALIPSO. The CALIPSO mission is part of the Earth System Pathfinder program by the National Aeronautics and Space Administration (NASA) in collaboration with the French space agency Centre National d'Études Spatiales (CNES). CALIPSO was launched in 2006 together with the CloudSat satellite and flies in formation as part of the A-train constellation (Stephens et al., 2002). CALIOP is a near-nadir active remote sensing device with a two-wavelength polarization-sensitive lidar that provides high-resolution vertical profiles of aerosols and clouds. In the mission overview Winker et al. (2009) state that CALIOP is the first polarization lidar to give almost global coverage between 82°N and 82°S. The receiver footprint on the ground has a diameter of 90 m sampled every 333 m along the track and moves with nearly 7 km s⁻¹. The CALIPSO lidar can detect visibly thin clouds missed by radar but can not be used for thicker clouds due to strong attenuation. Unfortunately, the CloudSat radar being more sensitive to larger hydrometeors has not been available after June 2010 (CloudSat Data Processing Center, 2012) at which time the global model GME with a horizontal resolution of 40 km and 40 vertical layers was operational and CloudSat consequently can not be used for this evaluation. Therefore, only upper troposphere and lower stratosphere lidar data is used for evaluating the numerical weather prediction model data. Unless stated differently,

the global model data used for comparison is interpolated to the satellite track by use of the nearest neighbour method. The global model experiments were run with a 24h forecast where the closest hourly model time output to the satellite crossing is chosen. In the following, the emphasis lies on the evaluation of the ice water content and its frequency of occurrence. For cirrus location and the associated IWC the CALIPSO Version 3.01 Level 2 Cloud Profile data is used (Powell et al., 2010). The CALIPSO IWC product is horizontally averaged over 5km and has a vertical resolution of 60m for the altitudes 8.2-20.2km. Investigated are the capability of the GME and GME_{ice} to capture the cirrus clouds as seen by the CALIPSO lidar.

Of further interest is the representation of the ice supersaturation by the global model. This being especially prone to change in the depositional growth in the GME_{ice} . For this comparison the CALIPSO Cloud Profile atmospheric data GEOS-5 (Goddard Earth Observing System) product (Rienecker et al., 2008) is introduced and used. Compared are the frequency of occurrence of the relative humidity with respect to ice exceeding 100% as well as the vertical extent of ice supersaturated regions. As further reference data for the relative humidity with respect to ice the humidity and temperature field data set for July 2011 from the ECMWF Integrated Forecast System (IFS)(see <http://www.ecmwf.int/research/ifsdocs/>) is used.

5.1 Ice Water Content Comparison with CALIPSO Data

A study conducted by Waliser et al. (2009) shows that there are still severe shortcomings concerning the simulation of ice water content in current weather and climate models. In order to counteract this deficit more IWC products are now available for model evaluation like the CALIOP IWC profiles. These profiles are calculated by using the CALIPSO 532nm cloud particle extinction profiles and applying a power law parameterisation. The mentioned parameterisation is derived from remote sensing data and low- and mid-latitude aircraft field campaigns as well as in-situ measurements (Heymsfield et al., 2005). Comparisons of the IWC to the Microwave Limb Sounder (MLS) and in-situ measurements indicate that the CALIPSO IWC retrieval may be as much as a factor of two too low (Wang and Dessler (2012), Avery et al. (2012)). This is partly due to disregarding horizontally oriented ice crystals as they produce deviating high backscatter. As stated by Avery et al. (2012) the sensitivity of the IWC detection has an upper limit of 100 mg m^{-3} . At daytime the minimum detection is 0.4 mg m^{-3} while during nighttime this is improved to 0.1 mg m^{-3} due to a better signal-to-noise ratio (Avery et al., 2012).

As an example of the IWC profiles an arbitrary piece of the CALIPSO track with high cloud occurrence is depicted in Fig. 5.1 for July 7th, 2011 at 15:25:26 until 15:38:28 UTC. Shown in Fig. 5.1 is the IWC product from the CALIOP space-based lidar and the model data output from the GME and GME_{ice} interpolated to the satellite track by use of the nearest neighbour method. The processed data consists of model forecasts which are closest to the satellite crossing time. The lidar path section shown in Fig. 5.1 is only used to demonstrate the used data. The shaded grey area below 8km indicates where the CALIOP data is not as reliable due to

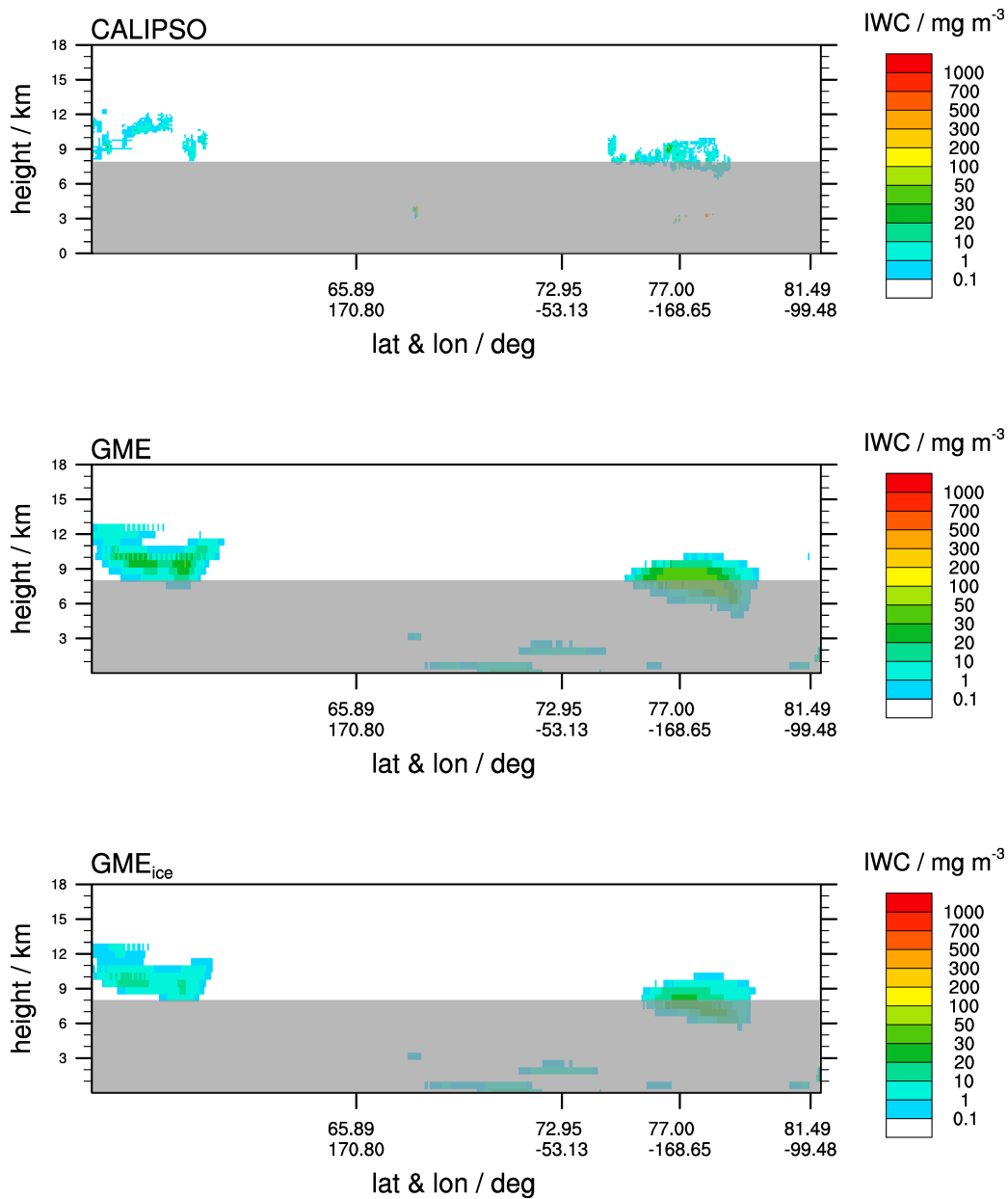


Figure 5.1: The ice water content on the CALIPSO track on July 7th 2011 between 15:25:26 and 15:38:28 UTC. On the ordinate are the latitude and longitude position of the satellite beneath each other. The shaded grey area below 8km indicates where the CALIOP data is not as reliable due to strong attenuation (Avery et al., 2012). The top plot depicts the IWC derived from the CALIOP data. The GME (middle) and GME_{ice} (bottom) model forecasts at the respective satellite crossing time is interpolated to the CALIPSO track.

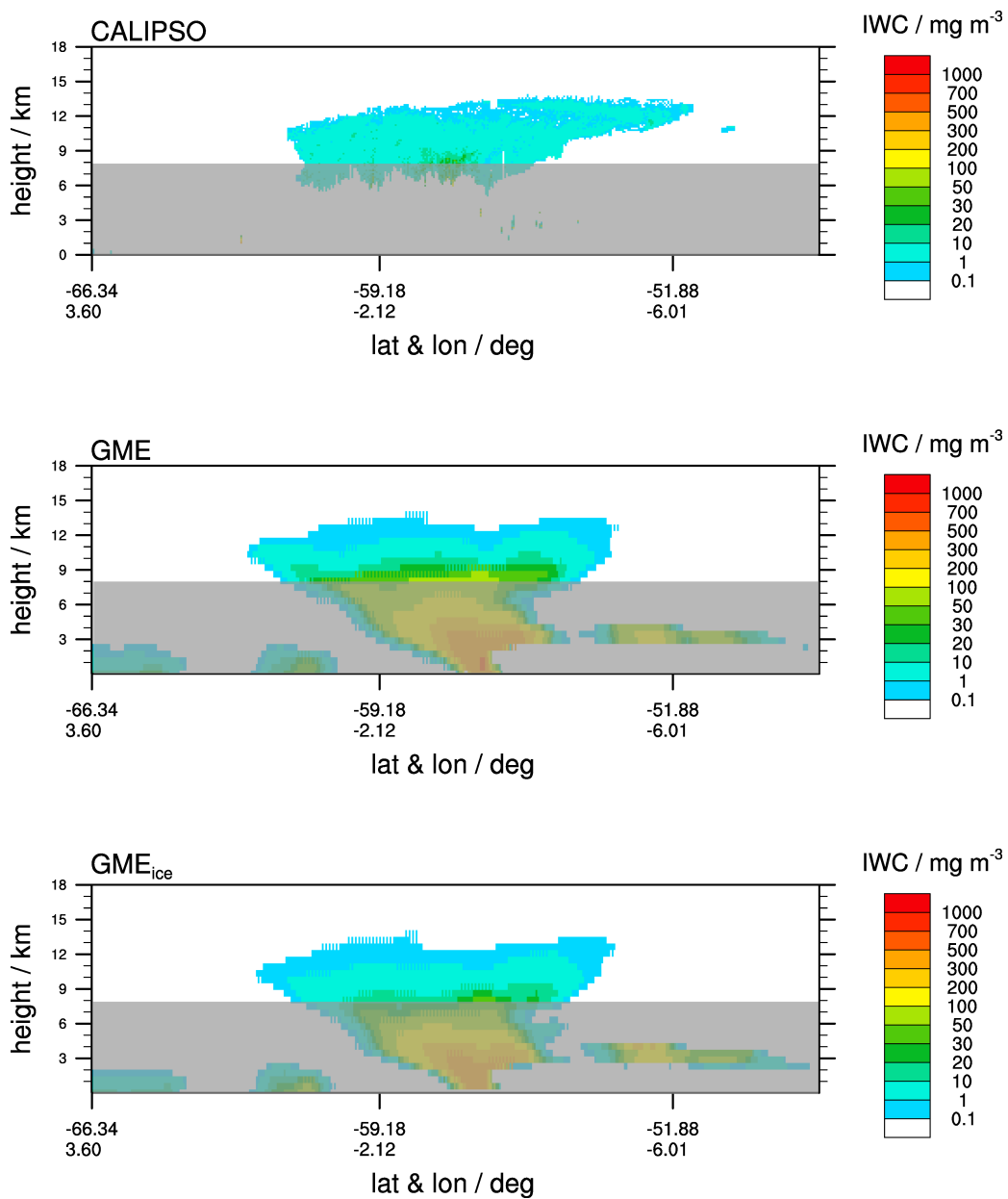


Figure 5.2: As in Fig. 5.1 the ice water content on the CALIPSO track is depicted, but on July 7th 2011 between 14:46:18 and 14:51:30 UTC. On the ordinate are the latitude and longitude positions of the satellite beneath each other. The shaded grey area below 8 km indicates where the CALIOP data is not as reliable due to strong attenuation (Avery et al., 2012). The top plot depicts the IWC derived from the CALIOP data. The GME (middle) and GME_{ice} (bottom) model forecasts at the respective satellite crossing time is interpolated to the CALIPSO track.

strong attenuation (Avery et al., 2012). Nevertheless, the difference in IWC resulting from the different ice microphysics schemes from the GME and GME_{ice} is as expected. Observable is the same location of the clouds for all three plots. However, the magnitude of the IWC and the vertical and horizontal extent of the cirrus clouds differ. The IWC from the CALIPSO data seems fragmentary and the IWC only reaches values around 20 mg m^{-3} , whereas the simulated cirrus has a more opaque structure and reaches 33 mg m^{-3} for the GME_{ice} data and even higher values of 48 mg m^{-3} for the GME data.

A further CALIPSO track is plotted in Fig. 5.2 to show the CALIPSO behaviour for a frontal or convective weather situation on July 7th, 2011 between 14:46:18 and 14:51:30 UTC. The anvil and detrainment zone is visible in the CALIPSO plot (top). This is not observable in the GME and GME_{ice} . What is also of importance in Fig. 5.2 is the missing high ice water contents in the core of the cloud for the CALIPSO IWC product. This is due to the strong attenuation caused by the high IWC or larger hydrometeors. Thus high IWC contents and lower clouds have to be treated with caution, as the CALIPSO lidar may not be able to capture these events. As these are only two individual cases, it is of interest to see the general properties and occurrences of the global ice water content as represented by the CALIPSO, GME and GME_{ice} .

5.1.1 Zonal and Meridional Ice Water Content Averages

Evaluations with the CALIOP IWC product are limited to heights above 8km where the IWC is more reliable due to less attenuation (Avery et al., 2012). In order to see the whole vertical extent of the global distribution of the IWC, first, only the GME and GME_{ice} are considered. The main sources for ice clouds include the storm tracks (baroclinic wave activity) in the mid-latitudes and the detrainment of deep convection in the tropics, thus resulting in local maxima in 300hPa and 600hPa (Ma et al., 2012), corresponding to 4km and 9km. These local maxima can also be observed in the global zonal mean plots in Fig. 5.3. The plot depicts daily 24 hour data means which are averaged over the month of July 2011. A polar stratospheric cloud (PSC) clearance was performed in the Antarctic. PSCs normally develop at the beginning of June and consist of either ice or nitric acid. As the latter is not included in the model and PSCs are not of concern at this point the clouds above 9km and between 84°S and 60°S are removed, analogous to Delanoë et al. (2011). Shown are the grid scale cloud ice mixing ratios q_i on the left and ice water contents $\rho_a(q_i + q_s)$ on the right hand side for the GME (top), the GME_{ice} (middle) and the GME_{ice} without cloud ice sedimentation (bottom).

When considering the cloud ice in the mid-latitudes on the left hand side of Fig. 5.3 large differences in the magnitude and location can be seen. In Fig. 5.3a the region of maximum cloud ice in the GME output lies about 2 to 3km higher and is narrower than in the plots Fig. 5.3b and Fig. 5.3c from the GME_{ice} simulations with and without sedimentation, respectively. The cloud ice sedimentation shows the biggest influence on the magnitude of the cloud ice mixing ratio when considering all of the individual changes conducted in the cloud ice scheme. In Fig. 5.3c the cloud ice mixing ratio obtains peak mean values over 10 mg m^{-3} as does the global mean

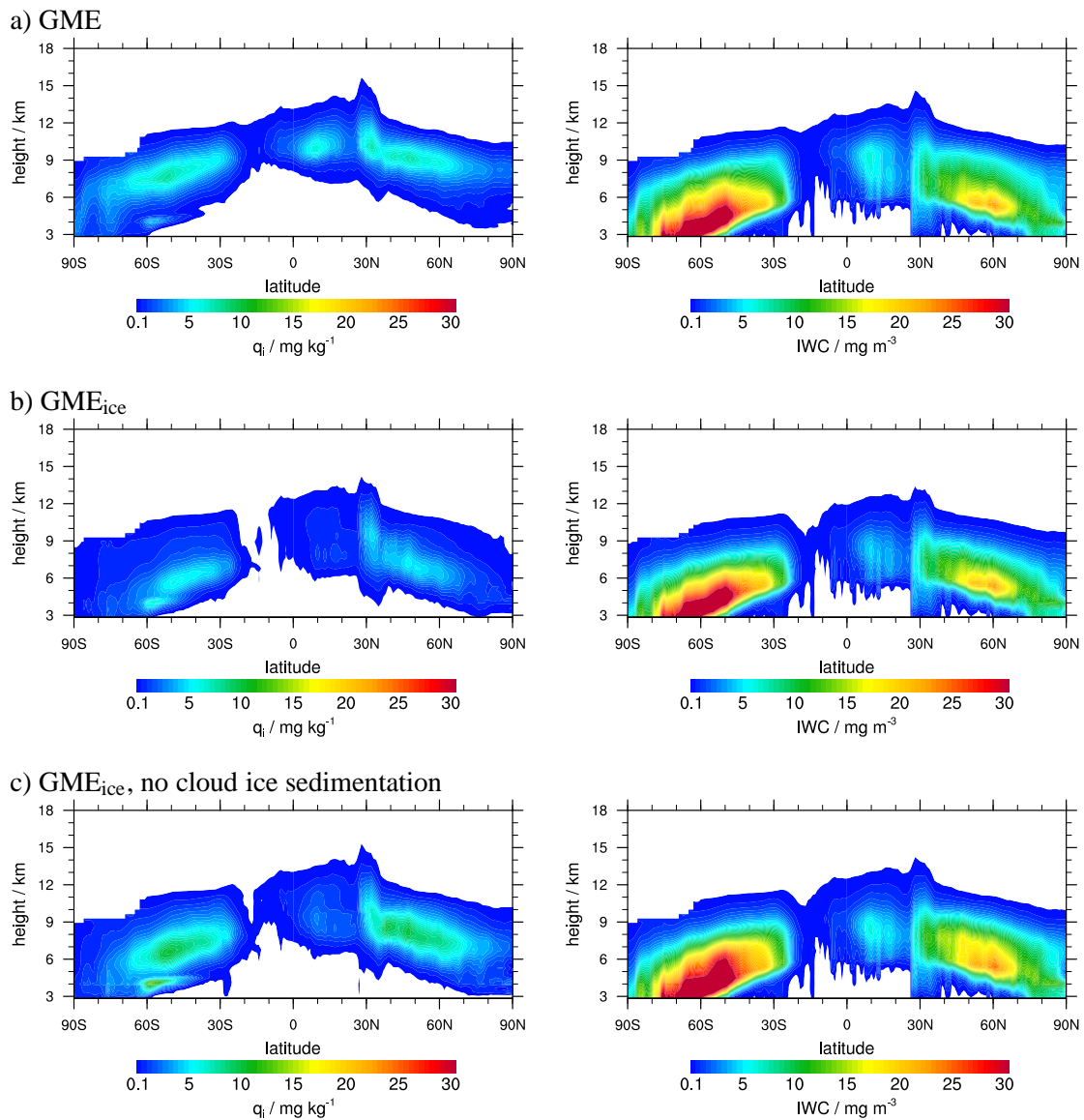


Figure 5.3: Meridional monthly mean over July 2011 of the cloud ice and ice water content for the standard GME (top), the new ice scheme GME_{ice} (middle) and the GME_{ice} without cloud ice sedimentation (bottom).

of q_i in Fig. 5.3a, but the areas where these local maxima arise are much wider spread. This demonstrates how crucial the results in global mean values can differ by including or excluding single microphysical processes.

In Fig. 5.3 the expected maximum in the tropics is not very pronounced in all plots. This might be due to the missing contribution of the sub-grid scale hydrometeors which are not included here and shortcomings in the convective detrainment. Furthermore, verification of the GME using radiosondes show that the atmosphere is too stable in the tropical region (Fröhlich, pers. communication 2009). The new ice nucleation parameterisation is not thought to influence this shortcoming as it is not coupled to the convection scheme. Nevertheless, Fig. 5.3b and Fig. 5.3c

do show a reduction of cloud ice in the tropics. The indicated reduction is due to the typical pattern of high cloud cover over the ITCZ (inner tropical convergence zone) at the beginning of the West African monsoon. A further reason for less ice clouds being expected in this region is the descending of the Hadley cell. The mentioned ice cloud minimum over 20°S (North Africa, North Australia) can also be observed in the mean ice cloud occurrence depicted in Fig. 4 in Delanoë et al. (2011). The mentioned plot is based on CloudSat observations on the MetOffice and ECMWF grid in comparison to the model data, respectively, for the last three weeks of July 2006. Thus it follows from comparison to the findings of Delanoë et al. (2011) that the cloud ice mixing ratio with the new cloud ice scheme is capable of reproducing this phenomenon while the operational cloud microphysics overpredicts the ice clouds in this region.

The right hand side of Fig. 5.3 shows the zonal global mean of the ice water content. A problem when regarding the ice water content is that it is the sum of the cloud ice and the snow with snow being the dominant hydrometeor. As a result, changes in the smaller cloud ice quantity are hard to detect. Differences in IWC are thus not quite as pronounced as for the cloud ice mixing ratio by itself. However, noticeable are the lower IWC occurrences at 20°S with the new ice microphysics for reasons discussed above. Also the top height is lower when introducing the cloud ice sedimentation.

After this short overview of the meridional distribution of cloud ice over all heights, the GME and the GME_{ice} are now compared to the CALIOP lidar IWC product. For this the GME and the GME_{ice} model data interpolated on the CALIPSO track are evaluated for July 2011. Also, the CALIPSO data is interpolated on the GME vertical altitudes for better comparison in this study. First, the ice water content is regarded between the total height of 8 and 15 km and it is later vertically partitioned.

In the following, the differences in the global averages of the GME, the GME_{ice} and the CALIOP product IWC are investigated. The first plot Fig. 5.4 shows the mean over the height between 8 and 15 km. The upper plot shows the global mean over all lidar granules in July 2011 for the CALIOP IWC product. The middle plot depicts the mean of the interpolated model data of the GME and the lower plot for the GME_{ice} . On the right hand side of each plot is the zonal mean over the latitude with a minimum of 0.1 mg m^{-3} and a reference line at 1 mg m^{-3} to facilitate the comparison.

The overall global structures of occurrence of higher mean IWC in the polar, mid-latitude and tropics are captured by the global numerical weather prediction models in Fig. 5.4. Peak IWC values are reached at 30°S and in the ITCZ, which lies at about 5°N during the northern hemispheric summer. Comparisons of the zonal means of the CALIPSO IWC product (top) to the GME (middle) show the overprediction of the ice water content of the GME for the mid-latitudes. The greatest outliers can be found above the Himalayan region, where peak amounts over 30 mg m^{-3} are reached in the GME and the GME_{ice} . That might be a consequence of errors in the extinction retrievals of the CALIPSO which increase with cloud optical depth (Winker et al., 2009). However, the GME also overpredicts the IWC in the southern hemisphere mid-latitudes. This is not the case for the GME_{ice} as both, the CALIPSO and the GME_{ice} zonal

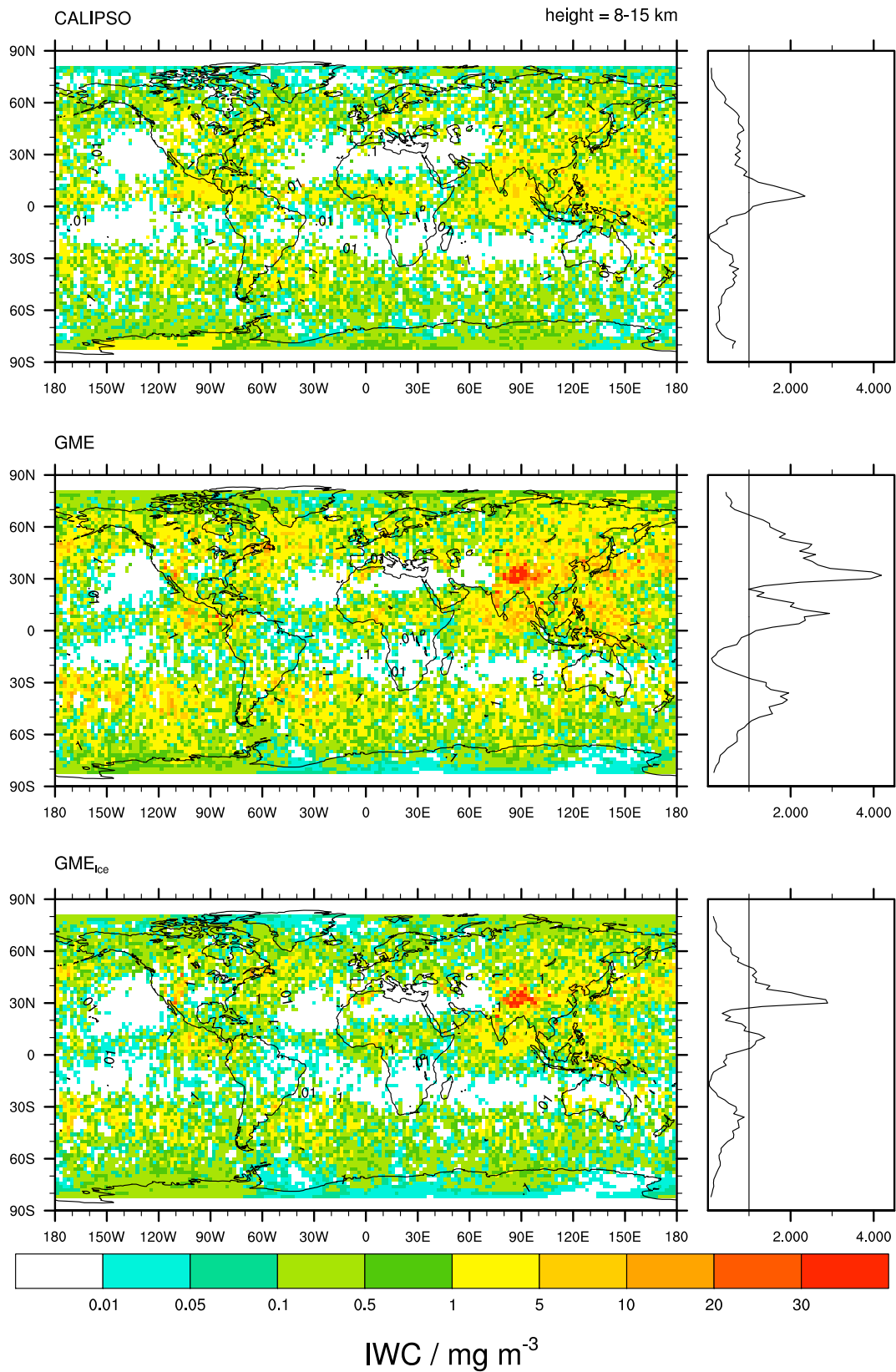


Figure 5.4: Global map of the average ice water content for the altitude between 8 and 15 km. The upper plot depicts the mean CALIPSO lidar data, the middle plot the interpolated GME and the lower plot the GME_{ice} model data. On the right hand side is the zonal mean for the range of 0.1-4.5 mg m⁻³ with a reference line at the zonal IWC magnitude of 1 mg m⁻³.

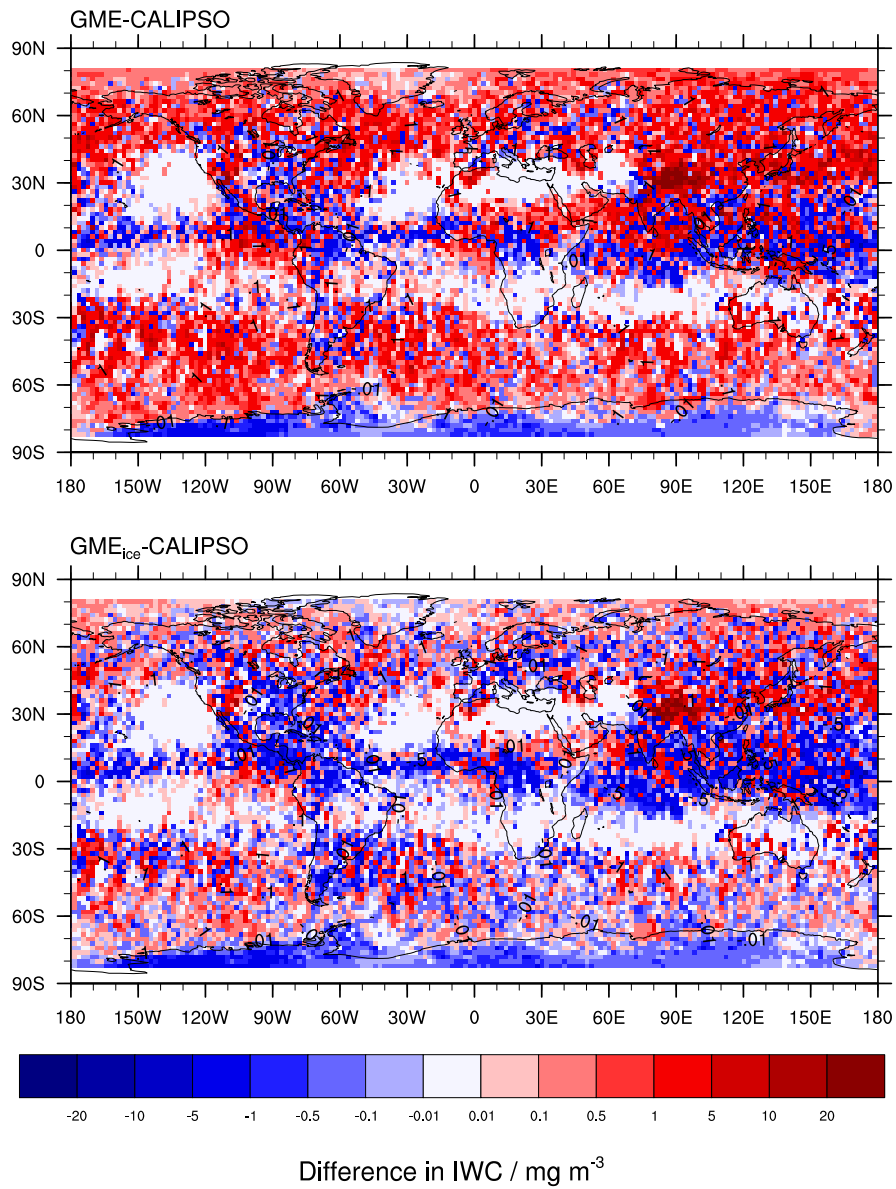


Figure 5.5: Difference of the mean ice water content for the altitudes between 8 and 15 km as previously depicted in Fig. 5.4. The top plot shows the difference between the CALIPSO and the GME and the bottom plot depicts the difference between the CALIPSO and the GME_{ice}.

mean lies below 1 mg m^{-3} . On the other hand GME_{ice} underpredicts the mean IWC in the tropics which was also observed and discussed for Fig. 5.3.

In Fig. 5.5 the differences of the depicted IWC fields in Fig. 5.4 of the CALIOP IWC and the GME (top) as well as the CALIOP IWC and the GME_{ice} (bottom) are plotted. Red represents an overprediction in mean ice water content while the blue colour is a sign for IWC underprediction. The top plot Fig. 5.5 is dominated by an overprediction of the ice water content simulated by the GME in the mid-latitudes and polar region in the northern hemisphere. The differences in ice water content lie in the magnitude between 1 to 5 mg m^{-3} but also attaining values around 10 mg m^{-3} . Also, an underprediction of ice water content in the southern polar region and tropics of about -5 mg m^{-3} is shown. Underprediction is also observable in the difference plot between the averaged CALIPSO IWC product data and the GME_{ice} model output at the bottom of Fig. 5.5. In this plot the other regions show a rather mixed behaviour and no clear structures. However, the regions of high overpredictions are significantly reduced and only reach differences up to 1 mg m^{-3} . The IWC underpredictions are the same for the GME and the GME_{ice} .

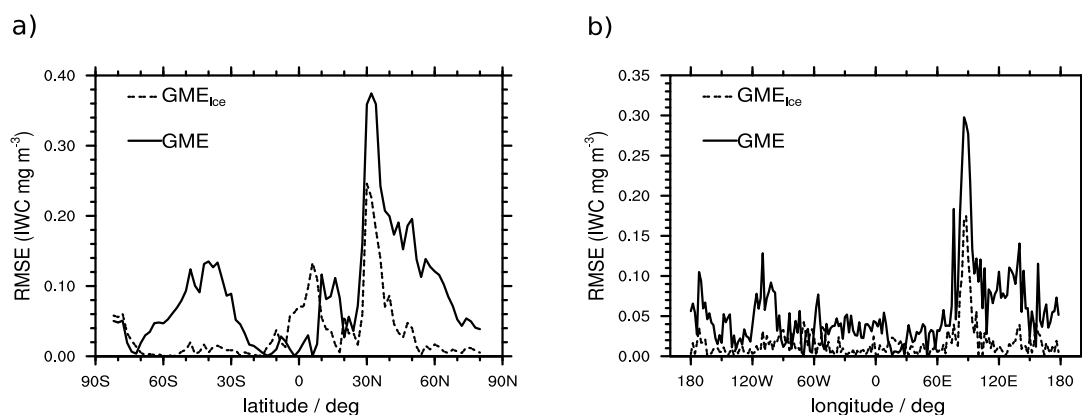


Figure 5.6: Root mean square error of the IWC frequency between 8km and 15km for the CALIPSO data and GME and GME_{ice} over a) latitude and b) longitude.

As an error metric for the model performance, the root mean square error (RMSE) is applied. This measure for the difference between the observations X_{obs} and the forecast model value X_{model} at time and space i for the number of points n is defined by

$$\text{RMSE} = \sqrt{\frac{1}{n} \sum_{i=1}^n (X_{\text{obs},i} - X_{\text{model},i})^2}. \quad (5.1)$$

The RMSE is calculated for the averaged IWC field between 8 and 15 km as depicted in Fig. 5.4. Values of the RMSE near to zero indicate a good model prediction performance. Fig. 5.6 shows the RMSE resulting from the difference of CALIPSO and GME/ GME_{ice} data. For these plots the model and satellite data are additionally averaged over latitude and longitude. The RMSE is then calculated over the mean latitude and longitude values, depicted in Fig. 5.6a and Fig. 5.6b, respectively. The unit of the RMSE is, according to the variable, mg m^{-3} for the ice water content. When looking at the difference between the two model outputs in Fig. 5.6b, the RMSE

for the dashed line resulting from the lidar and the GME_{ice} data is greatly reduced compared to the RMSE resulting from the CALIPSO and the GME data. That is also true for the latitudinal distribution in Fig. 5.6a with the exception of the tropical region. In this region the GME_{ice} has a shortcoming in comparison to the GME. The ice water content is underpredicted in this region which is in accordance to the findings of the zonal mean in Fig. 5.4. The peak at $30^\circ N$ in Fig. 5.6a and $90^\circ E$ Fig. 5.6b corresponds to the IWC maximum over the Himalayan region.

The above mentioned behaviour provides an overall idea of the averaged IWC for the UTLS. In order to see how the IWC magnitudes differ with height, a vertical sub-division will give a more detailed insight into the model behaviour. Now the heights are sub-divided into 8-10 km, 10-12 km and 12-15 km depicted in the plots Fig. 5.7, Fig. 5.8 and Fig. 5.9, respectively. In the following figures, the CALIPSO IWC product is always depicted at the top, the GME IWC averages in the middle and the GME_{ice} IWC averages at the bottom. On the right hand side is the zonal mean with a reference line at 1 mg m^{-3} as used before.

In Fig. 5.7 the mean IWCs for the lowest levels between 8-10 km is shown. Even though the GME and the GME_{ice} capture the overall cloud structures the GME output shows a severely higher global magnitude in ice water content. The GME_{ice} model output has lower magnitudes than the GME but still locally overestimates the IWC by $5\text{-}10 \text{ mg m}^{-3}$ in comparison to the CALIPSO IWC product, not considering the peak in the Himalayans. In question is to what extent the model representations are erroneous as greater cloud optical depths might have led to the small IWCs of the lidar product. Also, it has to be kept in mind that the IWC content might be of a factor two too low, as stated before.

In the upper troposphere, lower stratosphere (UTLS) averaged data between 10-12 km (Fig. 5.8) the GME is able to represent the IWC magnitudes of the CALIPSO data. However, the GME has a higher cloudiness especially at $10\text{-}20^\circ S$. This is also true for the GME_{ice} although the IWC is reduced. Other than that, the GME_{ice} ice water content does not reach zonal means higher than 0.2 mg m^{-3} in the mid-latitudes, which is much lower than the CALIPSO and GME data zonal means. This shortcoming is also visible in the upper vertical sub-division between 12-15 km in Fig. 5.9, which is only relevant for the tropics.

The ice water content behaviour is also investigated by use of relative frequency in Fig. 5.10. Again the sub-division for 8-10 km and 10-12 km is made in Fig. 5.10a and Fig. 5.10b, respectively. For lower altitudes between 8-10 km depicted in Fig. 5.10a, the GME_{ice} shows a more similar behaviour to the CALIPSO IWC product than the GME, especially in the mid-latitudes. The mentioned is not the case for the heights between 10 and 12 km in Fig. 5.10b, where the lidar IWC and GME model output show the same relative frequencies in the tropics and mid-latitudes. When comparing the GME_{ice} with the GME their difference is very clear. The GME constantly shows higher frequencies in ice water content magnitudes, especially when it comes to high values. In the GME_{ice} , the initial ice nuclei distribution is assumed to be the same over all heights. Introducing a height dependent distribution would change the amount of ice water content resulting from heterogeneous nucleation, fitting it to the lidar IWC.

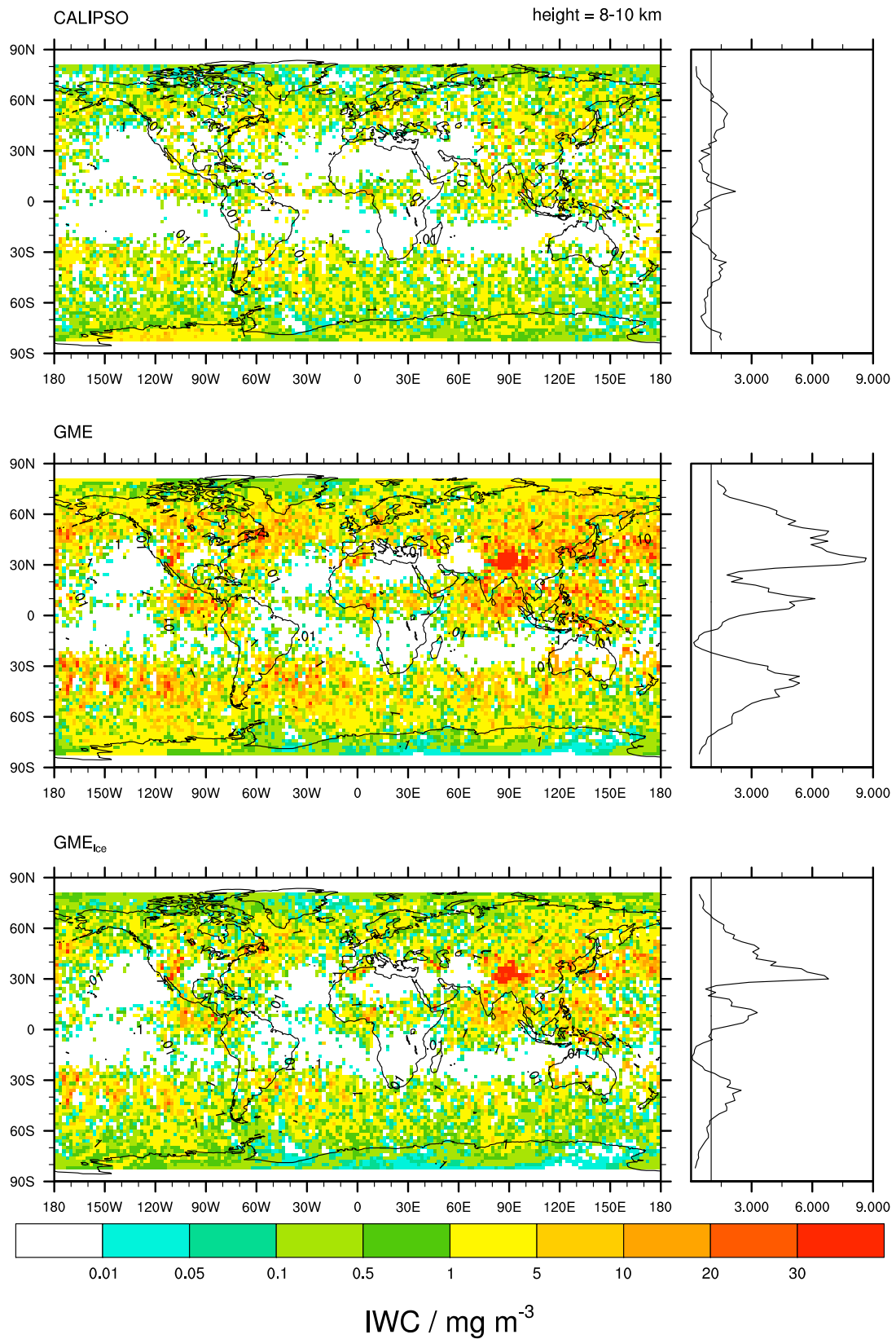


Figure 5.7: Global map of the mean of ice water content from the CALIPSO IWC Product (top), the GME (middle) and the GME_{ice} (bottom) for the altitude between 8 km and 10 km. On the right hand side is the zonal mean for the range of 0.1-9 mg m⁻³ with a reference line at the zonal IWC magnitude of 1 mg m⁻³.

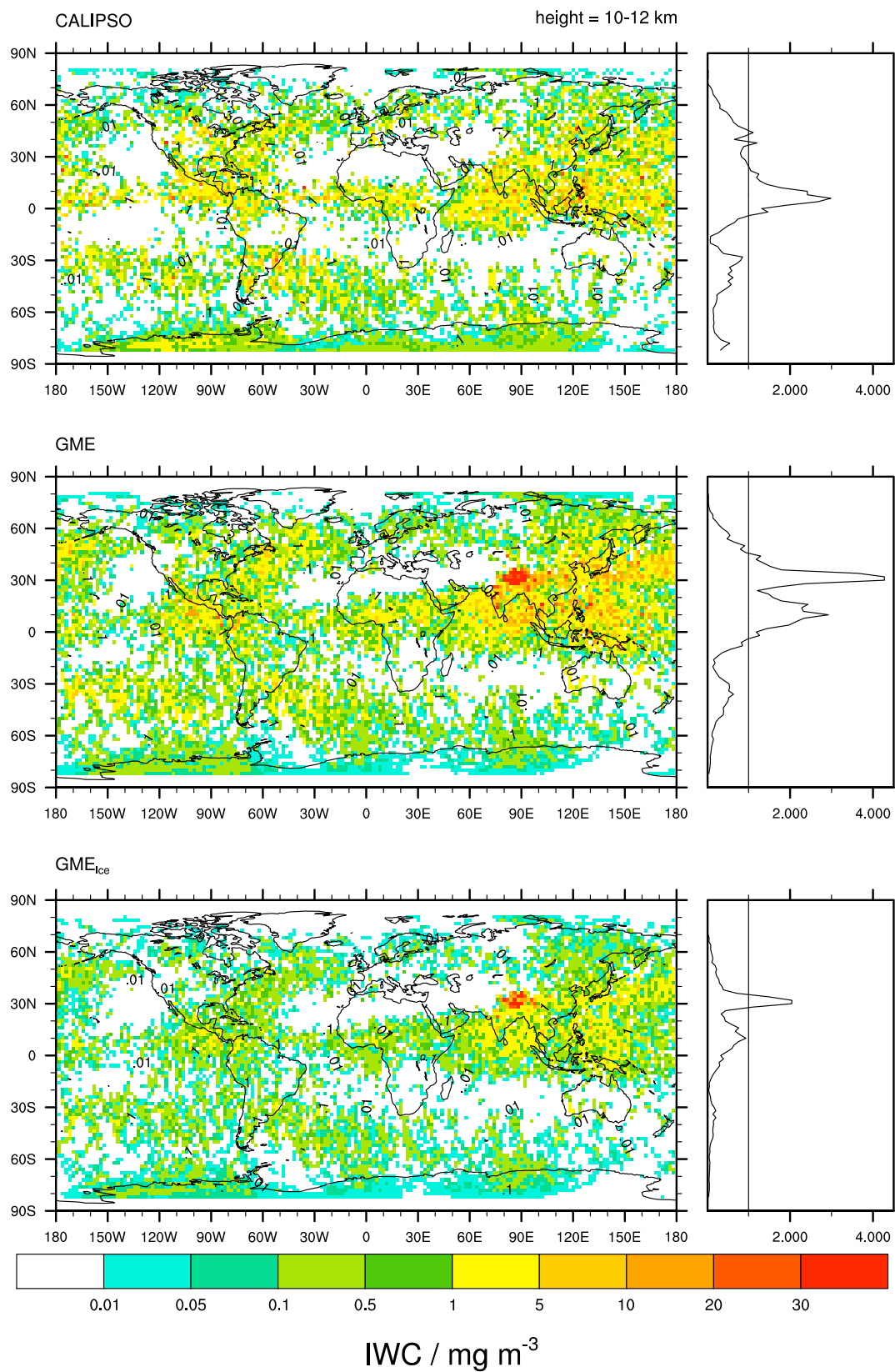


Figure 5.8: As Fig. 5.7 global map of the mean ice water content but for the altitude between 10km and 12km. On the right hand side is the zonal mean for the range of 0.1-4.5 mg m^{-3} with a reference line at the zonal IWC magnitude of 1 mg m^{-3} .

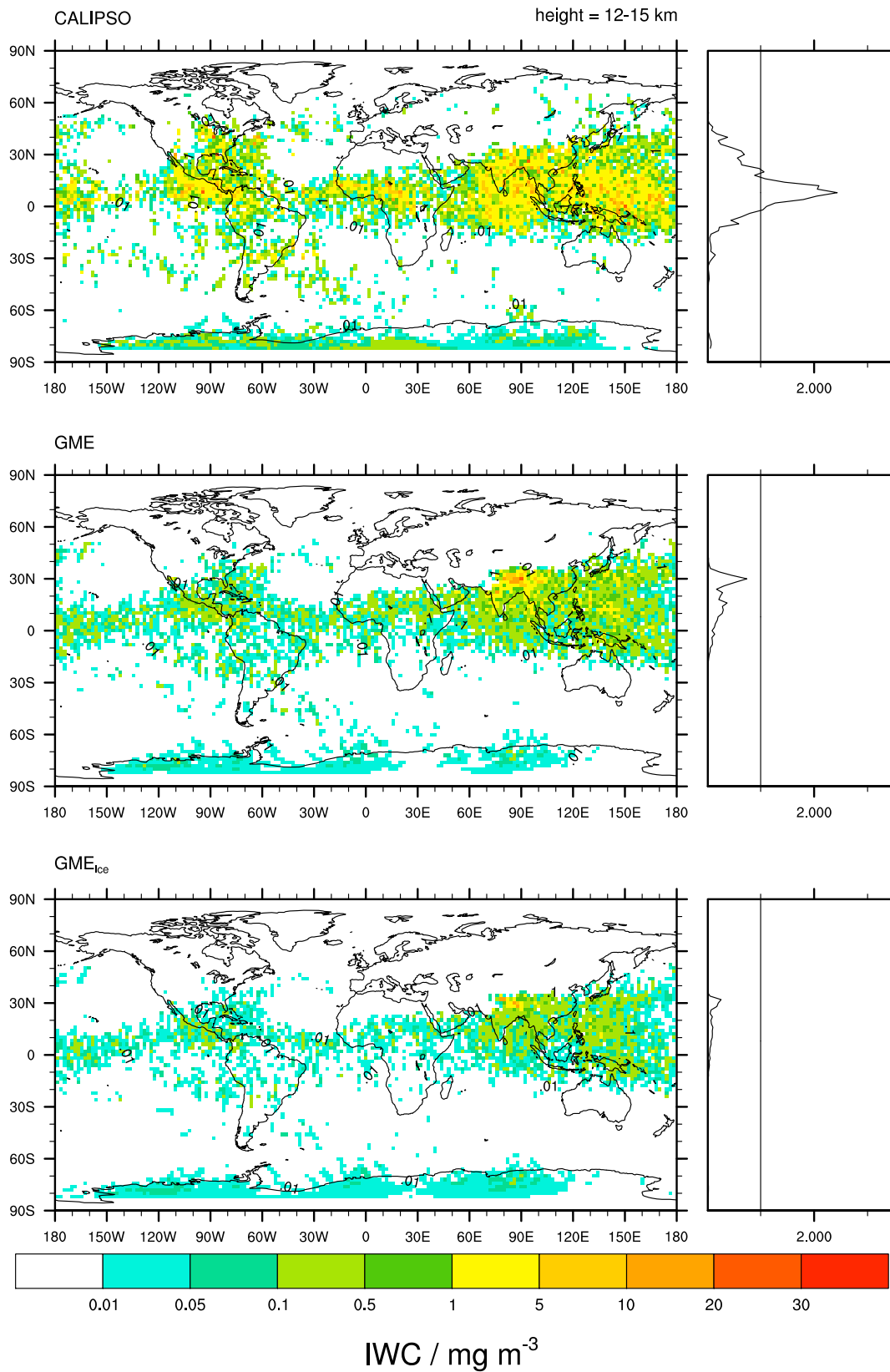


Figure 5.9: As Fig. 5.7 global map of the mean ice water content but for the altitude between 12km and 15km. On the right hand side is the zonal mean for the range of 0.1-2.5 mg m^{-3} with a reference line at the zonal IWC magnitude of 1 mg m^{-3} .

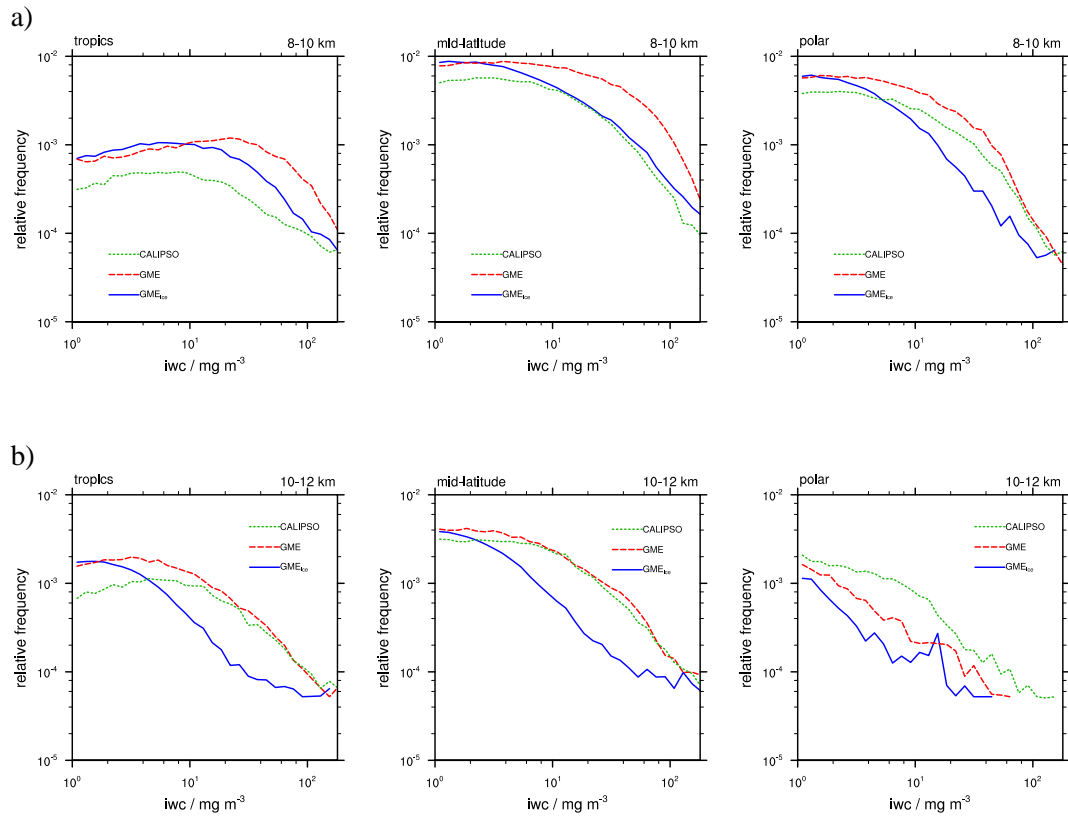


Figure 5.10: Relative frequency for the CALIPSO, the GME, and the GME_{ice} ice water content between 8-10km (top) and 10-12 km (bottom) for the tropics, the mid-latitudes, and the polar regions.

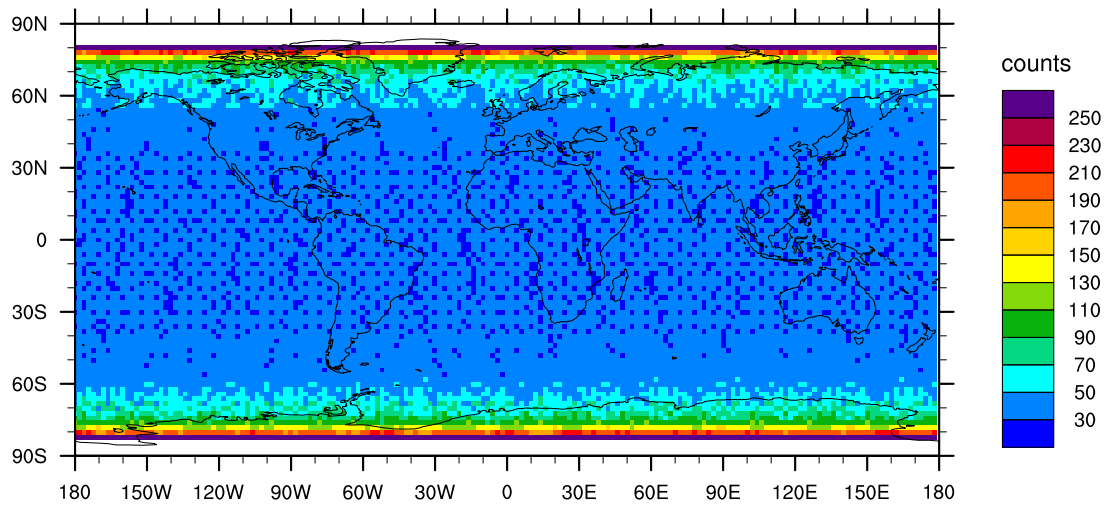


Figure 5.11: Number of satellite overpasses per grid point for July 2011.

In summary, the GME shows a clear overprediction in ice water content around 9km which is only slightly present in the heights between 10-12km and fully vanishes above. On the other hand, the GME_{ice} performs better between 8-10km and increasingly underpredicts the ice water content with increasing height. However, a meaningful conclusion can not be made when only considering the average IWCs. This is especially due to the lidar sensitivity to thicker clouds and uncertainties in the IWC product algorithm. The attention at this point should lie on the different magnitudes of IWC resulting from the altered ice microphysics. Additionally, not only the magnitude of the IWC of high clouds is important but also the frequency of occurrences. This is investigated in the next section.

5.1.2 High Cloud Frequency of Occurrence

In the following, the frequency of occurrence for the existence of clouds is investigated by use of the GME, the GME_{ice}, and the horizontally averaged 5 km layer CALIPSO IWC product. Again, the model data used is interpolated to the CALIPSO satellite track and the lidar data is interpolated on the GME model levels for better comparison. For this study the global distribution is used within a limited altitude, namely for the global model levels between 9-11 km. Also, the height dependence of IWC occurrence is investigated. Different ice water content thresholds are chosen as a criteria for the presence of a cloud and will be explicitly pointed out.

At first the global occurrence of high clouds is analysed. Therefore, the frequency of occurrence results from dividing the number of cloudy grid boxes by the satellite overpasses Fig. 5.12. The global total number of available data points, which are evaluated for all the granules of July 2011, is shown in Fig. 5.11. A grid box is defined as cloudy if the ice water content lies within the CALIPSO detection range of $0.4\text{-}100\text{ mg m}^{-3}$. The global field of occurrences for clouds between 9-11 km is depicted in Fig. 5.12. The high cloud frequencies from the GME (middle)

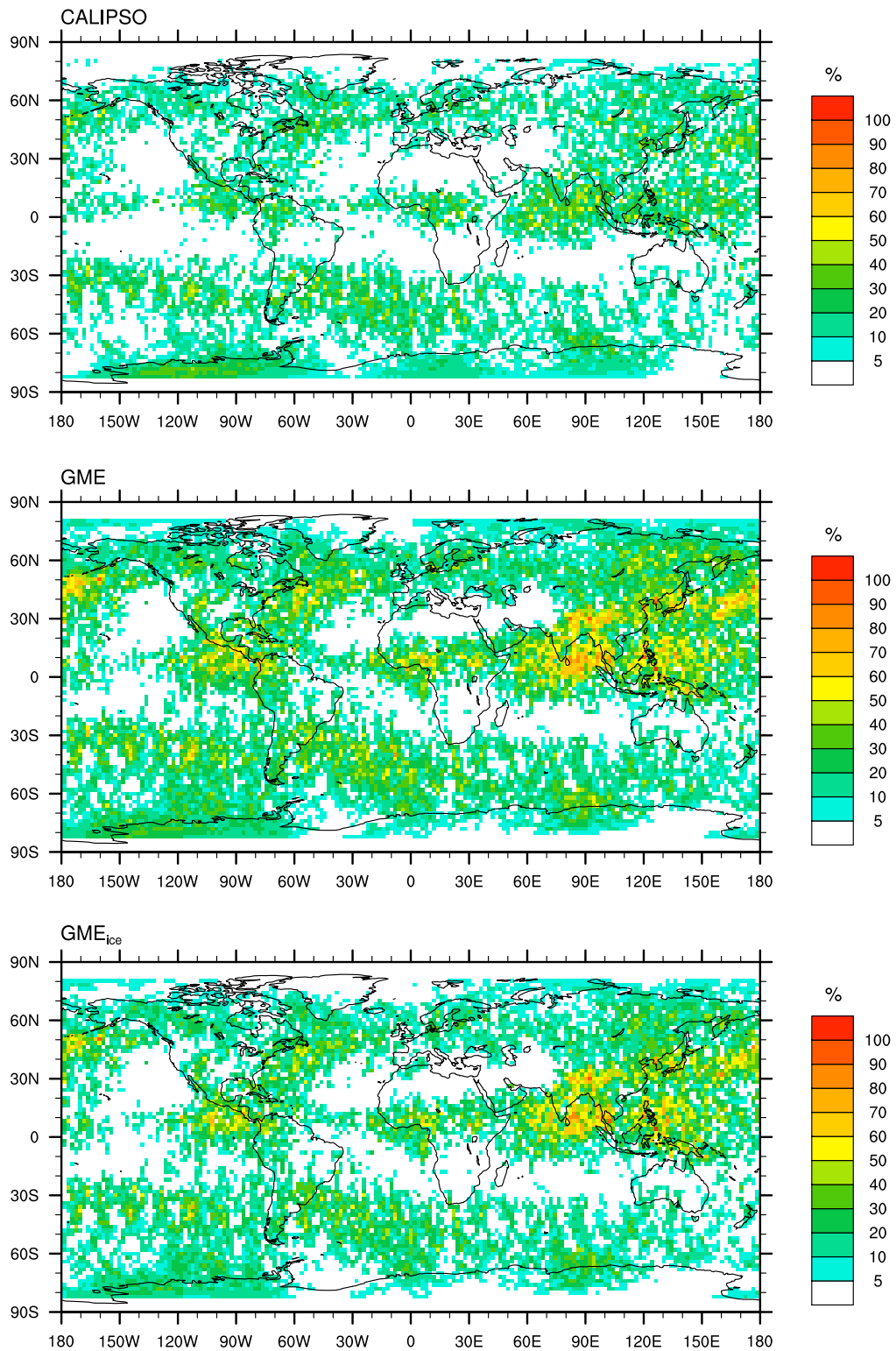


Figure 5.12: Frequency of occurrence for IWC within the CALIPSO detection range $0.4-100\text{ mg m}^{-3}$ in the upper troposphere/ lower stratosphere between 9-11 km.

and the GME_{ice} (bottom) resemble each other in structure and have peak frequencies of up to 90% cloudiness, in contrast to the frequencies of the CALIOP IWC product (top), which only reaches peak values of 40%. Also more cloud free regions are observable especially between 10-20° S. Regional distinctions between the GME and the GME_{ice} are clarified in the difference plot Fig. 5.13. The dominant red colour represents the regions of higher cloudiness frequencies in the GME compared to the GME_{ice} . Only in the tropics does the GME predict a lower frequency in IWC in some points. Thus when considering the high cloudiness occurrence, the GME_{ice} is closer to the CALIPSO data. A comparison of the GME prognostic scheme to CloudSat Cloud Profiling Radar observations by Reitter et al. (2011) show that the occurrence of high ice water paths are overpredicted with the operational microphysics, especially in the mid-latitudes.

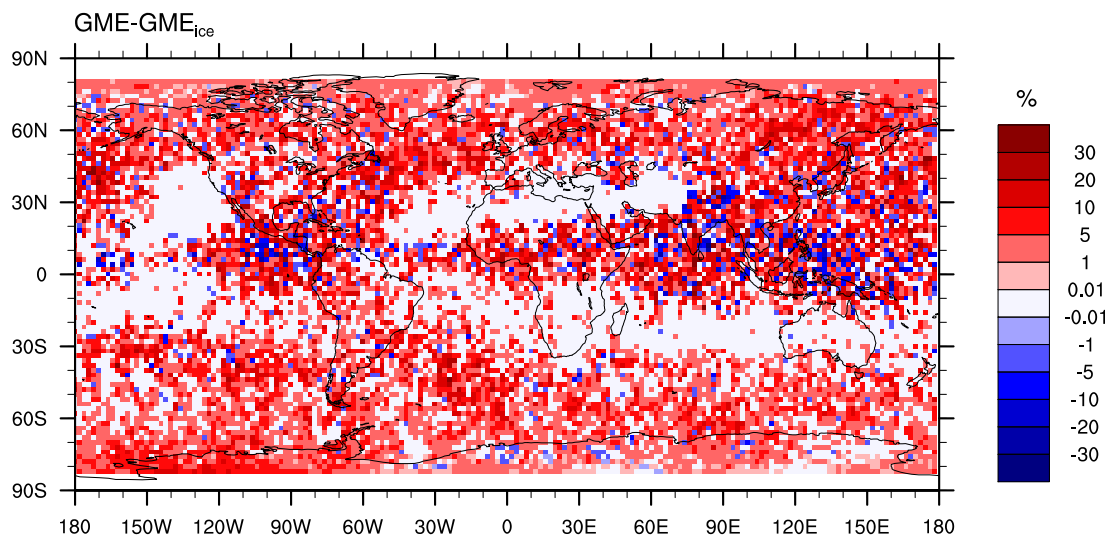


Figure 5.13: Difference in frequency of occurrence for ice water contents of $0.4-100 \text{ mg m}^{-3}$ in the upper troposphere/ lower stratosphere between 9-11 km.

The frequency of occurrence of clouds between 8 and 15 km in dependence of height and with varying IWC threshold for cloudiness is depicted in Fig. 5.14. Results in Fig. 5.14 are determined by defining the existence of a cloud to be within the CALIPSO IWC product validity range of $0.4-100 \text{ mg m}^{-3}$. In the tropics (left most plots), the maximum of the vertical profile of the frequency of occurrence of high clouds of the CALIPSO data is at 13 km and much lower for the GME models at 11.6 km. This underestimation between 12 and 15 km was already observable through the absence of clouds in the GME and the GME_{ice} in Fig. 5.9. In the mid-latitudes and polar regions (middle and right most plot of Fig. 5.9) the cloud frequencies captured by the CALIPSO are much lower beneath 10 km than the frequencies resulting from the GME and the GME_{ice} . On the one hand, increasing attenuation might be a reason for the reduced CALIPSO frequencies, while on the other hand the GME and GME_{ice} overpredict cloud occurrences in these heights. For the GME_{ice} this overprediction between 8 and 10 km is reduced by 4%. In the UTLS the CALIPSO has a higher cloud frequency than the global models. This changes when reducing the cloud threshold to 0.01 mg m^{-3} as shown in Fig. 5.14b. The global model

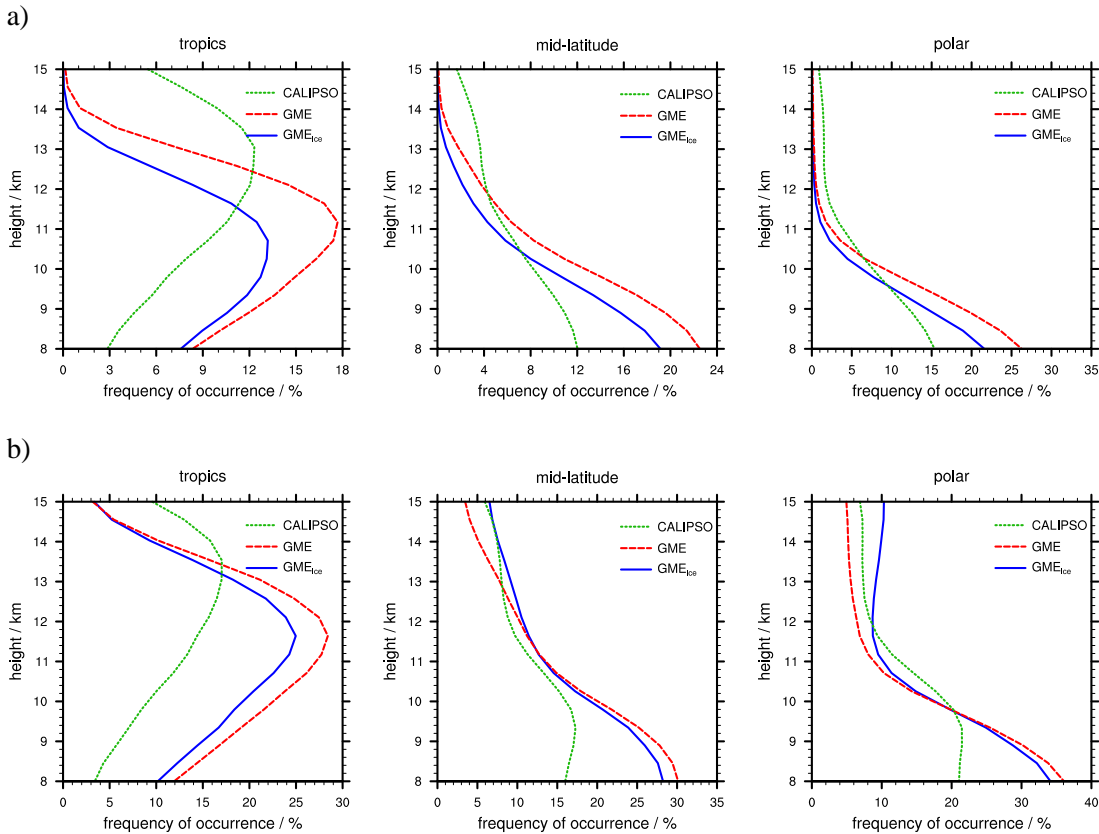


Figure 5.14: Vertical profile of the frequency of occurrence within the CALIPSO detection range $0.4\text{-}100\text{mgm}^{-3}$ (top) and for the IWC between $0.01\text{ and }100\text{mgm}^{-3}$ (bottom) with height in the upper troposphere/ lower stratosphere between 8 and 15 km .

frequencies of clouds above 10km highly increase. In the mid-latitudes and polar regions the GME_{ice} frequencies are higher than those of the GME. As a lot of the higher clouds in the GME_{ice} have smaller ice water contents, they were not captured in Fig. 5.14a. With GME_{ice} more high clouds occur, which may be a result of the introduction of the homogeneous freezing of liquid aerosols, as only heterogeneous freezing is included in the operational microphysics.

This demonstrates the high sensitivity of using thresholds for masking clouds. Questionable is to what extent the results are comparable, as the IWC derived from the CALIPSO lidar is based on a parameterisation and may be erroneous especially for great heights and strong attenuation. This makes it difficult to quantify the model errors. Yet, it can be used for indication of the overall model behaviour. As such it was remarkable that the changed ice microphysical scheme in the GME_{ice} leads to a reduction in ice water contents $0.4\text{-}100\text{mgm}^{-3}$ and ice cloud occurrence in the upper troposphere compared to the GME. In the UTLS the GME_{ice} has a higher ice cloud occurrence when it comes to small ice water contents. This is strongly correlated with the existence of ice supersaturation. How well this is captured will be the topic of the following section Sec. 5.2.

5.2 Ice Supersaturation

It is now of interest how the changes in the ice microphysical parameterization affects the relative humidity with respect to ice and the regions of its occurrence. Especially the revised parameterisation of the depositional growth is assumed to affect the behaviour of the ice supersaturation. In the operational microphysics routine, the depositional growth is calculated by use of the Euler method and a limitation of the water vapour supply for cloud ice and snow to saturation. The more physical approach is to use depositional relaxation timescales and allow for a competition for available water vapour between snow and cloud ice as stated in Eq. (4.28) earlier on.

In this section, the general occurrence of relative humidity with respect to ice is compared to the distribution law derived from Measurement of Ozone by Airbus in-service Aircraft (MOZAIC) data (Gierens et al., 1999). Further investigations of the quality of the numerical prediction model results are conducted by use of the CALIPSO Cloud Profile atmospheric data. It is derived by the Goddard Earth Observing System Model, Version 5 (GEOS-5) (Rienecker et al., 2008) and provided externally for the CALIPSO project by the Global Modelling and Assimilation Office (GMAO) Data Assimilation System (DAS). The GEOS-5 DAS integrates the GEOS-5 Atmospheric Global Climate Model (GCM) with the Gridpoint Statistical Interpolation atmospheric analysis (see <http://www.geos5.org/>). For further comparison, the relative humidity with respect to ice from the GME and GME_{ice} is compared to the ECMWF IFS model forecast data, which is the acknowledged reference for other NWP model developers. For the subsequent evaluation of the ice supersaturation, the data for the month of July 2011 will be used.

5.2.1 Ice Supersaturation Frequencies in the GME

In the following, the global occurrence of relative humidity with respect to ice is discussed. In order to understand the distribution of ice supersaturation in the atmosphere the global model data from the GME and GME_{ice} is divided for the tropics, mid-latitudes and polar regions. The relative frequencies with a further differentiation between cloud free and all model output points are plotted for the GME (Fig. 5.15a) and the GME_{ice} (Fig. 5.15b). In Fig. 5.16 it is additionally distinguished between the different temperature regimes case a: $220 < T < 243$ K and case b: $T \leq 220$ K. These different cases are then compared to a distribution law for the relative humidity in the upper troposphere/ lower stratosphere based on Gierens et al. (1999). The exponential law is derived from three years of data from the MOZAIC airborne program (Marenco et al., 1998).

First, the results of Fig. 5.15a and Fig. 5.15b for the GME and the GME_{ice} are discussed, respectively. The relative frequency distribution for the GME in Fig. 5.15a is shown for all model points and only the cloud free points, where the mixing ratios for cloud ice and cloud water are equal to zero. In the GME plots (Fig. 5.15) it can be seen that relative humidity w.r.t.

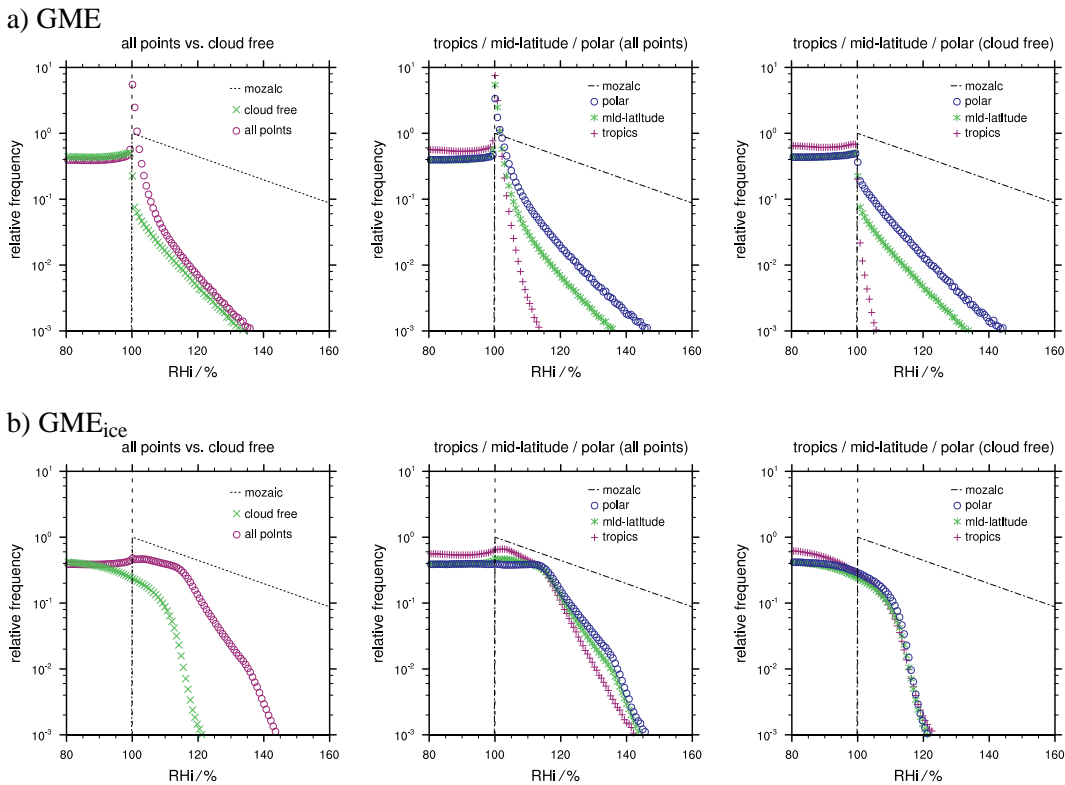


Figure 5.15: Frequency of occurrence of relative humidity w.r.t. ice in the tropics, mid-latitudes and polar regions distinguishing between cloud free and all points. For this the GME a) and the GME_{ice} b) model data for July 2011 are compared to MOZALC data.

ice frequencies denoted by a reference line at $RH_i = 100\%$ only has a peak when considering all points. The mentioned peak will be removed, once the cloud clearing is performed. This shows that for the operational ice microphysics scheme a lot of the in-cloud relative humidity is equal to ice saturation. The ice supersaturation distribution exponentially decreases with increasing humidities. When looking at the different geographic regions, the distribution for all points in Fig. 5.15a shows that most of the ice supersaturation occurs in the polar regions and the least in the tropics. This looks similar when looking at the cloud free points for the polar and mid-latitudes, which are slightly reduced. However, the frequency of ice supersaturation in the tropics is small, which indicates that most of the ice supersaturation in the tropics exist within clouds in the GME. The high relative frequencies described by the MOZALC exponential law are not reached even though high supersaturations are present.

The RH_i distribution for the GME_{ice} Fig. 5.15b looks very different for the comparison between all points and only the cloud free points. The distribution considering all points is almost parallel to the MOZALC distribution until reaching 120% . After that the relative frequency drops steeply and bulging at $RH_i = 140\%$. Thus a break in the distribution can be observed for the GME_{ice} . This might be a consequence of the two nucleation mechanism being triggered at these humidities. This is further discussed later in combination with the temperature dependencies. When regarding the relative frequencies in dependency of the tropics, mid-latitudes

and polar regions in Fig. 5.15b, the differences are not that obvious. A main difference to the GME relative frequency of RHi lies in the location of the maximum, which is near a relative frequency of 120% for the polar region and is shifted further to saturation in the tropics. When looking at the cloud free scenario in Fig. 5.15b it is quite surprising that the ice supersaturation values are reduced so severely. Responsible for this might be the process of sedimentation as it plays a crucial role in maintaining in-cloud ice supersaturation (Spichtinger and Gierens, 2009a). This finding of in-cloud supersaturation is also in accordance with Spichtinger and Gierens (2004) who investigated this phenomenon through statistical evaluations of MOZAIC and INCA measurements. They argue that the shape of the humidity distribution differ in dependency of the maturity of the cloud. The cirrus clouds warmer than -40°C are considered to be more mature and have a more symmetric distribution, while it is positively skewed in colder cirrus (Spichtinger and Gierens, 2004). Thus it is important to investigate the different temperature regimes in which the high relative humidities occur.

The temperature dependency of the ice supersaturation frequency is important to investigate due to the nucleation regimes and is depicted in Fig. 5.16. Heterogeneous nucleation occurs at temperatures above $\sim 220\text{K}$ and RHi around $\sim 120\%$ while homogeneous freezing of liquid aerosols happens at colder temperatures and higher ice supersaturations. Thus differences in the RHi distribution are expected in relation to the different nucleation regimes. The temperature ranges that are considered for the GME (Fig. 5.16a) and the GME_{ice} (Fig. 5.16b) are $220 < T < 243\text{K}$ and $T \leq 220\text{K}$, where heterogeneous and homogeneous nucleation are active, if sufficient ice nuclei and ice supersaturation are existent.

Looking at Fig. 5.16a for the GME model output reveals that the relative humidities over ice peak at ice saturation for both temperature intervals. Case a shows maximum relative humidities with respect to ice of 110%, whereas the colder case b includes the higher values. It is interesting to see that the ice supersaturation seems to be quite insensitive towards the temperature in the tropical region. In the other regions the RHi values are much higher which would be expected in colder regions.

When regarding the relative frequency plots in Fig. 5.16b the observed behaviour for case a is analogue to the findings in Lamquin et al. (2012) for relative humidities over ice for $T < 243\text{K}$. For very cold temperatures below 200K with high level cirrus there is a shift in the RHi peak. This peak at 120% for high clouds can also be seen in Fig. 4 in Lamquin et al. (2012), where the RHi field is plotted for the northern mid-latitudes MOZAIC data. This bulge in the RHi distribution in the MOZAIC data at 120% for high cirrus is also discussed in Spichtinger and Gierens (2004). Therein it is also argued that for thin high cirrus clouds the depletion of supersaturation through depositional growth is very slow. This behaviour is also observable in the relative frequency plot Fig. 5.16b with the new microphysical scheme including the altered depositional growth.

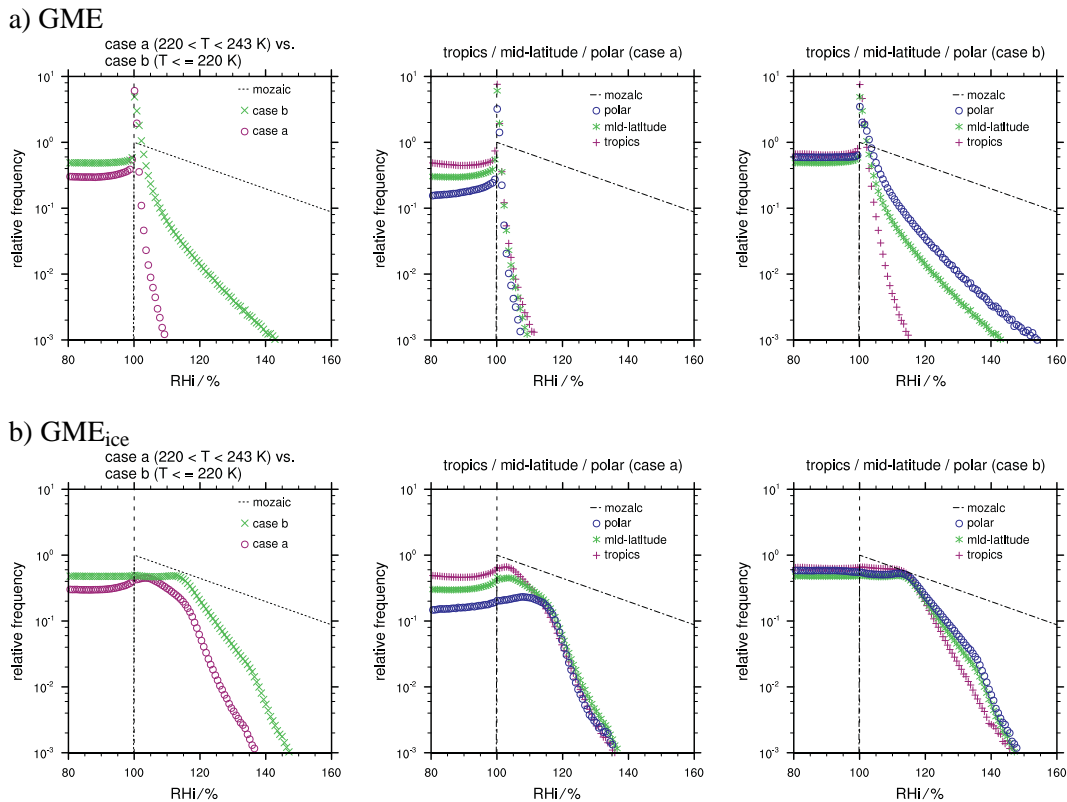


Figure 5.16: Frequency of occurrence of relative humidity w.r.t. ice in the tropics, mid-latitudes and polar regions as in Fig. 5.15 but now with distinguishing between the temperature regions $220 < T < 243$ K and $T \leq 220$ K. The GME (top) and the GME_{ice} (bottom) model data for July 2011 are compared to MOZAIC data.

5.2.2 Comparison to CALIPSO GEOS-5 atmospheric data

To assess the quality of the relative humidity over ice of the GME and the GME_{ice} it is compared to the atmospheric data which is supplied along with the CALIPSO track data from the GEOS-5 Earth System Modelling and Data Assimilation System. The synoptic and time averaged GEOS-5 data is given for the midpoint of each point in the CALIPSO Level 2 profile. Thus the spatial resolution remains the same as for the CALIPSO IWC product, i.e. vertically 60 m and horizontally averaged over 5 km for data between 8.2-20.2 km.

The cloud physics scheme of the GEOS-5 Atmospheric General Circulation Model accounts for convection and large-scale condensation distinguishing between liquid and ice phase condensates (Rienecker et al., 2008). In the moist physics routine, the convection parameterisation is the Relaxed Arakawa-Schubert scheme (Moorthi and Suarez, 1992) and called first. The emerging detraining mass and condensate fluxes are included in the subsequently called large-scale cloud scheme. It states in the documentation from Rienecker et al. (2008) that the condensation process is based on a boxcar probability distribution function with a bi-modal structure with the spread being determined by local saturation humidity. Once condensates exist, the processes of evaporation, autoconversion, accretion and sedimentation determine the further development.

The relative humidity provided as CALIPSO atmospheric data from the GEOS-5 is a mixed phase RH. Following the description of Putman (pers. communication 2013) this means that for $T < 233.16\text{K}$ the RH model output is RH over ice only. Between $233.16\text{K} < T < 273.16\text{K}$ RH is over a mixture of water and ice with a linear interpolation between 273.16K and 233.16K and for temperatures below 273.16K the relative humidity is over water only. Thus the water vapour mixing ratio at saturation is

$$q_{v,s} = \begin{cases} q_{v,sw}, & \text{if } T \geq T_0 \\ q_{v,sw} + (q_{v,si} - q_{v,sw}) \frac{(T - T_0)}{(T_1 - T_0)} & \text{if } T_0 < T < T_1 \\ q_{v,si}, & \text{if } T \leq T_1 \end{cases} \quad (5.2)$$

with $T_1 = 233\text{K}$ and $T_0 = 273\text{K}$. The water vapour mixing ratio can be calculated using $q_v = RH q_{v,s}$ and inserted into $RHi = q_v/q_{v,si}$ yields

$$RHi = RH \left(q_{v,sw} + (q_{v,si} - q_{v,sw}) \frac{(T - T_0)}{(T_1 - T_0)} \right) \frac{1}{q_{v,si}}. \quad (5.3)$$

The relative humidity with respect to ice from GEOS-5 data is calculated using Eq. (5.3) and is now compared to RHi from the GME and the GME_{ice} for July 2011. As done in Sec. 5.1.2 for the CALIPSO ice water content profile data, the GEOS-5 data is interpolated to the GME model heights. The GME and GME_{ice} data is interpolated onto the CALIPSO track. In Fig. 5.17 the frequency of occurrence for relative humidities with respect to ice above 100% between 9-11 km is shown. The frequency is normalised by the satellite passings depicted in Fig. 5.11. On the first glance, the GME (middle plot) and GME_{ice} (bottom plot) have the same structures and frequencies. Yet deviations in the latter are perceivable in the difference plot shown in

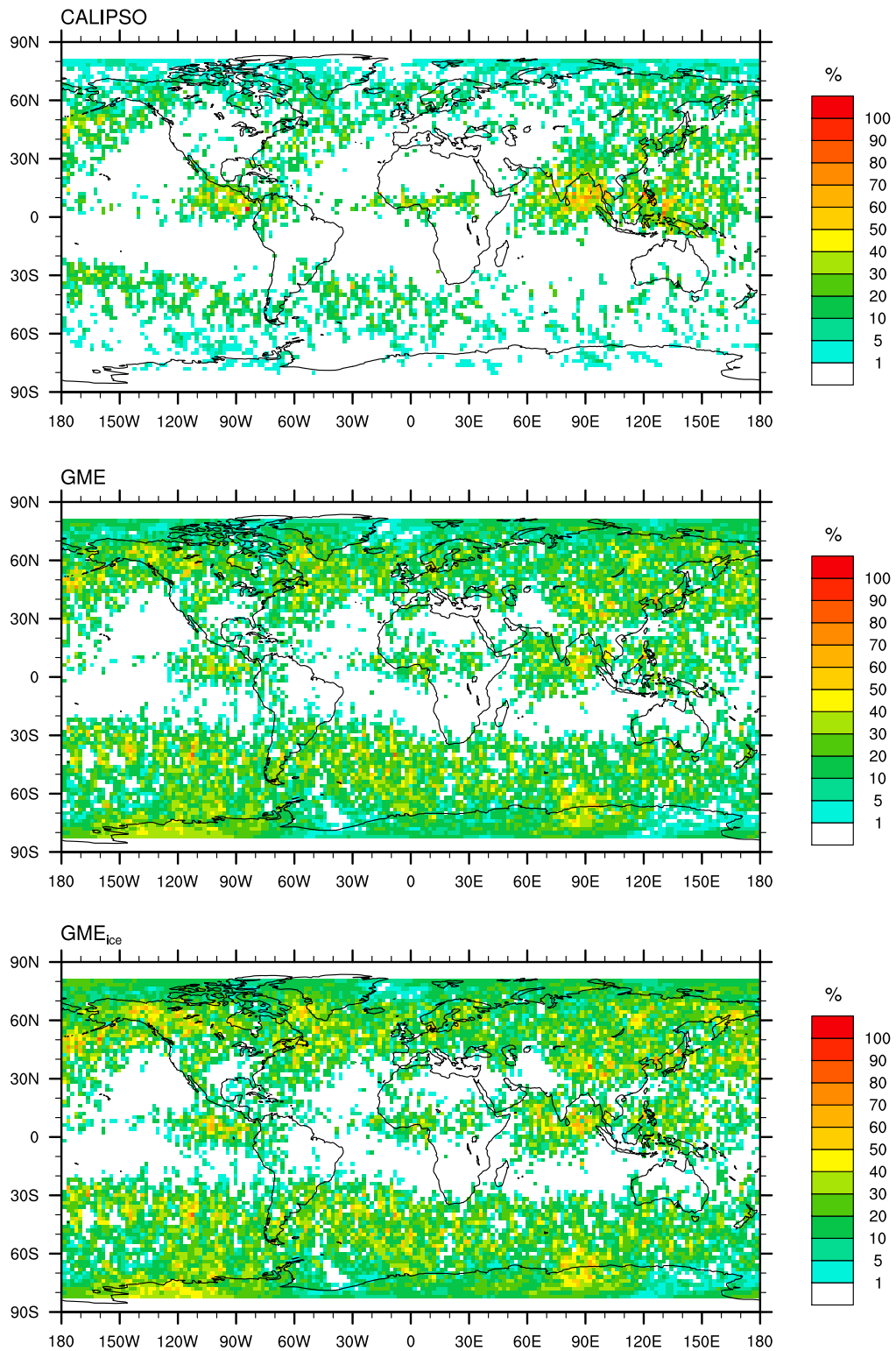


Figure 5.17: Frequency of occurrence for $RH_i > 100\%$ in the upper troposphere/ lower stratosphere between 9-11 km.

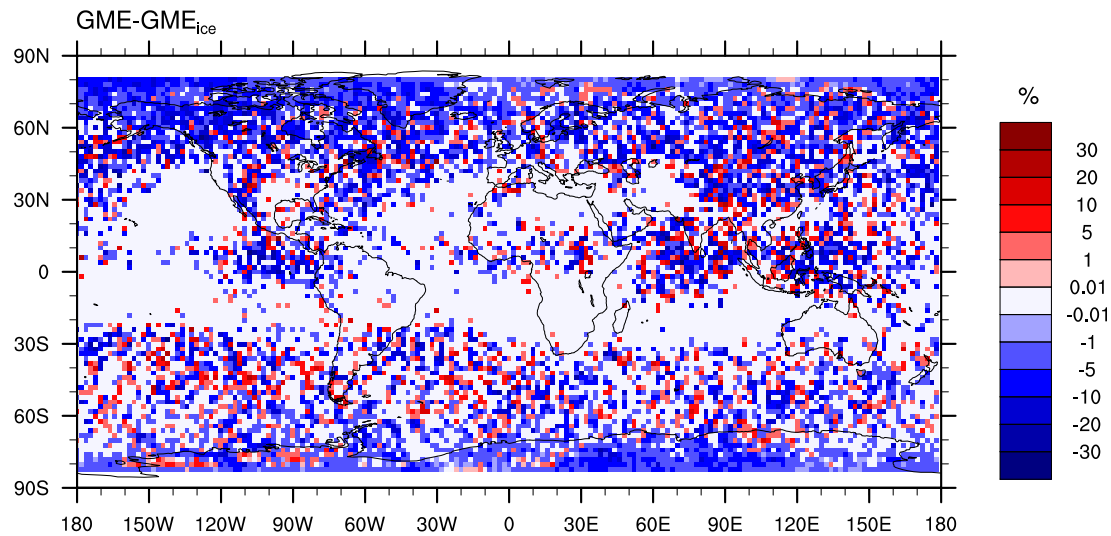


Figure 5.18: Difference in frequency of occurrence for $RH_i > 100\%$ of the GME and GME_{ice} between 9-11 km.

Fig. 5.18. The blue colour being dominant indicates the higher frequency of ice supersaturation in the GME_{ice} especially in the polar regions. This higher frequency in the GME_{ice} is expected, as the relaxation timescale approach for the depositional growth in the new cloud ice scheme causes a slower depletion of ice supersaturation.

The CALIPSO atmospheric data (Fig. 5.17 top plot) has much lower frequencies of $RH_i > 100\%$ in comparison to the GME and the GME_{ice} plots in the mid-latitudes and polar region. In the tropics the frequencies look similar and peak frequencies of 75% of $RH_i > 100\%$ can be found. In Read et al. (2007) the humidity GEOS-5 analyses is compared to the Aura Microwave Limb Sounder (MLS) H_2O for pressures between 316-83 hPa. The result of this study is that the GEOS-5 is more humid than the MLS (version 2.2) data for all levels regarded. In Read et al. (2007) the MLS RH_i is also compared against AIRS RH_i data. It is discussed that the MLS probability density function has a longer tail into supersaturation in comparison to the AIRS data (see Fig. 20 in Read et al. (2007)) due to a fractional radiance error. Thus the low GEOS-5 $RH_i > 100\%$ frequency is even more surprising, however the MLS RH_i versus GEOS-5 RH_i was not specifically looked at according to Read, pers. communication 2013. This makes the result quite questionable. To assess the quality of the GME and the GME_{ice} RH_i frequencies, further reference data is needed. Therefore data from the ECMWF is used for comparison in the next section.

5.2.3 Comparison to IFS data

In the following, the relative humidity with respect to ice from the GME and the GME_{ice} are compared to ECMWF IFS data (see <http://www.ecmwf.int/research/ifsdocs/CY37r2/>). For this purpose, the global model forecasts for the IFS, the GME and the GME_{ice} are used from 00-24 h

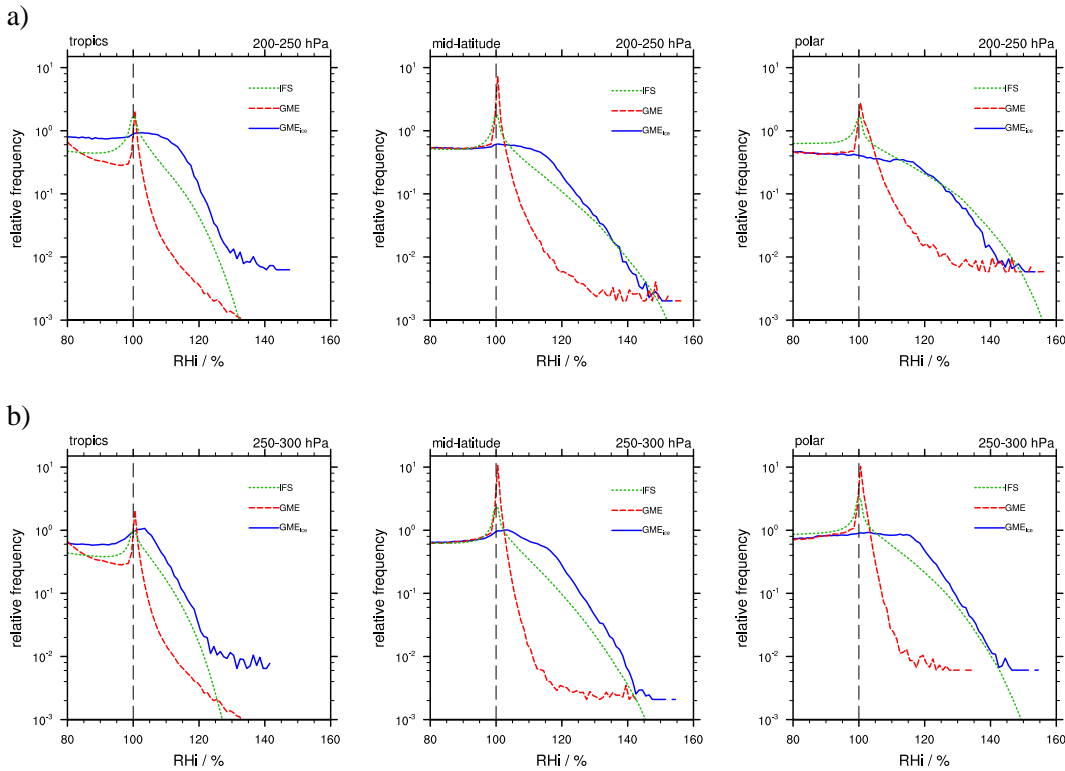


Figure 5.19: Frequency of occurrence of relative humidity w.r.t. ice in the tropics, mid-latitudes and polar regions where the temperature is below 250.16 K. The GME and the GME_{ice} model data for July 2011 are compared to IFS data. The top plots show the evaluation for the pressure levels 200-250hPa and the lower plots show the *RHi* between 250 and 300hPa.

for July 2011 every 3h. The operational IFS forecasts are on seven pressure levels namely 500, 400, 300, 250, 200, 150 and 100hPa. The used IFS data has a resolution of ≈ 16 km on the reduced gaussian grid N640 with 2560x1280 grid points.

The IFS model physics comprises prognostic equations for rain, snow, cloud liquid water, cloud ice and a grid box fractional cloud cover for the cloud and large-scale processes further described in ECMWF (2011). For stratiform and convective clouds the prognostic cloud scheme by Tiedtke (1993) is implemented in the IFS. The model physics also accounts for homogeneous and heterogeneous ice nucleation, with the latter being based on the diagnostic formulation of Meyers et al. (1992). Homogeneous nucleation is triggered at a local critical relative humidity as defined in Kärcher and Lohmann (2002), and similar to Eq. (3.8) of the presented approach. Ice nucleation is also initiated if the grid-mean reaches a lower threshold, which additionally depends on the ratio $q_{v,sw}/q_{v,si}$ for the nucleation of liquid water droplets. Existing ice crystals deplete ice supersaturation within the model time-step (for a detailed description see Tompkins et al. (2007)). This consequently leads to ice supersaturation only in cloud-free regions.

The relative humidity diagnostic in the IFS accounts for the liquid phase, the mixed phase and the ice phase. The model output relative humidity is defined by the vapour pressure e_v and

the saturation vapour pressure $e_s = \alpha e_{sw} + (1 - \alpha)e_{si}$ (Forbes, pers. communication 2013) as $RH = e_v/e_s$. The saturation vapour pressure over water (e_{sw}) and ice (e_{si}) are calculated as documented in ECMWF (2011) and α is the mixed-phase diagnostic function that ranges from $\alpha = 1$ at 273.16K to $\alpha = 0$ at 250.16K. Thus for $T > 273.16$ K, the RH diagnostic is w.r.t. water and below 250.16K it is w.r.t. ice, while in between it is mixed phase.

The relative frequency for RHi for the pressure levels 200-250hPa and 250-300hPa is depicted in Fig. 5.19a and Fig. 5.19b, respectively. The model behaviour is similar for both pressure intervals. The GME (dashed red) and the IFS (dotted green) both have a peak at ice saturation. This originates from in-cloud saturation. By definition the IFS does not allow for in-cloud ice supersaturation as previously discussed (see also Sec. 3.2 and Fig. 3.1). This peak at $RHi = 100\%$ does not exist in the GME_{ice} (solid blue) model output because of the change in depositional growth in the new cloud ice scheme. The curve of the relative frequency of relative humidity with respect to ice of the GME is of a rather convex nature after the peak. The RHi curves of the IFS and the GME_{ice} both show a concave behaviour for $RHi > 100\%$ agreeing especially in the mid-latitudes and polar regions. This shows that especially the frequencies for higher ice supersaturations are captured well with the altered depositional growth. The influence of homogeneous nucleation of liquid aerosols might also contribute to this behaviour. While the IFS and the GME_{ice} account for this process occurring at $RHi \approx 150\%$, it is not implemented in the GME physics at the present.

The evaluation of the global frequency of occurrence of $RHi > 100\%$ is shown in Fig. 5.20. The data is normalised by the amount of grid points. For better comparison GME and GME_{ice} data between 100 and 500hPa and with temperatures below $T < 250.16$ K is used for comparison. The top plot in Fig. 5.20 shows the frequencies of ice supersaturation in the IFS, the middle plot for the GME and the bottom plot for the GME_{ice}. The overall structures and peak frequencies are in accordance with each other. However, the frequencies in the IFS are lower than expected due to the lack of in-cloud ice supersaturations. This is especially visible in the mid-latitude storm tracks between 30°C and 50°C. When comparing the GME and the GME_{ice}, the GME_{ice} locally has higher frequencies, which is in accordance to Fig. 5.18. The result for the higher threshold for RHi occurrence of 120% is shown in Fig. 5.21. Only the southern polar region of the GME have non-vanishing frequencies. The IFS and the GME_{ice} still have wider areas with frequencies of $RHi > 120\%$ occurrence of around 5%, especially in the tropics and southern hemisphere.

5.2.4 Ice Supersaturated Regions

The characteristics of ice supersaturated regions (ISSRs) have been described in Sec. 2.3. In question is how well these regions are represented in the GME and GME_{ice}. Investigated is the global distribution of ISSRs and their vertical layer thickness. The interpolated data on the CALIPSO track from the GME and the GME_{ice} and their time and spatial means of the relative humidity with respect to ice and the ice water content is used. Only data is considered where

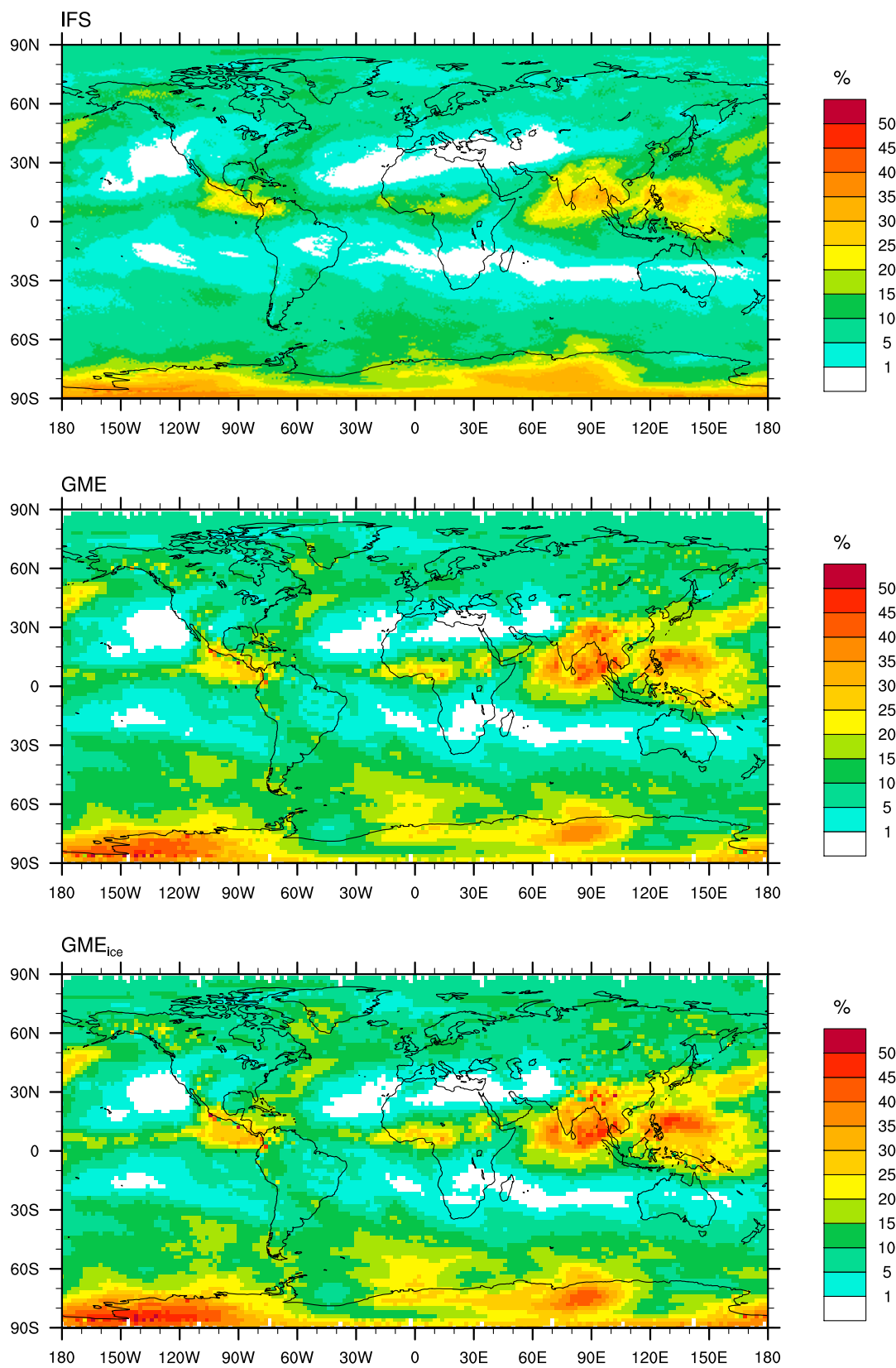


Figure 5.20: Frequency of occurrence of $RH_i > 100\%$ in the upper troposphere/lower stratosphere between 100-500 hPa and $T < 250.16\text{ K}$ for July 2011.

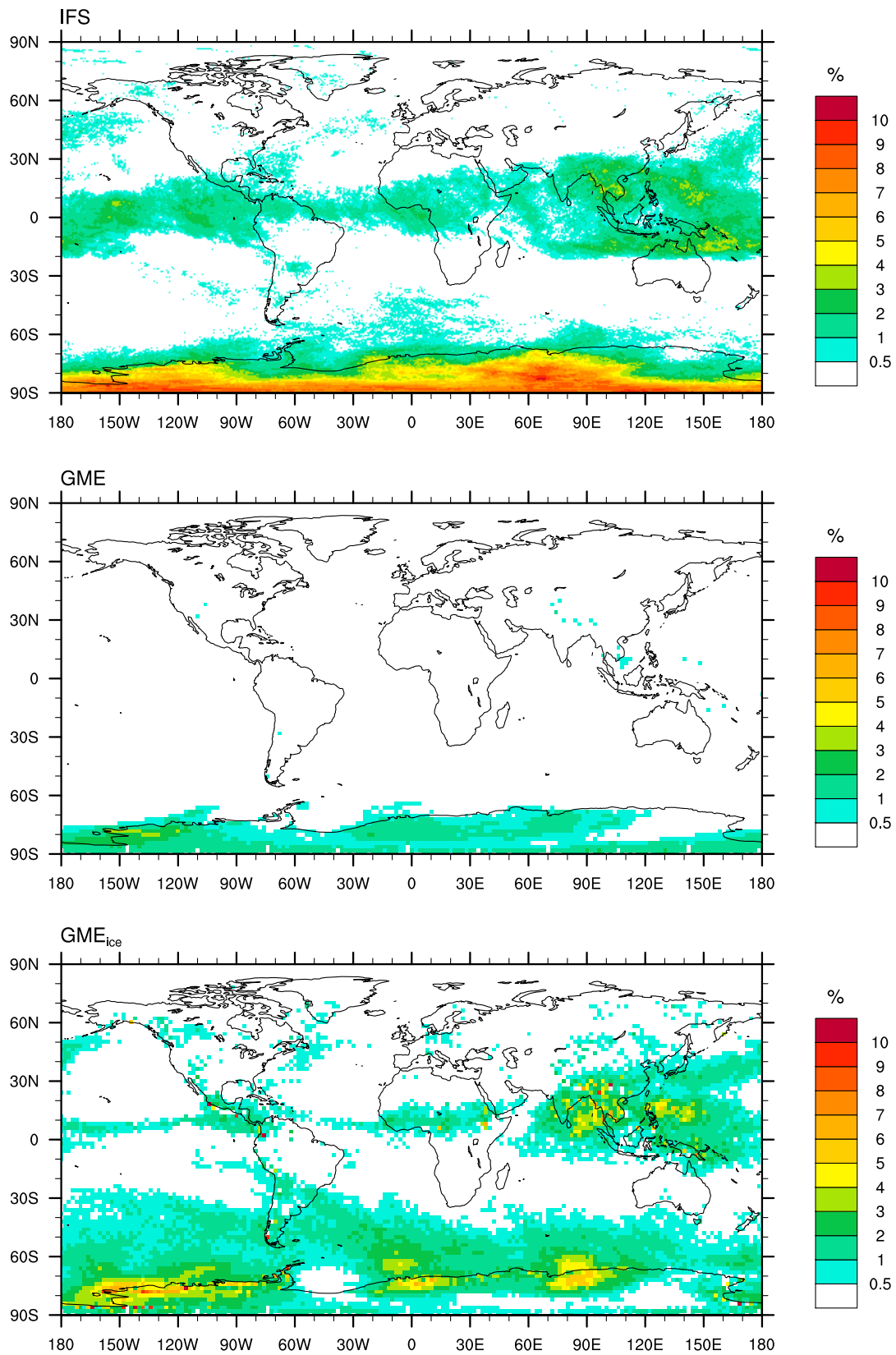


Figure 5.21: Frequency of occurrence of $RH_i > 120\%$ in the upper troposphere/lower stratosphere between 100-500hPa and $T < 250.16\text{K}$ for July 2011. Attention has to be paid to the different colour scale in comparison to Fig. 5.20.

the $RHi > 100\%$ and the ice water content is less than 1 mg m^{-3} . This is done as proposed in Lynch (2002) as ice supersaturated regions are defined as a cloud free air mass.

The resulting global field of the vertical layer thickness is plotted in Fig. 5.22 for the GME (top) and the GME_{ice} (bottom). The GME plot in Fig. 5.22 shows a general lack of global ISSRs. While the ISSRs in the tropics and northern polar regions are rather patchy and the thickness lies beneath 4km, there is a maximum in the southern polar region of 8km which seems extremely thick. In contrast, the overall ISSRs thicknesses for the GME_{ice} in Fig. 5.22 (bottom) lie beneath 2km with a maximum between 2-4km in the southern polar region.

The corresponding global mean values for the ISSRs thickness as calculated from the GME data is 2.25km and for the GME_{ice} 1.32km. This is in accordance with the findings of Spichtinger et al. (2003a) who give the mean vertical extension of ISSRs of 1-2km. This leads to the conclusion that the GME slightly overpredicts the thickness of these regions, which is probably mainly due to the large values in the southern polar region. Also the vertical global model resolution in the upper troposphere of about 1 km and larger could be a possible reason.

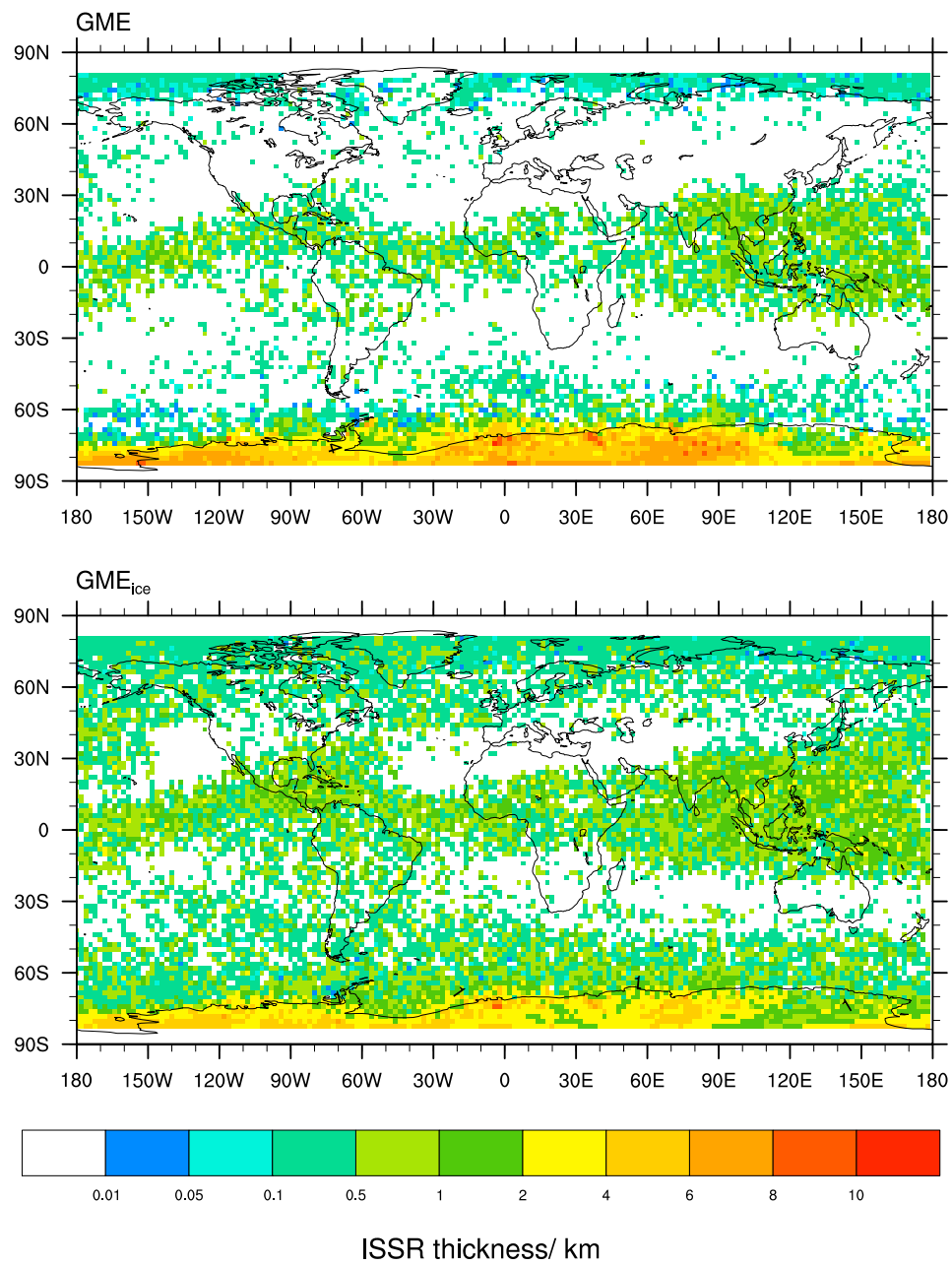


Figure 5.22: The vertical layer thickness of ice supersaturated regions in the GME (top) and the GME_{ice} (bottom).

Chapter 6

Discussion of Results

The principal aim of this work was to identify the controlling processes of cloud ice particle and ice supersaturation formation and represent these processes in a physical way in the DWD model chain. In order to accomplish this goal, a new cloud ice scheme was developed and tested within different model environments. The parcel model, the idealised COSMO model setup, the regional COSMO-DE, and the global GME were used in order to gain a better comprehension of the behaviour of the new ice microphysics scheme.

For developing the new ice cloud scheme, state-of-the-art parameterisations were compared to existing formulations used in the DWD numerical weather prediction models and shortcomings were detected. In this context, the cloud ice nucleation parameterisations for the heterogeneous nucleation and the depositional growth were investigated. Important microphysical processes which were not represented previously in the DWD NWP models are the homogeneous nucleation of liquid aerosols, an ice nuclei budget variable for heterogeneously nucleated ice crystals and cloud ice sedimentation. Which of these processes are most important for cirrus and ice supersaturation development are discussed in the following. Presented are the results of satellite data comparisons to the regional COSMO model and global GME with the new cloud ice scheme, COSMO_{ice} and GME_{ice}, respectively. The use of different model resolutions allows for a scale dependent interpretation of cirrus formation within NWP models. A study for July 2011 of the GME and GME_{ice} along with a verification with CALIPSO lidar data helped to assess the results with regard to the ice water content. The quality of the modelled ice supersaturation of the GME_{ice} was compared to the GME, the IFS and the CALIPSO/GEOS data. In this context the strengths and weaknesses of the new scheme for further applications are elaborated.

6.1 Summary of Results

A parcel model was used to investigate the difference of the homogeneous and heterogeneous nucleation parameterisations, their competition and their influence on ice crystal number den-

sity, ice particle radius, cloud ice mixing ratio and ice supersaturation. Results depicted in Fig. 3.5 show that the choice of the parameterisations for the homogeneous and heterogeneous nucleation modes have the greatest impact on microphysical properties for young cirrus and ice supersaturation. For young cirrus, the cloud ice mixing ratio resulting from the new cloud ice scheme, including homogeneous and heterogeneous freezing, is lower than the cloud ice mixing ratio resulting from the operational cloud ice scheme using heterogeneous nucleation only. For older cirrus which developed through a constant uplifting, the air parcel reaches a quasi-steady state and the cloud ice mixing ratio for both cloud ice schemes converge to saturation (see Fig. 3.5d). Moreover, the importance of including the homogeneous nucleation in the ice nucleation scheme is stressed when regarding the associated ice supersaturation ratios (see Fig. 3.5a). The ice supersaturation ratio only reaches values below 1.2 ($RH_i = 120\%$) when solely using the heterogeneous nucleation scheme from the operational scheme of the DWD NWP models for the parcel model simulations. The values of the ice supersaturation ratio reaches values over 1.45 ($RH_i = 145\%$) when applying the new cloud ice scheme which includes homogeneous freezing based on Kärcher et al. (2006) including the competition of the two nucleation modes.

Idealised model runs in the COSMO model environment of orographic cirrus were conducted in order to investigate the effect of each model change on the cirrus cloud structure. Emphasised were the introduction of the prognostic tracking variable for activated ice nuclei and cloud ice sedimentation. Both were shown to alter the spatial structure and reduce heterogeneously nucleated ice. Whereas the ice nuclei budget variable limits heterogeneous cloud ice production and changes the inner cloud ice crystal distribution, the cloud ice sedimentation especially reduces heterogeneous cloud ice, as heterogeneous cloud ice particles are bigger than homogeneously nucleated ice crystals, and has a stronger impact on the vertical structure. The limitation and reduction of heterogeneous nucleation both cause less supersaturation to be depleted and thus subsequent homogeneous nucleation has a higher chance of being triggered if sufficiently high cooling rates exist. Under which circumstances either the homogeneous or heterogeneous nucleation dominates cirrus cloud formation is highlighted in the parameter study for orographic clouds. In this study the mountain height, where higher mountains cause stronger orographic waves with correlated cooling rates, and the amount of atmospheric aerosol number density were varied. Homogeneous nucleation dominates in scenarios with strong orographic forcing and low ice nuclei whereas heterogeneous nucleation controls cirrus formation in regimes with low mountain heights and high numbers of ice nuclei. Excluding the tracking variable and/or the cloud ice sedimentation causes a severe increase in heterogeneously nucleated cloud ice even for regimes with high vertical velocities, as can be seen in the parameter space plots in Fig. 4.6. To include the ice nuclei budget variable and cloud ice sedimentation are thus necessary in order to prevent an overestimation of heterogeneous nucleated cloud ice. Also, the parameter study demonstrates the substantial dependence of homogeneous freezing on high vertical velocities.

A case study of the 26th of August 2011 using the COSMO-DE with a resolution of 1.7km was conducted using the operational cloud ice microphysics scheme and the new two-moment

cloud ice microphysics scheme. Comparing the modelled ice supersaturation fields shows a significant difference between the COSMO and COSMO_{ice} model. The relative humidities with respect to ice from the operational cloud ice scheme reach values between 110% and 120% while $RHi \approx 140\%$ when using the new cloud ice scheme. This finding of differing values for RHi is consistent with the observations made in the parcel model runs and is due to the missing of the homogeneous nucleation mode. Furthermore, comparisons of the high cloud cover with MSG SEVIRI cloud classification data show that the new cloud ice scheme is capable of predicting semi-transparent clouds (high cloud cover $\approx 50\%$) whereas the operational cloud ice scheme tends to overpredict the high cloud cover with sustainable values between 90% and 100% (see Fig. 4.13).

For July 2011, an evaluation for the ice water content, high cloud occurrence and ice supersaturation of the GME_{ice} was performed. The IWC and high cloud occurrence of the operational and new two-moment cloud ice scheme were compared with the CALIPSO lidar ice water content product. The GME_{ice} greatly reduces the RMSE for all longitudes and latitudes for the heights between 8-15km except in the tropics, where the GME with the operational microphysics scheme performs slightly better (see Fig. 5.6). However, the tropics are not representative for the evaluation, as the sub-grid scale mixing ratios for cloud ice and snow are not considered in this work and shortcomings of the convection parameterisation dominate. In comparison to the CALIPSO data, the GME overpredicts the IWC in 9km, whereas the GME_{ice} shows good agreements with the CALIPSO data for 8-10km but increasingly underpredicts the IWC with increasing height. Also the GME_{ice} shows a reduction in high cloud occurrence which is an improvement against the GME between 9-11 km when compared to the CALIPSO data, as shown in Fig. 5.12. The high cloud frequency from the GME_{ice} is dependent on the considered IWC range. For the IWC range 0.4-100mg m⁻³ the reduction in high cloud frequency above ≈ 10 km is too high, while including smaller IWCs between 0.01 and 100mg m⁻³ cause an increase in high ice cloud occurrence in comparison to the GME and are in accordance with the CALIPSO data in the mid-latitudes Fig. 5.14. Regarding ice supersaturation, clear improvements were observed when comparing the GME_{ice} to the IFS. The slopes of the frequency of occurrence for high ice supersaturation values between 200hPa and 300hPa are compliant for the IFS and GME_{ice}, while the GME does not capture them (see Fig. 5.19). Additionally, in-cloud supersaturation is allowed for through the application of the altered depositional growth in the GME_{ice}, which is not allowed for in the IFS but is in accordance with in-situ measurements (discussed in Sec. 6.2.2).

6.2 Interpretation of Results

The results of this work are now interpreted with respect to their influence on cloud ice, ice supersaturation and their dependency on the model resolution.

6.2.1 Cloud ice

The main physical processes for cirrus formation are homogeneous and heterogeneous nucleation. The latter depends on available atmospheric aerosol, while for triggering homogeneous nucleation vertical velocity fluctuations are required. Cloud ice sedimentation and depositional growth were identified as further controlling cirrus cloud development. For a physical representation in the NWP models of the DWD, state-of-the-art parameterisations were tested and implemented providing a new two-moment cloud ice scheme.

The inclusion of homogeneous nucleation of liquid phase aerosols as a separate process is essential for correctly modelling cloud cirrus due to the correlated high ice supersaturation ratios and high ice crystal concentrations. However, in order to reproduce observed high ice crystal number densities with NWP models, sub-grid scale vertical velocities are needed especially in global models (e.g., Kärcher and Lohmann (2002), Hoyle et al. (2005)). In order to counteract this deficit in regional models, a simple relation using the turbulent kinetic energy was used in the COSMO model (see Sec. 4.3.1). The prevailing shortcoming of sufficient fluctuations in the vertical velocity was highlighted by the comparison of ice crystal number densities of idealised simulations in the COSMO model environment to measurements from the INCA campaign (Sec. 4.4.1), where an offset of the ice crystal number densities to lower values was observed. For the global model, the *TKE* could not be used and instead an additional sub-grid scale orography induced velocity was implemented following Joos et al. (2008), as shown in Sec. 4.3.2. However, further enhanced mesoscale fluctuations in the global model are still required, as peak ice crystal number densities could not be attained with this approach. Another formulation of the vertical velocity for the global model is derived in Sec. 6.2.3, which uses the correlation between the high resolution model updrafts from the COSMO-DE and their average over the GME model resolution. Only if vertical velocities above 20 cm s^{-1} are reached and a low amount of ice nuclei exist in the atmosphere, ice supersaturation reaches high enough values to trigger homogeneous nucleation (e.g., Khvorostyanov and Sassen (2002), Gierens et al. (2003)).

The operational heterogeneous nucleation model parameterisation is only temperature dependent, while the new parameterisation based on Phillips et al. (2008) also takes the ice supersaturation and the aerosol species dust, soot and organic substances into account. A fixed number density for the three classes of ice nuclei is given, which makes it important to include a heterogeneous nucleation dependent variation to limit the amount of available IN. The limitation is included in the NWP models by the implementation of a prognostic tracking variable for activated aerosol. Previously activated ice nuclei are thus accounted for and are subject for freezing again, depending on a mixing timescale. The mixing timescale is set to two hours throughout the course of this study, which means that previously nucleated ice nuclei are available for heterogeneous nucleation again after this time. The mixing timescale is a sensitive tuning parameter to increase or decrease heterogeneous nucleation by reducing or increasing the mixing time interval, respectively. The prognostic IN budget variable is thought to be an intermediate solution between the constant IN field and prognostic aerosols being directly nucleated, which

is not feasible for operational NWP model use due to computational limitations. An attempt at a more physical approach based on an IN budget variable was thus undertaken which reduces the risk of overpredicting available IN in the NWP model. Another possible tuning parameter for the heterogeneous nucleation parameterisation is the amount of initial aerosol available, which can be altered as a whole with a scaling factor or a height dependent ice nuclei distribution could be introduced, derived by fitting the resulting model ice water content to observations (see Fig. 5.14). Also possible is to change single IN concentrations for carbon, soot and organic substances individually, as they have different nucleation characteristics. Yet, there are still a lot of uncertainties concerning heterogeneous nucleation and the nucleation characteristics for each IN species (DeMott et al., 2011). In Phillips et al. (2013) a revised version of the applied heterogeneous ice nucleation scheme is presented. Introduced are new properties for black carbon, insoluble organic aerosols are replaced by primary biological particles, and a fourth group of ice nuclei is added, namely soluble organic aerosols (Phillips et al., 2013). The revision of the scheme shows the ongoing research on improving the understanding of ice nuclei nucleation characteristics.

Representing cloud ice sedimentation has a severe influence on the ice water content, reducing it by about 5 mg m^{-3} as shown in the meridional average in Fig. 5.3. Ice crystal sedimentation is important for the humidity transport, as the ice crystals evaporate in lower sub-saturated model levels. For sedimentation and deposition the ice crystal form assumed in this work are hexagonal plates, which are mostly found near cloud top in mid-latitude and tropical cirrus (Heymsfield and McFarquhar, 2002). This choice was made due to needs of consistency but is not trivial, as different temperatures and supersaturation cause a variety of different shapes to form with different habits (see Fig. 2.1). The ice supersaturation is also changed due to the relaxation timescale approach used for describing depositional growth in the new cloud ice scheme. Higher ice supersaturations cause a decrease in thick cirrus and anvil occurrence while increasing stratospheric water vapour (Gettelman and Kinnison, 2007), which is also observed to occur with the new ice microphysics.

In total, a new two-moment cloud ice scheme was developed which accounts for the physical processes dominating cirrus clouds. When intercomparing the model results from the regional COSMO model and the global GME, the cirrus occurrences and locations do not change drastically with the new ice microphysics scheme. The location of the cirrus clouds are thus confined to the availability of atmospheric water vapour and the model dynamics. When looking at single clouds, differences in the horizontal and vertical structures and microphysical properties are observable for the operational and new cloud ice microphysics schemes. Results from the global model showed that the new cloud ice scheme causes a reduction in high cloud occurrence and ice water content. The reduction of high ice water contents in comparison to the GME is a result of the introduction of cloud ice sedimentation. The introduction of the activated ice nuclei tracking additionally reduces the ice water contents in the regions of heterogeneous nucleation. For regions between 8-10km this reduction is compliant with the CALIPSO data. Yet, difficulties arise when comparing the CALIPSO ice water content product to the GME_{ice} . The influence of snow is dominant in the IWC and high attenuation reduces the detection of IWC

in lower altitudes with the CALIPSO lidar. Even though the CALIOP lidar is sensitive to cloud ice in higher altitudes, the CALIOP can not detect ice water contents below 0.4 mg m^{-3} during daytime (Avery et al., 2012). This makes the evaluation very sensitive to the validity interval of the derived satellite IWC and complicates a conclusive statement concerning the exact quality of the IWC magnitude of the GME_{ice} .

6.2.2 Ice Supersaturation

The triggering of homogeneous and heterogeneous ice nucleation depends on the magnitude of atmospheric ice supersaturation. Once cloud ice nucleation is triggered, further atmospheric mechanism influence the subsequent ice cloud evolution. Ice crystal sedimentation is especially important for heterogeneously nucleated ice particles as they reach larger dimensions. Cloud ice sedimentation is also crucial for restructuring the cloud and causes sustained in-cloud ice supersaturation (Spichtinger and Gierens, 2009a). The depletion of ice supersaturation is dependent on the timescale of depositional growth which is a challenge as it varies between 0.5h-3h according to which nucleation mechanism is active (Khvorostyanov and Sassen, 2002).

Numerical weather prediction and climate models require a consistent treatment of cloud microphysics. At present, the application of prognostic statistical cloud schemes is common. These employ sub-grid scale inhomogeneities by using probability distribution functions (PDFs). In Kärcher and Burkhardt (2008) and Wang and Penner (2010) the statistical cirrus cloud scheme PDFs for total water and temperature are described for clear-sky and in-cloud conditions. These cloud parameterisations are based on the operational scheme of the ECMWF by Tiedtke (1993), using clear-sky humidity fluctuations to predict cloud fraction and cloud condensate. However, cloudy air is assumed to be saturated. The operational cloud scheme in the NWP models at the DWD differs from the described statistical scheme. Instead of assuming sub-grid scale variability, the cloud scheme uses prognostic variables for all hydrometeors to achieve a good representation of the bulk microphysical processes. One advantage is that no separations between in-cloud and clear sky conditions are made. Thus it was possible to achieve an improvement of the ice supersaturation with the change in depositional growth, even within cloudy air. The chosen parameterisations for representing cirrus formation in this work are found to be consistent with the total microphysics scheme.

In the previous chapter the relative humidity with respect to ice from the GME and the GME_{ice} were compared to the IFS. The altered ice nucleation scheme in the GME_{ice} captures the distribution of the high ice supersaturation values better than the original scheme. The higher ice supersaturation values may partly be due to the lower ice water contents with the new cloud ice microphysics, which constitute a smaller sink for water vapour depletion through depositional growth. A main difference in the microphysics scheme of the IFS is that the depositional growth process is not explicitly modelled and consequently all humidity is converted to ice and $\text{RH}_i = 100\%$ within a model time step once nucleation is triggered (Tompkins et al., 2007). This leads to in-cloud saturation and can be observed by the peak at $\text{RH}_i = 100\%$ in the rela-

tive frequency plots in Fig. 5.19. In the GME_{ice} however, in-cloud supersaturation is allowed and physically represented due to the relaxation timescale approach for the altered depositional growth. This is a physical approach as e.g., Ovarlez et al. (2002) and Comstock et al. (2004) show in-cloud ice supersaturation to be a common phenomena. Looking at one year of Raman lidar measurements in 2000 at the Southern Great Plains facility near Lamont, Oklahoma, Comstock et al. (2004) finds that $RHi > 100\%$ is found in about 31 % of the cloudy data points. Khvorostyanov and Sassen (2002) also point out that there is a residual ice supersaturation of 5-10% left following a few hours after a cloud has developed. Also, the higher relative humidities are in accordance with the RHi distribution law derived from 3 years of MOZAIC measurements (Gierens et al., 1999).

The ice supersaturated regions and their vertical layer thickness is especially decisive for mitigation purposes reducing anthropogenic cloudiness as these are potential contrail regions. A possible mitigation strategy was previously illustrated in Fig. 1.1. This was part of the project 'Environmentally Compatible Flight Route Optimisation' described in Mannstein (2008) which investigated possible contrail mitigation strategies to reduce anthropogenic induced cloudiness. The better representation of ice supersaturation makes the altered cloud ice microphysics interesting for other investigations concerning contrails and their lifetime in upper tropospheric conditions. Findings concerning the life cycle of supersaturated regions in the upper troposphere from Dietz (2012) show that the humidity in the $COSMO_{ice}$ model is more realistic than in the operational COSMO-EU. Of interest could also be the implementation of an extra source term into the ice microphysics scheme for contrails which converts water vapour into cloud ice, for example, as proposed by Ferrone (2011) in Eq.(5.1).

6.2.3 Scale dependencies of ice microphysics processes

The new cloud ice scheme was tested in different NWP model environments, where the horizontal resolution differed from $\Delta x = 1$ km to $\Delta x = 30$ km. Especially homogeneous freezing of liquid phase aerosols are prone to be effected by the different NWP model resolutions, as high vertical velocities and the correlated high ice supersaturations are necessary for triggering homogeneous freezing. The scale dependency of the vertical velocity and the ice supersaturation is thus investigated. The refined COSMO-DE run of the 26th of August 2011 over 24 hours with a horizontal resolution of 1.7 km is used to investigate small scale fluctuations, e.g. in the vertical velocity w . For coarser model grids like the GME with a lack of these fluctuations in w , a further sub-grid scale variability would be desirable to achieve more realistic atmospheric conditions. Such is stressed in e.g., Hoyle et al. (2005), Gierens et al. (2007) and Dotzek and Gierens (2008) where statistic evaluations of cooling rates in the upper troposphere are conducted.

In the following, the maximum values for the vertical velocity and ice supersaturation in the $COSMO_{ice}$ model are investigated. The additional model variables w_{max} and $S_{i,max}$ are included in the 6 minute interval model output for the upper troposphere. The correlation between the

maximum values for the high-resolution regional model and the maximum values of the global model are investigated. The model variables w and S_i are of special importance as they determine the onset of nucleation events and the resulting ice crystal number density.

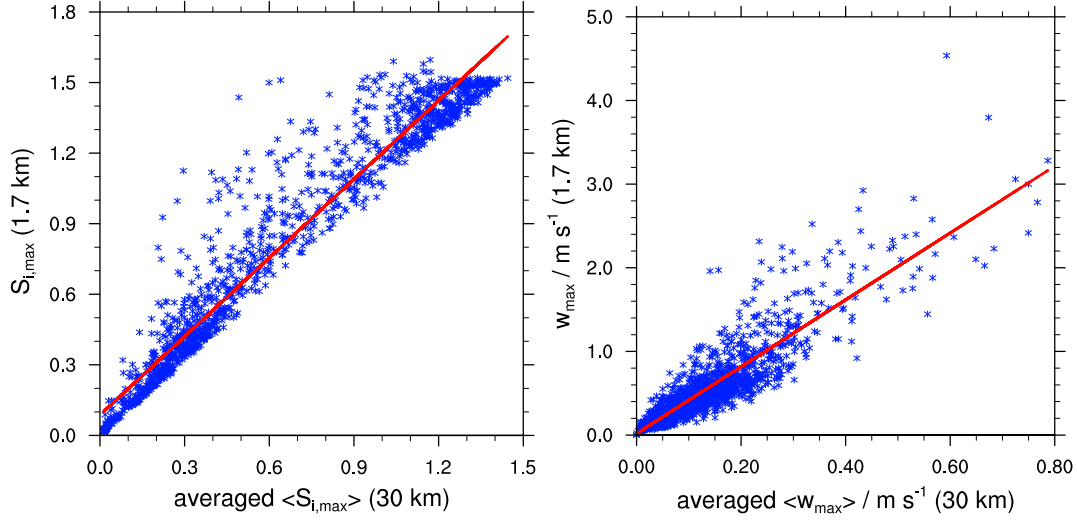


Figure 6.1: Depicted are the maximum values for the high resolution COSMO model run in relation to the maximum values for S_i and w averaged over the global model resolution with a linear regression line.

The scatterplots in Fig. 6.1 show the scale dependency of the vertical velocity and the ice supersaturation ratio. The maximum values of the COSMO-DE are compared to spatially averaged (upscaled) values for the grid spacing of 30km as used in the global model. For instance, $S_{i,max} = 1.41$ is correlated to the averaged value over the global model resolution $\langle S_{i,max} \rangle = 1.2$. This relation is more significant for the vertical velocity where the mean value in the global model $w_{max} = 0.4 \text{ m s}^{-1}$ corresponds to $\langle w_{max} \rangle = 1.6 \text{ m s}^{-1}$. A linear regression for a sub-grid scale ice supersaturation $S_{i,sgs}$ yields

$$S_{i,sgs} = \alpha_S(S_{i,GME} - S_{i,x}) + S_{i,y} \quad (6.1)$$

where the maximum rate is $\alpha_S = 1.11$ and the coefficients are $S_{i,x} = 0.62$ and $S_{i,y} = 0.78$. The resulting sub-grid scale vertical velocity w_{sgs} with the linear regression is

$$w_{sgs} = \alpha_w(w_{GME} - w_x) + w_y \quad (6.2)$$

with the maximum rate $\alpha_r = 4$ and the coefficients $w_x = 0.14$ and $w_y = 0.56$. The relation shows that the upscaled ice supersaturation ratio attains high values close to the high resolution output with a maximum rate of $\alpha_S = 1.11$. However, the vertical velocities show a great deficit in strong updraft when considering the upscaled values and the maximum rate ($\alpha_r = 4$) is a lot higher. This finding once again highlights the necessity of sub-grid scale fluctuations and related cooling rates in global models. The values $S_{i,sgs}$ and w_{sgs} can be used for further calculations in the cloud ice scheme along with the additional source for the vertical velocity that have been derived from the sub-grid scale orography scheme as described in Sec. 4.3. This

relation can then be applied to the Kärcher et al. (2006) scheme to estimate the sub-grid vertical velocity and ice supersaturation. In order to counteract repressing heterogeneous nucleation $S_{i,sgs}$ should only be applied if the model ice saturation ratio $S_{i,GME}$ is greater than 1.3. The sub-grid scale processes should primarily serve to achieve higher ice crystal number densities resulting from homogeneous nucleation, as this is still a shortcoming in cirrus modelling.

Chapter 7

Conclusion and Outlook

Cirrus clouds are one of the most ill-understood cloud types with a strong impact on climate (Barahona and Nenes, 2008). The formation of cirrus cloud is a multiscale problem, as the synoptic scale provides the environment, the mesoscale determines the forcing, and the actual nucleation events occur on a microscopic scale. This makes the parameterisation in numerical weather prediction models and climate models a challenging task. This work is supposed to help improve the understanding of the dominant processes controlling ice nucleation and ice supersaturation and account for them in numerical weather prediction models.

The mechanism controlling homogeneous and heterogeneous nucleation were localised as being the ice nuclei concentration, the fluctuations in the vertical velocity, the depositional growth and the cloud ice sedimentation. A two-moment two-mode ice nucleation scheme was developed and implemented. Using this scheme the mentioned dependencies and atmospheric processes were examined in detail. The resulting new cloud ice scheme is an extension of the ice microphysical parameterisation operational in the numerical weather prediction models at the German Weather Service (Deutscher Wetterdienst, DWD). In particular, the operational ice microphysics scheme lacks the representation of homogeneous nucleation of liquid aerosol droplets and cloud ice sedimentation. Further, the cloud ice crystal number from the operational cloud ice scheme only includes a temperature-based empirical parameterization that describes the increasing number of ice nuclei or ice crystals with decreasing temperature and can not distinguish between different nucleation modes, such as immersion or deposition freezing. Formed cloud ice rapidly depletes existing ice supersaturation. Though ice supersaturation is permitted as the depositional growth is explicitly resolved, a limitation ensures that not more water vapour is depleted than available. This ice microphysical framework makes a more physical approach for ice nucleation and ice supersaturation in the cloud ice scheme of the DWD model chain desirable.

The new cirrus scheme is compatible with both, the non-hydrostatic regional model COSMO and the global model GME and numerical stability as well as physical consistency can be ensured for a wide range of scales. Ice nucleation is described using state-of-the-art parameterisa-

tions for homogeneous and heterogeneous nucleation. While the latter mainly depends on the existence of ice nuclei, homogeneous freezing of supercooled liquid aerosol occurs in regions with high ice supersaturations and high cooling rates, i.e. in strong vertical updrafts. Further extensions of the operational scheme were made such as particle sedimentation and tracking for activated ice nuclei which is necessary to avoid an overestimation of heterogeneously nucleated ice particles. A relaxation timescale method is applied to achieve a consistent treatment of the depositional growth of the two small-particle ice modes and the larger snowflakes. Additional sub-grid scale vertical velocity fluctuations used in the microphysics scheme were derived. A systematic sensitivity study showed that the detailed choices in the design of the scheme do matter for the competition of heterogeneous vs. homogeneous nucleation. As atmospheric conditions for the triggering of homogeneous freezing depend on small-scale fluctuations, the resolved supersaturation over ice depends strongly on the model resolution. To investigate this resolution dependency high-resolution COSMO model simulations were performed with the aim to formulate a consistent parameterisation for the regional COSMO model and the global GME. This is of importance, as sensitivities of microphysical characteristics of cirrus clouds can alter the large-scale dynamics and the radiative properties of the atmosphere. A comparison of the GME containing the new ice microphysics with lidar data showed that on average the differences in cirrus occurrence and location remain similar, whereas the individual cloud structure is altered in comparison to the operational cloud ice scheme. The consistent formation of cirrus clouds in the global model with the operational and new cloud ice scheme shows the dominance of the model dynamics for cirrus formation. Yet, on the microphysical properties from the individual formed cirrus clouds differ for both cloud ice schemes. Cirrus formed with the operational ice microphysics scheme are of a rather opaque character with high ice water contents. However, with the new cloud ice microphysics, the cirrus clouds are not as uniformly structured and the ice water contents were reduced. The lower ice water contents in heights between 9-11 km are in accordance with the ice water content derived from CALIPSO (Cloud-Aerosol Lidar and Infrared Pathfinder Satellite Observations) data for July 2011. Also the ice supersaturation distribution was greatly improved with the new two-moment cloud ice scheme in comparison to IFS (Integrated Forecast System) data. In addition, the prediction of in-cloud supersaturation over ice became possible due to changes in the depositional growth scheme. In-cloud ice supersaturation is not allowed for in the IFS model but various in-situ measurements have provided evidence for its existence. The improved representation of ice supersaturation with the new cloud ice scheme thus allows for advances in predicting condensation trails with NWP models.

Homogeneous nucleation requires high vertical velocities while heterogeneous nucleation depends on the existence as well as the species of the aerosol. Further work concerning sub-grid scale fluctuations in the vertical velocity and an improved model representation of ice nuclei have thus to be conducted. In the new cloud ice scheme, a prognostic tracing variable for activated ice nuclei was introduced. This was a simplified approach to introduce time and space variability for ice nuclei. For future investigations, a coupling to the model aerosol climatology would be desirable. A further step would include the coupling to a full prognostic coupled

aerosol model, such as the COSMO-ART (ART stands for Aerosol and Reactive Trace gases) (Vogel et al., 2009).

Projects such as 'High Definition Clouds and Precipitation for Climate Prediction' (Stevens et al., 2013) deal with future applications and requirements for model parameterisations. In this project, the microphysical effect of implementing the entire high-resolution approach from Morrison et al. (2005) for large-eddy simulations is investigated. This would have the advantage of dealing with the Bergeron-Findeisen process in a more physical way. For this work, the cloud ice and snow relaxation timescales were adapted for the depositional growth. As the COSMO-DE model microphysical scheme also accounts for graupel, for the future it would be of interest to implement the new cloud ice scheme in combination with the graupel and investigate the interactions.

Nomenclature and Abbreviations

Symbol	Description	Units
α_d	Deposition coefficient	1
α_S	Maximal rate for linear regression for S_i	1
α_w	Maximal rate for linear regression for w	1
Δt	Model time step	s
Δx	Horizontal model resolution	m
η	Dynamic viscosity	$\text{m}^2 \text{s}^{-1}$
τ_c	Optical cloud thickness	1
τ_{dep}	Timescale for depositional growth	s
τ_{freez}	Time of freezing event	s
ρ_a	Air density	kg m^{-3}
ρ_i	Ice particle mass density	kg m^{-3}
v_i	Specific volume of a water molecule w.r.t. ice	m^{-3}
v_{th}	Thermal speed	cm s^{-1}
χ_{IN}	Scaling parameter for the amount of available ice nuclei	1
a	Half-width of bell-shaped hills	m
a_w	Water activity of a solution	1
a_{iw}	Water activity in equilibrium with ice	1
c_p	Specific heat capacity of air	$\text{J kg}^{-1} \text{K}^{-1}$
BC	Inorganic black carbon	cm^{-3}
D_c	Average diameter of cloud droplets	μm
D_i	Ice crystal diameter	μm
$D_{i,\text{max}}$	Ice crystal maximum dimension	μm
D_v	Coefficient of water vapour diffusion in air	$\text{m}^2 \text{s}^{-1}$
DM	Dust/metallic aerosols	cm^{-3}
e_v	Vapour pressure over ice	Pa
e_s	Saturation vapour pressure	Pa
e_{si}	Saturation vapour pressure over ice	Pa
e_{sw}	Saturation vapour pressure over water	Pa
g	Acceleration of gravity	ms^{-2}
H_i	Howell factor for diffusional growth	1

h_{\max}	Height of bell-shaped hills	m
h_{surf}	Artificial model orography height for idealised simulations	m
IWC	Ice water content	gm^{-3}
IWP	Ice water path	gm^{-2}
J	Nucleation rate	$\text{cm}^{-3} \text{s}^{-1}$
J_{cr}	Critical nucleation rate	$\text{cm}^{-3} \text{s}^{-1}$
k_b	Boltzmann constant	J K^{-1}
L_m^{ef}	Effective latent heat of melting	cal g^{-1}
L_s	Latent heat of sublimation	J kg^{-1}
m_c	Average mass of cloud droplets	kg
$m_{i,0}$	Mass of individual ice particle prior to freezing	kg
m_i	Mass of individual ice particle	kg
M_a	Molecular mass of air	kg mol^{-1}
M_w	Molecular mass of water	kg mol^{-1}
m_w	Mass of a water molecule	kg
n	Number of bell-shaped hills	1
$n_{i,0}$	Aerosol number density prior to freezing	cm^{-3}
n_i	Number density of ice particles	cm^{-3}
N_i	Ice crystal number	kg kg^{-1}
$n_{\text{frac},X}$	Frozen ice nuclei fraction for aerosol species X	cm^{-3}
$n_{i,\text{het}}$	Heterogeneously nucleated number density of ice particles	cm^{-3}
$N_{i,\text{het}}$	Heterogeneously nucleated number density of ice particles	kg kg^{-1}
$n_{i,\text{hom}}$	Homogeneously nucleated number density of ice particles	cm^{-3}
n_{IN}	Available ice nuclei per time step	cm^{-3}
$n_{i,\text{nuc}}$	Activated ice nuclei number density	cm^{-3}
$n_{\text{IN},\text{PDA08}}$	Ice nuclei number density as defined by PDA08	cm^{-3}
$n_{\text{IN},X}$	Number density for active IN for species	cm^{-3}
n_{sat}	Number density at saturation	cm^{-3}
$n_{X,a}$	Number mixing ratio for activated IN per species	kg^{-1}
O	Insoluble organic carbon	cm^{-3}
S_{nuc}	Heterogenous nucleation of cloud ice	s^{-1}
$S_{c,\text{frz}}$	Nucleation of cloud ice due to homogeneous freezing of cloud water	s^{-1}
$S_{i,\text{au}}$	Autoconversion of cloud ice to form snow due to aggregation	s^{-1}
$S_{i,\text{dep}}$	Deposition growth and sublimation of cloud ice	s^{-1}
$S_{i,\text{dep}}$	Deposition rate for homogeneous and heterogeneous cloud ice	s^{-1}
$S_{i,\text{melt}}$	Melting of cloud ice to form cloud water	s^{-1}
S_{aud}	Autoconversion of cloud ice to form snow due to deposition	s^{-1}
S_{agg}	Collection of cloud ice by snow (aggregation)	s^{-1}
$S_{i,\text{cri}}$	Collection of ice by rain to form snow	s^{-1}
q_i	Cloud ice	kg kg^{-1}
q_v	Water vapour mixing ratio	kg kg^{-1}
$q_{v,s}$	Water vapour mixing ratio at saturation	kg kg^{-1}

$q_{v,si}$	Water vapour mixing ratio at ice saturation	kg kg^{-1}
$q_{v,sw}$	Water vapour mixing ratio at water saturation	kg kg^{-1}
$r_{i,0}$	Aerosol particle radius prior to freezing	μm
r_i	Ice crystal radius	μm
R	Universal gas constant	$\text{J mol}^{-1} \text{K}^{-1}$
RHi	Relative humidity with respect to ice	%
RHw	Relative humidity with respect to water	%
R_a	Gas constant for air	$\text{J mol}^{-1} \text{K}^{-1}$
R_w	Gas constant for water	$\text{J mol}^{-1} \text{K}^{-1}$
S_i	Ice saturation ratio	1
$S_{i,sgs}$	Sub-grid scale ice saturation ratio from linear regression	1
$S_{i,x}$	Coefficient for linear regression	1
$S_{i,y}$	Coefficient for linear regression	1
$S_{i,cr}$	Critical ice saturation ratio for homogeneous freezing	1
$S_{w,cr}$	Critical water saturation ratio heterogeneous freezing	1
T	Air temperature	K
T_c	Air temperature	$^{\circ}\text{C}$
u_0	Initial horizontal wind speed	ms^{-1}
V_0	Initial volume	cm^3
v_i^T	Terminal velocity of ice particles	cm^3
w	Vertical velocity	ms^{-1}
w_{COSMO}	Vertical velocity from the COSMO model	ms^{-1}
w_{TKE}	Vertical velocity derived from the turbulent kinetic energy	ms^{-1}
w_{sgs}	Sub-grid scale vertical velocity from linear regression	ms^{-1}
w_x	Coefficient for linear regression	1
w_y	Coefficient for linear regression	1

Abbreviation	Description
CALIPSO	Cloud-Aerosol Lidar and Infrared Pathfinder Satellite Observations
CAM3	Community Atmosphere Model 3
CCN	Cloud Condensation Nuclei
CNES	Centre National d'Études Spatiales
CEPEX	Central Equatorial Pacific Experiment
CFDC	Continuous Flow Diffusion Chamber
COSMO	Consortium for Small-Scale Modeling
COSMO-ART	COSMO including Aerosol and Reactive Trace gases
COSMO-DE	COSMO local model over Germany
COSMO-EU	COSMO local model over Europe
DLR	Deutsches Zentrum für Luft- und Raumfahrt (German Aerospace Center)

DWD	Deutscher Wetterdienst (German Weather Service)
ECHAM5	European Centre/ Hamburg 5 climate model
ECMWF	European Centre for Medium-Range Weather Forecast
GCMs	Global Circulation Models
GEOS	Goddard Earth Observing System
GMAO	Global Modeling and Assimilation Office
GME	Global Model
HIRS	High Resolution Infrared Radiation Sounder
IFS	Integrated Forecast System
IN	Ice Nuclei
INCA	Interhemispheric differences in cirrus properties from anthropogenic emissions
ISSRs	Ice Supersaturated Regions
Lidar	Light Detection and Ranging
MARL	Mobile Aerosol Raman Lidar
MLS	Microwave Limb Sounder
MODIS	Moderate Resolution Imaging Spectroradiometer
MOZAIC	Measurements of Ozone by Airbus in-service Aircraft
MSG	Meteosat Second Generation
NASA	National Aeronautics and Space Administration
NCAR	National Center for Atmospheric Research
NWCSAF	Nowcasting Satellite Application Facility
NWP	Numerical Weather Prediction
OLR	Outgoing Longwave Radiation
PDFs	Probability Distribution Functions
PSC	Polar Stratospheric Clouds
RMSE	Root Mean Square Error
SEVIRI	Spinning Enhanced Visible and Infrared Imager
SSO	Sub-Scale Orography
SVC	Subvisible Cirrus
TKE	Turbulent Kinetic Energy
TTL	Tropical Tropopause Layer
UTLS	Upper Troposphere/ Lower Stratosphere
WMO	World Meteorological Organization

Bibliography

- Ansmann, A., M. Tesche, D. Althausen, D. Mueller, P. Seifert, V. Freudenthaler, B. Heese, M. Wiegner, G. Pisani, P. Knippertz, and O. Dubovnik, 2008: Influence of Saharan dust on cloud glaciation in southern Morocco during the Saharan Mineral Dust Experiment. *J. Geophys. Res.*, **113**, D04210, doi:10.1029/2007JD008785.
- Avery, M., D. Winker, A. Heymsfield, M. Vaughan, and S. Young, 2012: Cloud ice water content retrieved from the CALIOP space-based lidar. *Geophys. Res. Lett.*, **39**, L05808, doi:10.1029/2011GL050545.
- Baldauf, M., J. Förstner, S. Klink, T. Reinhardt, C. Schraff, A. Seifert, and K. Stephan, 2010: Kurze Beschreibung des Lokal-Modells Kürzestfrist COSMO-DE (LMK) und seiner Datenbanken auf dem Datenserver des DWD. Deutscher Wetterdienst, P.O. Box 100465, 63004 Offenbach, Germany.
- Barahona, D. and A. Nenes, 2008: Parameterization of cirrus cloud formation in large-scale models: Homogeneous nucleation. *J. Geophys. Res.*, **113**, D11211, doi:10.1029/2007JD009355.
- 2009: Parameterizing the competition between homogeneous and heterogeneous freezing in cirrus cloud formation-monomodisperse ice nuclei. *Atmos. Chem and Phys.*, **9**, 369–381, doi:10.5194/acp-9-369-2009.
- Barahona, D., J. Rodriguez, and A. Nenes, 2010: Sensitivity of the global distribution of cirrus ice crystal concentration to heterogeneous freezing. *J. Geophys. Res.*, **115**, doi:10.1029/2010JD014273.
- Baum, B. A., A. J. Heymsfield, P. Yang, and S. T. Bedka, 2005: Bulk Scattering Properties for the Remote Sensing of Ice Clouds. Part I: Microphysical Data and Models. *J. Appl. Met.*, 1885–1895.
- Baumgardner, D., J. E. Dye, B. W. Gandrud, and R. G. Knollenberger, 1992: Interpretation of measurements made by the forward scattering spectrometer probe (FSSP-300) during the airborne Arctic stratospheric expedition. *J. Geophys. Res.: Atmospheres*, **97**, 8035–8046.
- Chen, T., W. B. Rossow, and Y. Zhang, 2000: Radiative effects of cloud-type variations. *Journal of Climate*, **13**, 264–286, doi:10.1175/1520-0442(2000)013<0264:REOCTV>2.0.CO;2.

- CloudSat Data Processing Center, 2012: CloudSat/TRMM Intersects. Accessed: 11/19/2012.
URL <http://www.cloudsat.cira.colostate.edu/dpcstatusTRMM.php>
- Cohard, J.-M. and J.-P. Pinty, 2000: A comprehensive two-moment warm microphysical bulk scheme. I:Description and tests. *Quart. J. Roy. Met. Soc.*, **126**, 1815–1842.
- Comstock, J. M., T. P. Ackermann, and D. D. Turner, 2004: Evidence of high ice supersaturation in cirrus clouds using ARM Raman lidar measurements. *Geophys. Res. Lett.*, **31**, 10.1029/2004GL019705.
- Comstock, J. M., R.-F. Lin, D. O’Starr, and P. Yang, 2008: Understanding ice supersaturation, particle growth, and number concentration in cirrus cloud. *J. Geophys. Res.*, **113**, 10.1029/2008JD010332.
- Cox, S. K., 1971: Cirrus clouds and the climate. *J. Atmos. Sci.*, **28**, 1513–1515, doi:10.1175/1520-0469(1971)028<1513:CCATC>2.0.CO;2.
- Curry, J. A. and V. I. Khvorostyanov, 2012: Assessment of some parameterizations of heterogeneous ice nucleation in cloud an climate models. *Atmos. Chem and Phys.*, **12**, 1151–1172, doi:10.5194/acp-12-1151-2012.
- Delanoë, J., R. J. Hogan, R. M. Forbes, A. Bodas-Salcedo, and T. H. M. Stein, 2011: Evaluation of ice cloud representation in the ECMWF and UK Met Office models using CloudSat and CALIPSO data. *Quart. J. Roy. Met. Soc.*, **137**, 2064–2078, doi:10.1002/qj.882.
- DeMott, P. J., M. P. Meyers, and W. R. Cotton, 1994: Parameterization and impact of ice initiation processes relevant to numerical model simulations of cirrus clouds. *J. Atmos. Sci.*, **51**, 77–90.
- DeMott, P. J., O. Möhler, O. Stetzer, G. V. Z. Levin, M. D. Petters, M. Murakami, et al., 2011: Resurgence in ice nuclei measurement research. *Bull. Am. Met. Soc.*, **102**, 1623–1635, doi:10.1175/2011BAMS3119.1.
- DeMott, P. J., D. C. Rogers, and S. M. Kreidenweis, 1997: The susceptibility of ice formation in upper tropospheric clouds to insoluble aerosol components. *J. Geophys. Res.*, **102**, 19575–19584, doi:10.1029/97JD01138.
- Derrien, M. and H. L. Gléau, 2005: MSG/SEVERI cloud mask and type from SAFNWC. *International Journal of Remote Sensing*, **26**, 4707–4732, doi:10.1080/01431160500166128.
- Deuber, O., S. Matthes, R. Sausen, M. Ponater, and L. Lim, 2013: A physical metric-based framework for evaluating the climate trade-off between CO₂ and contrails- The case of lowering aircraft flight trajectories. *Environmental Science and Policy*, **25**, 176–185, doi:10.1016/j.envsci.2012.10.004.
- Dietz, S., 2012: *Untersuchung Charakteristischer Lebenszyklen von Eisübersättigten Regionen in der oberen Troposphäre*. Masterarbeit, Institut für Meteorologie und Geophysik der Universität Innsbruck.

-
- Doms, G., J. Forstner, E. Heise, H.-J. Herzog, M. Raschendorfer, T. Reinhardt, B. Ritter, R. Schrodin, J.-P. Schulz, and G. Vogel, 2007: A description of the nonhydrostatic regional model Im, Part II: Physical Parameterization. Deutscher Wetterdienst, P.O. Box 100465, 63004 Offenbach, Germany.
- Doms, G., D. Majewski, A. Müller, and B. Ritter, 2004: Recent changes to the cloud-ice scheme. COSMO Newsletter No.4.
- Dotzek, N. and K. Gierens, 2008: Instantaneous fluctuations of temperature and moisture in the upper troposphere and tropopause region. Part 2: Structure functions and intermittency. *Meteorol. Zeitschr.*, **17**, 323–337.
- Dowling, D. R. and L. F. Radke, 1990: A summary of the physical properties of cirrus clouds. *J. Appl. Met.*, **29**, 970–987.
- Eastwood, M. L., S. Cremel, C. Gehrke, E. Girard, and A. K. Bertram, 2008: Ice nucleation on mineral dust particles: Onset conditions, nucleation rates and contact angles. *J. Geophys. Res.*, **114**, 10.1029/2008JD010639.
- ECMWF, 2011: IFS Documentation, Part IV: Physical Processes. <http://www.ecmwf.int/research/ifsdocs/CY37r1/index.html>.
- Eidhammer, T., P. J. DeMott, and S. M. Kreidenweis, 2009: A comparison of heterogeneous ice nucleation parameterizations using a parcel model framework. *J. Geophys. Res.*, **114**, D06202, doi:10.1029/2008JD011095.
- Eleftheratos, K., C. S. Zerefos, P. Zanis, D. S. Balis, G. Tselioudis, K. Gierens, and R. Sausen, 2007: A study on natural and manmade global interannual fluctuations of cirrus cloud cover for the period 1984-2004. *Atmos. Chem and Phys.*, **7**, 2631–2642.
- Emersic, C., 2012: Cloud Physics Research- Light Scattering by Ice Crystals. <http://www.cas.manchester.ac.uk/resactivities/cloudphysics/topics/lightscattering>, accessed: 15/03/2012.
- EUMETSAT, 2011: SEVIRI- cloud top height factsheet. *EUM/OPS/DOC/11/4199*, 1–5.
- Ferrone, A., 2011: *Aviation and climate change in Europe: from regional climate modelling to policy-options*. Ph.D. thesis, Earth and Life Institute (ELI), Georges Lemaître Centre for Earth and Climate Research (TECLIM), Université catholique de Louvain (UCL) (Belgium).
- Field, P., A. J. Heymsfield, and A. Bansemmer, 2006: Shattering and particle interarrival times measured by optical array probes in ice clouds. *J. Atmos. Ocean. Tech.*, **23**, 1257–1371.
- Field, P. R., R. J. Cotton, K. Noone, P. H. Kaye, E. Hirst, R. S. Greenaway, C. Jost, R. Gabriel, R. Reiner, M. Andreae, C. P. R. Saunders, A. Archer, T. Choulaton, M. Smith, B. Brooks, C. Hoell, B. Bandy, D. Johnson, and A. Heymsfield, 2001: Ice nucleation in orographic wave clouds: Measurements made during INTACC. *Quart. J. Roy. Met. Soc.*, **127**, 1493–1512.

- Fletcher, N. H., 1962: *Physics of Rain Clouds*. Cambridge University Press.
- Fornea, A. P., S. D. Brooks, J. B. Dooley, and A. Saha, 2009: Heterogeneous freezing of ice on atmospheric aerosols containing ash, soot, and soil. *J. Geophys. Res.*, **114**, doi:10.1029/2009JD011958.
- Forster, P., V. Ramaswamy, P. Artaxo, T. Berntsen, R. Betts, D. W. Fahey, J. Haywood, J. Lean, D. C. Lowe, G. Myhre, J. Nganga, R. Prinn, G. Raga, M. Schulz, and R. V. Dorland, 2007: Climate Change 2007: The Physical Science Basis. *Intergovernmental Panel on Climate Change Fourth Assessment Report: Climate Change 2007*, S. Solomon, D. Qin, M. Manning, Z. Chen, M. Marquis, K. Averyt, M. Tignor, and H. Miller, eds., Cambridge University Press, Cambridge, UK and New York, NY, USA.
- Fu, Q. and K. N. Liou, 1993: Parameterization of the radiative properties of cirrus clouds. *J. Atmos. Sci.*, **50**, 2008–2025.
- Fukuta, N. and L. A. Walter, 1970: Kinetics of hydrometeor growth from a vapor-spherical model. *J. Atmos. Sci.*, **27**, 1160–1172.
- Fusina, F., P. Spichtinger, and U. Lohmann, 2007: Impact of the ice supersaturated regions and thin cirrus on radiation in the midlatitudes. *J. Geophys. Res.*, **112**, doi:10.1029/2007JD008449.
- Gayet, J.-F., F. Auriol, A. Minikin, J. Ström, M. Seifert, R. Krejci, A. Petzold, G. Febvre, and U. Schumann, 2002: Quantitative measurement of the microphysical and optical properties of cirrus clouds with four different in situ probes: Evidence of small ice crystals. *JGR*, **29**, doi:10.1029/2001GL014342.
- Gayet, J.-F., J. Ovarlez, V. Sherbakov, J. Ström, U. Schumann, A. Minikin, F. Auriol, A. Petzold, and M. Monier, 2004: Cirrus cloud microphysical and optical properties at southern and northern midlatitudes during the INCA experiment. *JGR*, **109**, D20206, doi:10.1029/2004JD004803.
- Gettelman, A. and D. E. Kinnison, 2007: The global impact of supersaturation in a coupled chemistry-climate model. *Atmos. Chem and Phys.*, **7**, 1629–1643.
- Gettelman, A., X. Liu, D. Barahona, U. Lohmann, and C. Chen, 2012: Climate impacts of ice nucleation. *J. Geophys. Res.*, **117**, 10.1029/2012JD017950.
- Gettelman, A., X. Liu, S. J. Ghan, H. Morrison, S. Park, A. J. Conley, S. A. Klein, J. Boyle, D. L. Mitchell, and J. F. Li, 2010: Global simulations of ice nucleation and ice supersaturation with an improved cloud scheme in the community atmosphere model. *J. Geophys. Res.*, **115**, 10.1029/2009JD013797.
- Gierens, K., R. Kohlhepp, N. Dotzek, and H. G. Smit, 2007: Instantaneous fluctuations of temperature and moisture in the upper troposphere and tropopause region, Part I: Probability density and their variability. *Meteorol. Zeitschr.*, **16**, 221–231.

-
- Gierens, K., U. Schumann, M. Helten, H. Smit, and A. Marengo, 1999: A distribution law for relative humidity in the upper troposphere and lower stratosphere derived from three years of MOZAIC measurements. *Ann. Geophysicae*, **17**, 1218–1226.
- Gierens, K. and P. Spichtinger, 2000: On the distribution of ice-supersaturated regions in the upper troposphere and lowermost stratosphere. *Ann. Geophysicae*, **18**, 499–504, doi:10.1007/s00585-000-0499-7.
- Gierens, K., P. Spichtinger, and U. Schumann, 2012: Ice supersaturation. *Atmospheric Physics, Background-Methods-Trends*, U. Schumann, ed., Springer-Verlag.
- Gierens, K. M., 2003: On the transition between heterogeneous and homogeneous freezing. *Atmos. Chem and Phys.*, **3**, 437–446.
- Gierens, K. M., M. Monier, and J.-F. Gayet, 2003: The deposition coefficient and its role for cirrus clouds. *J. Geophys. Res.*, **108**, doi:10.1029/2001JD001558.
- Gu, Y. and K. N. Liou, 2000: Interaction of radiation, microphysics, and turbulence in the evolution of cirrus clouds. *J. Atmos. Sci.*, **91**, 2463–2479.
- Gultepe, I. and D. O. Starr, 1995: Dynamical structure and turbulence in cirrus clouds: Aircraft observations during fire. *J. Atmos. Sci.*, **52**, 4159–461.
- Haag, W. and B. Kärcher, 2004: The impact of aerosols and gravity waves on cirrus clouds at midlatitudes. *J. Geophys. Res.*, **109**, 10.1029/2004JD004579.
- Haag, W., B. Kärcher, S. Schäfer, O. Stetzer, O. Möhler, U. Schurath, M. Krämer, and C. Schiller, 2003: Numerical simulations of homogeneous freezing processes in the aerosol chamber AIDA. *Atmos. Chem and Phys.*, **3**, 195–210.
- Hallett, J., W. P. Arnott, M. P. Bailey, and J. T. Hallett, 2002: Ice crystals in cirrus. *Cirrus*, D. K. Lynch, K. Sassen, D. O. Starr, and G. Stephens, eds., Oxford University Press.
- Harrington, J. Y., D. Lamb, and R. Carver, 2009: Parameterization of surface kinetic effects for bulk microphysical models: Influences on simulated cirrus dynamics and structure. *J. Geophys. Res.*, **114**, 10.1029/2008JD011050.
- Hartmann, D. L., M. E. Ockert-Bell, and M. L. Michelsen, 1992: The effect of cloud type on earth's energy balance: Global analysis. *J. Atmos. Clim.*, **5**, 1281–1304.
- Hastings, D. A., P. K. Dunbar, G. M. Elphinstone, M. Bootz, H. Murakami, H. Maruyama, H. Masaharu, P. H. J. Payne, N. A. Bryant, T. L. Logan, J.-P. Muller, G. Schreier, and J. S. MacDonald, 1999: The global land one-kilometer base elevation (globe) digital elevation model, version 1.0.
URL <http://www.ngdc.noaa.gov/mgg/topo/globe.html>
- Hegg, D. A. and M. B. Baker, 2009: Nucleation in the atmosphere. *Reports on Progress in Physics*, **72**, 10.1088/0034-4885/72/5/056801.

- Heymsfield, A., D. Microphysics, P. DeMott, P. Forster, K. Gierens, and B. Kärcher, 2010: Contrail microphysics. *Bull. Am. Met. Soc.*, **91**, 465–472, doi:10.1175/2009BAMS2839.1.
- Heymsfield, A. J., 2007: On measurements of small ice particles in clouds. *Geophys. Res. Lett.*, **34**, 10.1029/2007GL030951.
- Heymsfield, A. J. and J. Iaquinta, 2000: Cirrus crystal terminal velocities. *J. Atmos. Sci.*, **57**, 916–938.
- Heymsfield, A. J. and G. M. McFarquhar, 1996: High albedos of cirrus in the tropical pacific warm pool: Microphysical interpretations from CEPEX and from Kwajalein, Marshall Islands. *J. Atmos. Sci.*, **53**, 2424–2451.
- 2002: Mid-latitude and tropical cirrus. *Cirrus*, D. K. Lynch, K. Sassen, D. O. Starr, and G. Stephens, eds., Oxford University Press.
- Heymsfield, A. J. and C. M. R. Platt, 1984: A parameterization of the particle size spectrum of ice clouds in terms of the ambient temperature and the ice water content. *J. Atmos. Sci.*, **41**, 846–855.
- Heymsfield, A. J. and R. M. Sabin, 1989: Cirrus crystal nucleation by homogeneous freezing of solution droplets. *J. Atmos. Sci.*, **46**, 2252–2264.
- Heymsfield, A. J. and C. D. Westbrook, 2010: Advances in the estimation of ice particle fall speeds using laboratory and field measurements. *J. Atmos. Sci.*, **67**, 2469–2482.
- Heymsfield, A. J., D. Winker, and G.-J. van Zadelhoff, 2005: Extinction-ice water content-effective radius algorithms for CALIPSO. *Geophys. Res. Lett.*, **32**, L10807, doi:10.1029/2007GL030951.
- Hobbs, P. V. and A. L. Rangno, 1985: Ice particle concentrations in clouds. *J. Atmos. Sci.*, **42**, 2523–2548.
- Hoose, C., J. E. Kristjánsson, J.-P. Chen, and A. Hazra, 2010: A classical-theory-based parameterization of heterogeneous ice nucleation by mineral dust, soot, and biological particles in a global climate model. *J. Atmos. Sci.*, **67**, 2483–2503.
- Howell, W. E., 1948: The growth of cloud drops in uniformly cooled air. *J. Meteor.*, **6**, 134–149.
- Hoyle, C., B. Luo, and T. Peter, 2005: The origin of high ice crystal number densities in cirrus clouds. *J. Atmos. Sci.*, **62**, 2568–2579, doi:10.1175/JAS3487.1.
- Immler, F., R. Treffeisen, D. Engelbart, K. Krüger, and O. Schrems, 2008: Cirrus, contrails and ice supersaturated regions in high pressure systems at northern mid latitudes. *Atmos. Chem and Phys.*, **8**, 1689–1699, doi:10.5194/acp-8-1689-2008.
- Jacobsen, M. Z., 2005: *Fundamentals of Atmospheric Modeling*. Cambridge University Press, New York.

-
- Jakob, C., 2002: Ice clouds in numerical weather prediction models- Progress, problems and prospects. *Cirrus*, D. K. Lynch, K. Sassen, D. O. Starr, and G. Stephens, eds., Oxford University Press.
- Jensen, E. J., L. Pfister, and O. B. Toon, 2011: Impact of radiative heating, wind shear, temperature variability, and microphysical processes on the structure and evolution of thin cirrus in the tropical tropopause layer. *J. Geophys. Res.*, **116**, 10.1029/2010JD015417.
- Jensen, E. J. and O. B. Toon, 1994: Ice nucleation in the upper troposphere: Sensitivity to aerosol number density, temperature, and cooling rate. *Geophys. Res. Lett.*, **21**, 2019–2022.
- Joos, H., P. Spichtinger, and U. Lohmann, 2009: Orographic cirrus in a future climate. *Atmos. Chem and Phys.*, **9**, 7825–7845.
- Joos, H., P. Spichtinger, U. Lohmann, J.-F. Gayet, and A. Minkin, 2008: Orographic cirrus in the global climate model ECHAM5. *J. Geophys. Res.*, **113**, doi:10.1029/2007JD009605.
- Kärcher, B. and U. Burkhardt, 2008: A cirrus cloud scheme for general circulation models. *Quart. J. Roy. Met. Soc.*, **134**, 1439–1461, doi:10.1175/JAS3447.1.
- Kärcher, B., J. Hendricks, and U. Lohmann, 2006: Physically based parameterization of cirrus cloud formation for use in global atmospheric models. *J. Geophys. Res.*, **111**, D01205, doi:10.1029/2005JD006219.
- Kärcher, B. and U. Lohmann, 2002: A parameterization of cirrus cloud formation: Homogeneous freezing of supercooled aerosols. *J. Geophys. Res.*, **107**, 4010, doi:10.1029/2001JD000470.
- 2003: A parameterization of cirrus cloud formation: Heterogeneous freezing. *J. Geophys. Res.*, **108**, 4402, doi:10.1029/2002JD003220.
- Kärcher, B. and S. Solomon, 1999: On the composition and optical extinction of particles in the tropopause region. *J. Geophys. Res.*, **104**, 27,441–27,459.
- Kärcher, B. and J. Strom, 2003: The roles of dynamical variability and aerosols in cirrus cloud formation. *Atmos. Chem and Phys.*, **3**, 823–838.
- Khvorostyanov, V., 1995: Mesoscale processes of cloud formation, cloud-radiation interaction, and their modelling with explicit cloud microphysics. **39**, 1–67.
- Khvorostyanov, V. and K. Sassen, 1998a: Cirrus cloud simulation using explicit microphysics and radiation. Part I: Model description. *J. Atmos. Sci.*, **55**, 1808–1821, doi:10.1175/1520-0469(1998)055<1808:CCSUEM>2.0.CO;2.
- 1998b: Cirrus cloud simulation using explicit microphysics and radiation. Part II: Microphysics, vapor and ice mass budgets, and optical and radiative properties. *J. Atmos. Sci.*, **55**, 1822–1844.

- Khvorostyanov, V. I. and J. A. Curry, 2004: The theory of ice nucleation by heterogeneous freezing of deliquescent mixed CCN. Part I: Critical radius, energy, and nucleation rate. *J. Atmos. Sci.*, **61**, 2676–2691.
- 2005: Fall velocities of hydrometeors in the atmosphere: Refinements to a continuous analytical power law. *J. Atmos. Sci.*, **62**, 4343–4357.
- 2009: Critical humidities of homogeneous and heterogeneous ice nucleation: Inferences from extended classical nucleation theory. *J. Geophys. Res.*, **114**, 10.1029/2008JD011197.
- Khvorostyanov, V. I. and K. Sassen, 2002: Microphysical processes in cirrus and their impact on radiation. *Cirrus*, D. K. Lynch, K. Sassen, D. O. Starr, and G. Stephens, eds., Oxford University Press.
- Koop, T., B. Luo, A. Tsias, and T. Peter, 2000: Water activity as the determinant for homogeneous ice nucleation in aqueous solutions. *Nature*, **206**, 611–614.
- Korolev, A., M. P. Bailey, J. Hallett, and G. A. Isaac, 2003: Laboratory and in situ observation of deposition growth of frozen drops. *J. Appl. Met.*, **43**, 612–622.
- Korolev, A. and I. Mazin, 2003: Supersaturation of water vapor in clouds. *J. Atmos. Sci.*, **60**, 2957–2974.
- Krämer, M., C. Schiller, A. Afchine, R. Bauer, I. Gensch, A. Mangold, S. Schlicht, N. Spelten, N. Sitnikov, S. Borrmann, M. de Reus, and P. Spichtinger, 2009: Ice supersaturations and cirrus cloud crystal numbers. *Atmos. Chem and Phys.*, **9**, 3505–3522.
- Ladino, L. A. and J. P. D. Abatt, 2013: Laboratory investigations of Martian water ice cloud formation using dust aerosol simulants. *J. Geophys. Res.: Planets*, **118**, 14–25, doi:10.1029/2012JE004238.
- Lamquin, N., C. J. Stubenrauch, K. Gierens, U. Burkhardt, and H. Smit, 2012: A global climatology of upper-tropospheric ice supersaturation occurrence inferred from the Atmospheric Infrared Sounder calibrated by MOZAIC. *Atmos. Chem and Phys.*, **12**, 381–405, doi:10.5194/acp-12-381-2012.
- Lee, D. S., G. Pitari, V. Grewe, K. Gierens, J. E. Penner, A. Petzold, M. J. Prather, U. Schumann, A. Bais, T. Berntsen, D. Iachetti, L. L. Lim, and R. Sausen, 2010: Transport impacts on atmosphere and climate: Aviation. *Atmos. Env.*, **44**, 4678–4734, doi:10.1016/j.atmosenv.2009.06.005.
- Leisner, T., 2008: Laborexperimente zur Wolkenmikrophysik. DMG presentation.
- Lin, R.-F., D. O. Starr, P. J. DeMott, R. Cotton, K. Sassen, E. Jensen, B. Kärcher, and X. Liu, 2002: Cirrus parcel model comparison project. Phase 1: The critical components to simulate cirrus initiation explicitly. *J. Atmos. Sci.*, **59**, 2305–2329.

-
- Liou, K.-N., 1986: Influence of cirrus clouds on weather and climate processes: A global perspective. *Mon. Wea. Rev.*, **114**, 1167–1199, doi:10.1175/1520-0493(1986)114<1167:IOCCOW>2.0.CO;2.
- Liou, K. N., 1992: *Radiation and Cloud Processes in the Atmosphere*. Oxford University Press, New York.
- Liou, K. N., J. L. Lee, S. C. Ou, Q. Fu, and Y. Takano, 1991: Ice cloud microphysics, radiative transfer and large-scale cloud processes. *Meteorol. Atmos. Phys.*, **46**, 41–50.
- Liu, X. and J. E. Penner, 2005: Ice nucleation parameterization for global models. *Meteorol. Zeitschr.*, **14**, 499–514.
- Lohmann, U. and K. Diehl, 2006: Sensitivity studies of the importance of dust ice nuclei for the indirect aerosol effect of stratiform mixed-phase clouds. *J. Atmos. Sci.*, **63**, 968–982.
- Lohmann, U., J. Feichter, C. C. Chuang, and J. Penner, 1999: Prediction of the number of cloud droplets in the ECHAM GCM. *J. Geophys. Res.*, **104**, 9169–9198.
- Lott, F. and M. J. Miller, 1997: A new subgrid-scale orographic drag parameterization: Its formulation and testing. *Quart. J. Roy. Met. Soc.*, **123**, 101–127.
- Lynch, D. K., 2002: Cirrus: History and definitions. *Cirrus*, D. K. Lynch, K. Sassen, D. O. Starr, and G. Stephens, eds., Oxford University Press.
- Lynch, D. K. and K. Sassen, 2002: Subvisual cirrus. *Cirrus*, D. K. Lynch, K. Sassen, D. O. Starr, and G. Stephens, eds., Oxford University Press.
- Ma, H.-Y., M. Köhler, J.-L. F. Li, J. D. Farrara, C. Mechoso, R. M. Forbes, and D. E. Waliser, 2012: Evaluation of an ice cloud parameterization based on a dynamical-microphysical lifetime concept using CloudSat observations and the ERA-Interim reanalysis. *J. Geophys. Res.*, **117**, D05210, doi:10.1029/2011JD016275.
- Majewski, D., D. Liermann, P. Prohl, B. Ritter, M. Buchhold, T. Hanisch, G. Paul, W. Wergen, and J. Baumgardner, 2002: The operational global icosahedral-hexagonal gridpoint model GME: Description and high-resolution tests. *J. Atmos. Sci.*, **139**, 319–338.
- Mannstein, H., 2008: Climate Protection and Adaption-Results of the klimazwei Research Programme- Umweltgerechte Flugroutenoptimierung.
URL <http://www.klimazwei.de/Portals/0/klimazwei-Ergebnisbroschüre.pdf>
- Marengo, A., V. Thouret, P. Nédélec, H. Smit, M. Helten, D. Kley, F. Karcher, et al., 1998: Measurement of ozone and water vapor by Airbus in-service aircraft: The MOZAIC airborne program, an overview. *J. Geophys. Res.*, **103**, 25631–25642, doi:10.1029/98JD00977.
- Maxwell, J. C., 1890: *The Scientific Papers of James Clerk Maxwell*. Cambridge University Press, New York.

- Mellor, G. L. and T. Yamada, 1974: A hierarchy of turbulence closure models for planetary boundary layers. *J. Atmos. Sci.*, **31**, 1791–1806, doi:http://dx.doi.org/10.1175/1520-0469(1974)031<1791:AHOTCM>2.0.CO;2.
- Meyers, M. P., P. J. DeMott, and W. R. Cotton, 1992: New primary ice-nucleation parameterizations in an explicit cloud model. *J. Appl. Met.*, **31**, 708–721.
- Minikin, A., A. Petzold, J. Ström, R. Krejci, M. Seifert, P. van Velthoven, H. Schlager, and U. Schuman, 2003: Aircraft observations of the upper tropospheric fine particle aerosol in the Northern and Southern Hemisphere at midlatitudes. *Geophys. Res. Lett.*, **30**, 10.1029/2002GL016458.
- Mitchell, D. L., 1996: Use of mass- and area-dimensional power laws for determining precipitation particle terminal velocities. *J. Atmos. Sci.*, **53**, 1710–1723.
- Mitchell, D. L. and A. J. Heymsfield, 2005: Refinements in the treatment of ice particle terminal velocities, highlighting aggregates. *J. Atmos. Sci.*, **62**, doi:10.
- Moorthi, S. and M. J. Suarez, 1992: Relaxed Arakawa-Schubert. A parameterization of moist convection for general circulation models. *Mon. Wea. Rev.*, **120**, 978–1002, doi:10.1175/1520-0493(1992)120<0978:RASAPO>2.0.CO;2.
- Morrison, H., J. Curry, and V. Khvorostyanov, 2005: A new double-moment microphysics parameterization for application in cloud and climate models. Part I: Description. *J. Atmos. Sci.*, **62**, 1665–1677, doi:10.1175/JAS3447.1.
- Murphy, D. M. and T. Koop, 2005: Review of ice and supercooled water for atmospheric applications. *Quart. J. Roy. Met. Soc.*, **131**, 1539–1565.
- Ovarlez, J., J.-F. Gayet, K. Gierens, J. Ström, H. Ovarlez, F. Auriol, R. Busen, and U. Schumann, 2002: Water vapor measurements inside cirrus clouds in northern and southern hemispheres during inca. *Geophys. Res. Lett.*, **29**, doi:10.1029/2001GL014440.
- Phillips, V., C. Andronache, B. Christner, C. Morris, D. Sands, A. Bansemer, A. Lauer, C. McNaughton, and C. Seman, 2009: Potential impacts from biological aerosols on ensembles of continental clouds simulated numerically. **6**, 987–1014.
- Phillips, V., P. DeMott, and C. Andronache, 2008: An empirical parameterization of heterogeneous ice nucleation for multiple chemical species of aerosol. *J. Atmos. Sci.*, **65**, 2757–2783.
- Phillips, V. T., P. J. DeMott, C. Andronache, K. A. Pratt, et al., 2013: Improvements to an empirical parameterization of heterogeneous ice nucleation and its comparison with observations. *J. Atmos. Sci.*, **70**, 378–409, doi:10.1175/JAS-D-12-080.1.
- Powell, K., M. Vaughan, D. Winker, K.-P. Lee, M. Pitts, C. Trepte, et al., 2010: Cloud-aerosol LIDAR infrared pathfinder satellite observations: Data management system: Data products catalog: Release 3.2. Technical Report PC-SCI-503, NASA Langley Research Center.

-
- Pruppacher, H. R. and J. D. Klett, 1997: *Microphysics of Clouds and Precipitation*. Kluwer Academic Publishers, Dordrecht.
- Read, W. G., A. Lambert, J. Bacmeister, R. E. Cofield, L. E. Christensen, D. T. Cuddy, W. H. Daffer, B. J. Drouin, and other, 2007: Aura microwave limb sounder upper tropospheric and lower stratospheric H_2O and relative humidity with respect to ice validation. *J. Geophys. Res.*, **112**, doi:10.1029/2007JD008752.
- Reitter, S., K. Fröhlich, and A. Seifert, 2011: Evaluation of ice and snow content in the global numerical weather prediction model GME with CloudSat. *Geosc. Model Dev.*, **4**, 579–589, doi:10.5194/gmd-4-579-2011.
- Reitter, S., A. Seifert, C. Köhler, and S. Crewell, 2013: Evaluation of ice clouds in COSMO-DE with satellite observations. EUMETSAT/AMS Meteorological Conference Abstract.
- Ren, C. and A. R. MacKenzie, 2005: Cirrus parameterization and the role of ice nuclei. *Quart. J. Roy. Met. Soc.*, **131**, 1585–1605, doi:10.1256/qj.04.126.
- Rienecker, M. M., M. J. Suarez, R. Todling, J. Bacmeister, L. Takacs, H.-C. Liu, W. Gu, M. Sienkiewicz, R. D. Koster, R. Gelaro, et al., 2008: Technical report series on global modeling and data assimilation: The GEOS-5 data assimilation system- documentation of versions 5.0.1, 5.1.0, and 5.2.0. Technical Report NASA/TM-2008-104606, NASA Goddard Space Flight Center.
- Sassen, K. and J. R. Campbell, 2001: A midlatitude cirrus cloud climatology from the facility for atmospheric remote sensing. Part I: Macrophysical and synoptic properties. *J. Atmos. Sci.*, **58**, 481–496.
- Sassen, K. and B. S. Cho, 1992: Subvisual-thin cirrus lidar dataset for satellite verification and climatological research. *J. Appl. Met.*, **31**, 1275–1285.
- Sassen, K., Z. Wang, and D. Liu, 2008: Global distribution of cirrus clouds from CloudSat/Cloud-Aerosol Lidar and Infrared Pathfinder Satellite Observations (CALIPSO) measurements. *J. Geophys. Res.*, **113**, D00A12, doi:10.1029/2008JD009972.
- Schiller, C., M. Kraemer, A. Afchine, N. Spelten, and N. Sitnikov, 2008: Ice water content of the Arctic, midlatitude, and tropical cirrus. *J. Geophys. Res.*, **113**, doi:10.1029/2008JD010342.
- Schulz, J.-P. and U. Schättler, 2010: Kurze Beschreibung des Lokal-Modells Europa COSMO-EU (LME) und seiner Datenbanken auf dem Datenserver des DWD. Deutscher Wetterdienst, P.O. Box 100465, 63004 Offenbach, Germany.
- Schumann, U., 2002: Contrail cirrus. *Cirrus*, D. K. Lynch, K. Sassen, D. O. Starr, and G. Stephens, eds., Oxford University Press.
- Spichtinger, P., 2004: *Eisübersättigte Regionen*. Ph.D. thesis, Deutsches Zentrum für Luft- und Raumfahrt, Institut für Physik der Atmosphäre, Oberpfaffenhofen.

- Spichtinger, P. and D. Cziczo, 2010: Impact of heterogeneous ice nuclei on homogeneous freezing events in cirrus clouds. *J. Geophys. Res.*, **115**, doi:10.1029/2009JD0112168.
- Spichtinger, P. and K. Gierens, 2004: On the distribution of relative humidity in cirrus clouds. *Atmos. Chem and Phys.*, **4**, 639–647.
- 2009a: Modelling of cirrus clouds - Part 1a: Model description and validation. *Atmos. Chem and Phys.*, **9**, 685–706.
- 2009b: Modelling of cirrus clouds - Part 2: Competition of different nucleation mechanisms. *Atmos. Chem and Phys.*, **9**, 2319–2334.
- Spichtinger, P., K. Gierens, U. Leiterer, and H. Dier, 2003a: Ice supersaturation in the tropopause region over Lindenberg, Germany. *Meteorol. Zeitschr.*, **12**, 143–156.
- Spichtinger, P., K. Gierens, and W. Read, 2003b: The global distribution of ice-supersaturated regions as seen by the Microwave Limb Sounder. *Quart. J. Roy. Met. Soc.*, **129**, 3391–3410.
- Stapelberg, S., P. D. J. Fischer, T. Böhme, T. Akkermans, T. Rheinhardt, et al., 2010: Long term evaluation of the diurnal cycle of COSMO-DE/EU with Meteosat Second Generation (MSG). QUEST presentation.
- Stephens, G. L., 2002: Cirrus, climate, and global change. *Cirrus*, D. K. Lynch, K. Sassen, D. O. Starr, and G. Stephens, eds., Oxford University Press.
- Stephens, G. L., S.-C. Tsay, J. Paul W. Stackhouse, and P. J. Flatau, 1990: The relevance of the microphysical and radiative properties of cirrus clouds to climate and climatic feedback. *J. Atmos. Sci.*, **47**.
- Stephens, G. L., D. G. Vane, R. J. Boain, G. G. Mace, et al., 2002: The CloudSat mission and the a-train: A new dimension of space-based observations of clouds and precipitation. *Bull. Am. Met. Soc.*, **83**, 1771.
- Stevens, B., 2011: Twelve lectures on cloud physics, winter semester 2010-2011. Max-Planck-Institut für Meteorologie.
- Stevens, B., J. Biercamp, U. Burkhardt, S. Crewell, S. Jones, A. Macke, A. Seifert, C. Simmer, and J. Quaas, 2013: High Definition Clouds and Precipitation for Climate Prediction. <https://is.enes.org/documents/Biercamp.pdf>.
- Tabazadeh, A., E. J. Jensen, and O. B. Toon, 1997: A model description of cirrus cloud nucleation from homogeneous freezing of sulfate aerosols. *J. Geophys. Res.*, **102**, 23,845–23,850.
- The NCAR Command Language (Version 6.0.0), 2012: Software. Boulder, Colorado: UCAR/NCAR/CISL/VETS, <http://dx.doi.org/10.5065/D6WD3XH5>.
- Tiedtke, M., 1993: Representation of clouds in large-scale models. *Mon. Wea. Rev.*, **121**, 3040–3061, doi:10.1175/1520-0493(1993)121<3040:ROCILS>2.0.CO;2.

-
- Tompkins, A., K. Gierens, and G. Rädcl, 2006: Ice supersaturation in the ECMWF Integrated Forecast System. ECMWF Newsletter No. 109.
- 2007: Ice supersaturation in the ECMWF Integrated Forecast System. *Quart. J. Roy. Met. Soc.*, **133**, 53–63.
- Vali, G., 1985: Nucleation terminology. *J. Aerosol Sci.*, **16**, 575–576.
- Vogel, B., H. Vogel, D. Bäumer, M. Bangert, K. Lundgren, R. Rinke, and T. Stanelle, 2009: The comprehensive model system COSMO-ART- Radiative impact fo aerosol on the state of the atmosphere on the regional scale. *Atmos. Chem and Phys.*, **9**, 8661–8680.
- Waliser, D. E., J.-L. F. Li, C. P. Woods, R. T. Austin, J. Bacmeister, J. Chern, A. D. Genio, J. H. Jiang, Z. Kuang, H. Meng, P. Minnis, S. Platnick, W. B. Rossow, G. L. Stephens, S. Sun-Mack, W.-K. Tao, A. M. Tompkins, D. G. Vane, C. Walker, and D. Wu, 2009: Cloud ice: A climate model challenge with signs and expectations of progress. *J. Geophys. Res.*, **114**.
- Wang, M. and J. Penner, 2010: Cirrus clouds in a global climate model with a statistical cirrus cloud scheme. *Atmos. Chem and Phys.*, **10**, 5449–5474, doi:10.5194/acp-10-5449-2010.
- Wang, T. and A. E. Dessler, 2012: Analysis of cirrus in the tropical tropopause layer from CALIPSO and MLS data: A water perspective. *J. Geophys. Res.*, **117**, D04211, doi:10.1029/2011JD016442.
- Whitby, K. T. and B. K. Cantrell, 1976: Electrical measurements of aerosols. *Fine Particle Aerosol Generation, Measurement, Sampling and Analysis*, B. Y. H. Liu, ed., New York, Academic Press, 581–624.
- Winker, D. M., J. R. Pelonn, and M. P. McCormick, 2003: The CALIPSO mission: Spaceborne lidar for observations of aerosols and clouds. *Lidar Remote Sensing for Industry and Environment Monitoring III*, **Proc. SPIE 4893**, doi:10.1117/12.466539.
- Winker, D. M., M. A. Vaughan, A. Omar, et al., 2009: Overview of the CALIPSO Mission and CALIOP Data Processing Algorithms. *J. Atmos. Ocean. Tech.*, **26**, 2310–2323, doi:10.1175/2009JTECHA1281.1.
- WMO, 1975: International Cloud Atlas, Volume I, Manual on the Observation of Clouds and other Meteors. WMO.
- Wylie, D. P. and W. P. Menzel, 1999: Eight years of high cloud statistics using HIRS. *J. Clim.*, **12**, 170–184.
- Yano, J.-I. and V. Phillips, 2011: Ice-Ice collisions: An ice multiplication process in atmospheric clouds. *J. Atmos. Sci.*, **68**, 322–333.
- Zhang, Y., A. Macke, and F. Albers, 1999: Effect of crystal size spectrum and crystal shape on stratiform cirrus radiative forcing. *Atmos. Res.*, **52**, 59–75, doi:10.1016/S0169-8095(99)00026-5.

Acknowledgements

This research contributes to the Klimazwei project 'Umweltgerechte Flugroutenoptimierung (UFO)' ('Environmentally Compatible Flight Route Optimisation') funded by BMBF Grant klimazwei-01LS05114. The CALIPSO data were obtained from the NASA Langley Research Center Atmospheric Science Data Center. The plots were done with The NCAR Command Language (Version 6.0.0) (2012).

I would like to deeply thank Dr. Axel Seifert for his continuous support and supervision. I would also like to thank Dr. Vaughan Phillips, Prof. Dr. Bernd Kärcher and Dr. Klaus Gierens for their help with the ice nucleation schemes. Moreover, I would like to thank Prof. Dr. Schumann for his interest in this work and his helpful suggestions and constructive criticism. Also, I thank Prof. Dr. Craig, who contributed helpful comments on the revision of this thesis. Furthermore, I thank Dr. Peter Spichtinger, Dr. Ulrike Burkhardt and Dr. Simon Unterstrasser for the fruitful discussions. I am very grateful to Dr. Hermann Mannstein who sadly passed away.

Special thanks goes to the FE13 and FE14 researchers at the DWD. Especially Thomas Hanisch and Jochen Förster were a great help with the numerical experiments, IT support and the good music and movies. I would also like to acknowledge the support from the special meteorologists Dr. Kirstin Kober, Isabel Alberts, Karolin Eichler, Nadine Schneider, Dr. Florian Hanisch and Dieter Schuster.

Last but not least, I am deeply grateful for the continuous support and positive attitude of my family and close friends.

Curriculum Vitæ

Personal Dates:

Name: Carmen Köhler

Date and Place of Birth: May 11th, 1980, Berlin

Education & Professional Career:

- 09/1985-06/1999 John F. Kennedy School, Berlin German-American Elementary and High School
· 1998 American High School Diploma
· 1999 German High School Diploma, Abitur
- 08/1999-06/2002 Hairdressing Apprenticeship at Art of Hair by Zaffer, Berlin and earned finishing certificate
- 10/2002-08/2008 Studies of Mathematics at Freie Universität Berlin
· Secondary subject: Meteorology
· Thesis: *Influence of Unsteady Aerodynamic Effects on Aeroplanes in Accordance with the Vortice Lattice Method*. Written at the IABG (Industrieanlagen-Betriebsgesellschaft mbH), Ottobrunn
- 02/2005-04/2005 Internship at the German Aerospace Center (DLR), Department for Flight System Engineering in Braunschweig
· Institute report: *Simplified 3-d Wind Model for the EFCS Simulator* (IB 111-2005/22)
- 09/2005-02/2006 Erasmus Semester at the Universidad de Granada, Spain
- 08/2008-08/2012 PhD within the UFO (Umweltgerechte Flugrouenoptimierung) Project and research scientist at the Institute for Atmospheric Physics at DLR, Oberpfaffenhofen, and German Weather Service (DWD), Offenbach
- since 12/2012 Research scientist in the EWeLiNE (Erstellung innovativer Wetter- und Leistungsprognosemodelle für die Netzintegration wetterabhängiger Energieträger) Project at the DWD, Offenbach